POLITECNICO
MILANO 1863

SCUOLA DI INGEGNERIA INDUSTRIALE
E DELL'INFORMAZIONE

Carbon-fiber/PEKK composite: mode I static and fatigue analysis

Tesi di Laurea Magistrale in
Space Engineering - Ingegneria spaziale

Author: **Pietro Gazzi**

Student ID: 969033
Advisor: Prof. Antonio Mattia Grande
Co-advisors: Dott. Enrico Chemello
Academic Year: 2021-22

Abstract

The purpose of this study is the experimental and numerical characterization of Solvay's PC(PEKK-FC)/S2. Some tests have been performed on uni-directional laminates of the cited material. After the experimental phase, it has been implemented through cohesive elements numerical study to be able to describe the test response.
In composite constructions, delamination is a prevalent failure mechanism. It can be caused by a variety of factors such as impact damage, manufacturing faults, fatigue loading, or out-of-plane force, such as when the structure buckles. It is critical to characterize the delamination development behavior in order to assure safe design. Simulations are an important element of this characterization because they reduce the need for time-consuming and expensive experimental studies.
The simulated test is the double cantilever beam. In order to carry out the simulations a subroutine has been implemented that takes into account the fiber-bridging phenomena observed during the experimental campaign. The subroutines, based on literature models, are both for the quasi-static analysis and fatigue.
A parameter-fitting algorithm has been implemented to achieve the best fidelity results. The Nelson Mead algorithm has been used to ensure this result, creating a recursive FEM-solver call algorithm.
The results of the listed simulations return good results with respect to the experimental one.

Keywords: delamination, thermoplastic composites, fatigue, cohesive elements

Abstract in lingua italiana

Lo scopo di questo studio è la caratterizzazione sperimentale e numerica del PC(PEKK-FC)/S2 di Solvay. Alcuni test sono stati eseguiti su laminati unidirezionali del materiale citato. Dopo la fase sperimentale, è stato implementato attraverso lo studio numerico di elementi coesivi per poter descrivere la risposta al test.

Nelle costruzioni composite, la delaminazione è un meccanismo di guasto prevalente. Può essere causato da una varietà di fattori come danni da impatto, difetti di fabbricazione, carico di fatica o forza fuori dal piano, ad esempio quando la struttura si piega. È fondamentale caratterizzare il comportamento di sviluppo della delaminazione al fine di garantire una progettazione sicura. Le simulazioni sono un elemento importante di questa caratterizzazione perché riducono la necessità di studi sperimentali costosi e dispendiosi in termini di tempo.
La prova simulata è la doppia trave a sbalzo. Per effettuare le simulazioni è stata implementata una subroutine che tiene conto dei fenomeni di fiber-bridging osservati durante la campagna sperimentale. Le subroutine, basate su modelli di letteratura, sono sia per l'analisi quasi-statica che per la fatica.
È stato implementato un algoritmo di adattamento dei parametri per ottenere i migliori risultati di fedeltà. L'algoritmo Nelson Mead è stato utilizzato per garantire questo risultato, creando un algoritmo di chiamata ricorsivo del risolutore FEM.
I risultati delle simulazioni elencate restituiscono buoni risultati rispetto a quella sperimentale.

Parole chiave: delaminazione, compositi termoplastici, fatica, elementi coesivi

Contents

List of Figures

List of Tables

List of Symbols

Variable	Description	SI unit
G	Fracture toughness	J/mm^2
$\boldsymbol{P}$	Load	N
$\boldsymbol{\delta}$	Separation	mm
$\boldsymbol{\sigma}$	Stress	MPa
$\boldsymbol{t}$	Traction	MPa
D	Cohesive degradation	-
D_s	Static degradation	-
D_f	Fatigue degradation	N
E	Young's modulus	MPa
ν	Poisson's ration	-
$\boldsymbol{K}$	Stiffness	MPa

1 | Introduction

The major guideline in aerospace structure material selection is focused on the right compromise between weight and strength. Weight saving is a fundamental aspect due to many reasons, in particular the correlated cost and fuel saving. For example, even with the reduction in launch costs due to new technologies, such as the Space X Falcon 9, the average price for reaching low earth orbit (LEO) is about 5000-10000 $. Through the reduction of the structure mass, there is the possibility to transport much more payload and to have a better income from the mission itself. Moreover, lower masses allow better fuel consumption that is strictly connected with mission costs and life duration. Besides the lightness, another crucial aspect is the ability of a particular material to withstand high loads. High-strength materials are fundamental for primary and secondary structures, due to the high loads witnessed during many phases of a mission. While in the early days of aerospace history aluminum was dominant all over the structures, in the last decades there has been a high increase in composite material. The definition of composite materials is blurred due to the wide variety of them in academia and in the industry field. For the interest of this work, it is considered composite a material composed by two or more constituents. These kinds of materials make possible a more precise design that takes in consideration the loads applied. In order to obtain a particular strength, fatigue response, or thermal properties the constituents can be changed or organized differently. An initial classification of composites is reported in Figure 1.1 accordig to the geometry of the constituents. In these cases, considering two constituents are present, the high-strength brittle material and the matrix that is a ductile carrier of the other component. Here there are reported: particle-reinforced where the high-strength material is composed of spherical or ellipsoidal particles suspended in the matrix; fiber-reinforced in which the suspended material is composed of fibers that can be long or short, depending on the case; finally structural elements, where different layers of different material or composite materials itself are laid-up together.

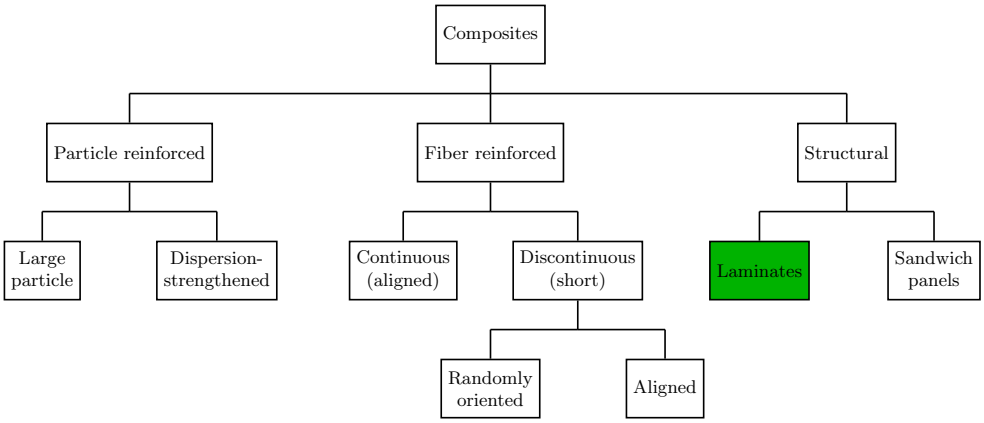

Figure 1.1: Classical composites classification

Combining materials of different characteristics it is possible to achieve new materials with intermediate properties. In this thesis, the main focus is posed on laminates composed by continuous fiber-reinforced ply, in particular thermoplastic carbon fiber reinforced polymers.

1.1. Thermo-plastic composites

Most of the commercial composites used in aerospace, but also automotive, and other fields are based on a thermo-sets matrix. Thermo-set are [1] [2] polymers obtained through a curing process starting from a low viscous and good penetration liquid. The curing procedure is an irreversible hardening process that can be achieved thanks to the heat, and that can be accelerated by high pressure and catalysts. Thermo-set composites are obtained by the composition of reinforcing fibers with this polymer, in particular for this kind of application, epoxy resin is used as a pre-polymer. Due to the nature of the curing process, thermos-set composites present issues, correlated to manufacturing, repairing, and waste management. From a manufacturing point of view, difficult methodologies are required in order to obtain the hardening effect: epoxies need to be preserved at low temperatures before production, and the curing is obtained through an expensive autoclave cycle. A cracked matrix cannot be repaired directly acting on the polymer, but it needs external input, such as patches in the aeronautical sector. Furthermore, sustainability has a

relevant role in any current decision and thermo-set reinforced parts cannot be recycled and they are difficult to be treated. All this generating a huge amount of waste that cannot be post-processed. For all these reasons the industry is moving towards different technologies characterized by similar performances without being affected by the problem cited above. Even if some alternatives are now possible, the aerospace industry has an inertia that is difficult to be stopped and inver. The Technology Readiness Level (TRL) of a process or material is strictly connected to the heritage of previous cases. Many years and experiments are required for new technology to be presented to the general public. Thermoplastic composites are based on thermoplastic matrix and in most cases reinforced with glass or carbon fibers. Because they use a thermoplastic matrix, these materials are not chemically unstable. A thermoplastic resin, often known as a thermosoft plastic, is any plastic polymer substance that becomes flexible or moldable at a high temperature and hardens when cooled [3]. The most used high-performance thermoplastic resin used in structural applications are polyetheretherketone (PEEK), Polyetherketoneketone (PEKK), that will be the main character of this thesis, and Polyphenylene sulfide (PPS). The processing temperature, handling, and storage requirements of the two materials varies substantially. Temperatures ranging from ambient temperature to 150°C are used to produce thermosets. In most cases, they are "set" and treated in an autoclave. The curing period might last up to 12 hours. However, thermosets must be cooled before curing to avoid resin advancement and retain mechanical characteristics. They typically have a shelf life of around 12 months from prepreg manufacturing through part completion. Furthermore, they cannot be remelted, remoulded, or recycled after they have been cured. The production of thermoplastic prepregs and finished thermoplastic components is often more challenging. They require increased processing temperatures of 320°C or more. However, autoclave curing is not usually required. The fundamental benefit of thermoplastics above thermosets is that they have an infinite storage life at ambient temperature prior to curing and do not necessitate refrigeration. Additionally, thermoplastics may be recycled. They may be remelted and rebuilt after curing, providing flexibility and sustainability benefits.

1.2. Thermo-plastic structural applications

These composites materials have not used yet in primary structure, but thanks to the previously mentioned characteristics the use will grow in the next few years in particular in the European market as presented in Figure 1.2.

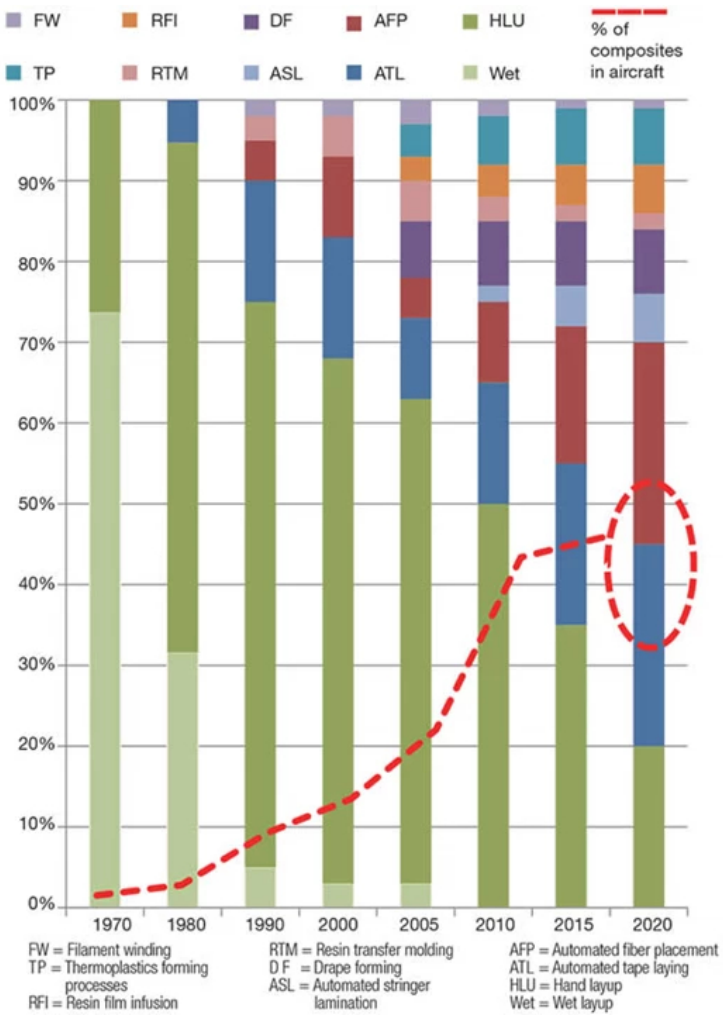

Figure 1.2: Market overview.

In this moment the main applications are in secondary structures such as the Airbus's leading edge of the A300-series.

1.3. Study case

In this thesis, it will be presented a study concerning the numerical and experimental characterization of APC(PEKK-FC)/S2 laminates produced with a hot-press process. This material is commercially available since 2017 but it has not been characterized completely [4]. In particular, it has been developed a numerical optimization process to determine the fracture toughness of uni-directional laminates in a static environment, and a study regarding the fatigue process.

2 | Composites delamination

Delamination is one of the leading failure root causes of fiber-reinforced composites. Delamination consists in the separation between two or more plies during a particular load case. This can happen during all the life of a particular component, starting from the manufacturing process, due to residual stresses or manufacturing errors, until the service itself, in which the part is subjected to various types of load of various nature. Even if fiber-reinforced composites have great performances in the prescribed design stress direction, thanks to the possibility of arranging the ply direction, they perform poorly in out of design conditions,because of low mechanical properties of the matrix. Delamination takes place because the interlaminar strength is low and it can bear only low-intensity phenomena.

2.1. Literature review

FRC's multilayer, non-homogeneous, and orthotropic body can undergo a variety of fracture modes, including matrix cracking. This form of crack is the first typically fracture mechanism to arise and can aid in the occurrence of subsequent modes of fracture. Fibre matrix debonding occurs when the connection between the matrix and the fibre is disrupted, resulting in a drop in material strength. Fibre breaking is the most common fracture mechanism in FRCs: fibres are the elements that carry the weight and the rupture usually results in a significant loss in load bearing capability, if not an outright failure. Delamination occurs with the contact between two laminae breaks, caused for example by an excessive stress concentration near the interface or manufacturing flaws.

2.1.1. Origin of delamination

The technical reasons of delamination, according to Pagano and Schoeppner [5], can be divided into two groups. Delamination owing to curved parts, such as curved sections, tubular segments, cylinders and spheres, and pressurised containers, is included in the first category. Normal and shear loads at the interface between two adjacent plies can cause loss of adhesion and the development of an interlaminar fracture in any of these

circumstances.
The second group comprises sudden changes in section, such as ply drop-offs, couplings between flexural reinforcement and thin plates, open edges, and joined and bolted joints. Temperature and moisture impacts might be included as a third category. The variation in thermal coeffis AQ cients of reinforcement and the matrix causes differential contractions between plies during the laminate curing process. These unequal contractions' residual stresses might be a cause of delamination [6]. Similarly, the variable expansion of the laminate plies during moisture absorption might be a source of delamination [7]. Delamination can also occur during the production stages as result of matrix shrinkage during curing or the creation of resin-rich patches as a result of improper plying methods. Delamination can occur during service in a variety of situations, such as transverse concentrated stresses induced by low velocity collisions. Delamination in composites constructions is frequently caused by impact. Structural damage in the boundary between neighboring plies as a result of collision, the dropping of a tool while manufacture, mounting, or fixing, or ballistic hits in military aircraft or buildings can all cause interlaminar fractures.

2.1.2. Types of delamination

Both internal and near-surface delaminations might be taken into consideration, according to Bolotin [8][9]. Internal delamination can result from the interaction of matrix fractures and ply interfaces in the inner ply interfaces of the laminate. This form of delamination frequently manifests as transverse matrix cracks in plies that are orthogonal to the tensile force. Composite constructions have much lower load capacities as a result of internal delamination. The overall flexural behavior of the laminate is severely impacted, especially when compression stresses are applied, as schematically depicted in Figure 2.1. Even though delamination divides the laminate into two pieces, the deformation of one half of the laminate interacts with the other. As a result of this interaction, both sections of the laminate may deflect similarly.

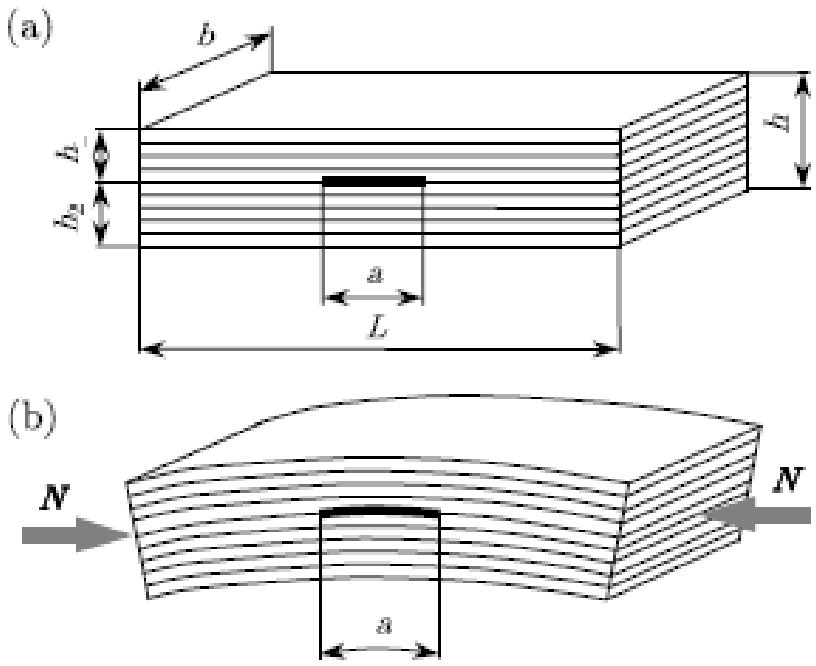

Figure 2.1: Internal delamination. Fig. by Bolotin

Near-surface delaminations, as the name implies, occur near the laminate's surface and constitute a more complicated scenario than internal delaminations. The delaminated part's deformation is less influenced by the deformation of the remainder of the laminate. As a result, the near-surface delaminated section does not always follow the remainder of the laminate's deformation. As a result, not only must the progression of the near-surface delamination be considered, but also its local stability. As illustrated in Figure 2.2, Bolotin[8][9] categorized the various forms of near-surface delamination that might occur in plate composite components under different stress circumstances. Internal or near-surface delaminations can spread under static or fatigue pressures after commencement. In both circumstances, the composite part's strength and stability to flexural loading are significantly reduced. Furthermore, because it is difficult to identify during the inspection, the delamination damage mechanism is very critical for the structural stability of composite constructions.

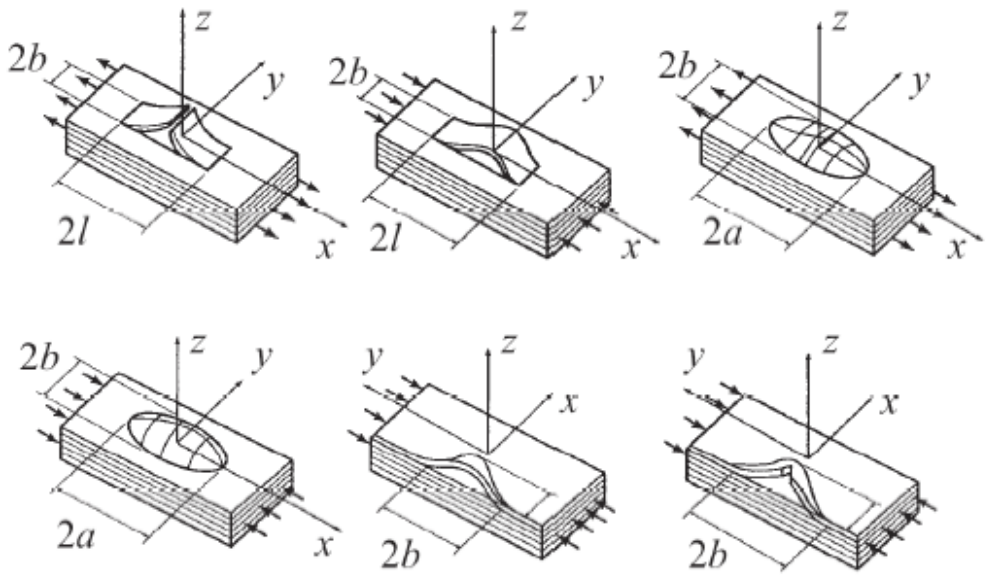

Figure 2.2: Near-surface delamination. Fig. by Bolotin

The near-surface categories specified by Bolotin can be further divided by the nature of the fail, which can be provoked by tension, in both compression and extension, and due to buckling, which can be present at the edge of the laminate or within it.
The establishment of a damage zone ahead of the crack tip precedes the formation of an interlaminar crack at the microscopic level. The size and shape of the deformation/damage zone are seen to be very varied, depending on both resin toughness and stress condition. The classical classification of the fracture modes is still present in delamination, as reported by Irwin [10]. Delamination fracture can occur in three modes: opening or peel mode (mode I), forward sliding shear mode (mode II), and ripping mode (mode III). The damage zone ahead of the fracture tip is higher for mode II or mode III loading than for mode I loading. This difference is due to a substantially slower decrease of the stress held forward of the tip of the crack for shear modes of loading Figure 2.3.

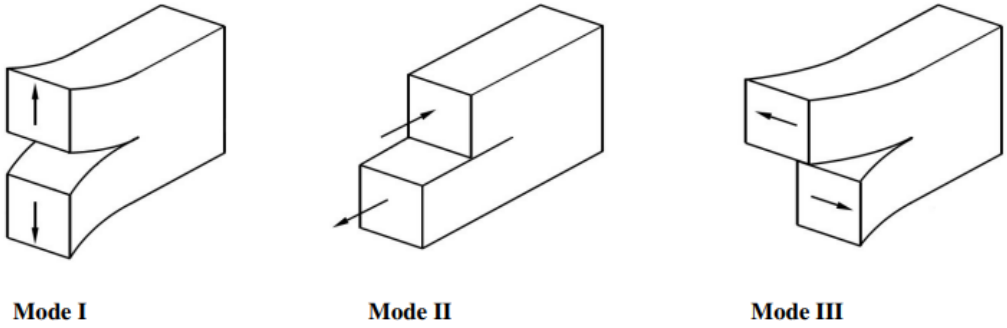

Figure 2.3: Delamination modes

For mode I loading in brittle systems, the zone ahead of the crack tip contains microcracks whose coalescence and growth results in crack advance. Sometimes,crack advance occurs by fibre-matrix debonding before microcrack coalescence occurs. When debonding takes place, fibre bridging and fiber breakage are observed. For ductile systems, plastic deformation around the crack tip precedes crack advance. Crack advance generally occurs by ductile tearing, but crack advance by interfacial debonding was also commonly observed in composites made with more ductile resins [8]. Shear modes, modes II and III, of quasi-brittle systems occur in a unique manner. Microcracks form a significant distance ahead of the crack tip, at a 45o angle to the ply plane. These fissures spread until they reach the fibres that hold the resin-rich area between plies together. It appears that the breaks in the resin occasionally stop short of the next visible fiber. However, there are fibers slightly above or below the surface that seem to be responsible for stopping the growth of these micro-cracks. Micro-crack coalescence is essential for macro-crack advancement. This agglomerate typically happens at the interface between fiber and matrix, producing the appearance of a corrugated roof as well as the production of "hackles" in the resin between fibers. Griffith [11] presented the energy release rate to characterise fracture based on the theory of energy conservation. The reduction in the total potential energy per unit area of crack expansion is described as the energy release rate.

$$G = -\frac{1}{b}\frac{\mathrm{d}U}{\mathrm{d}a} \tag{2.1}$$

2.2. Experimental campaign

Each material needs a specific study and a test campaign in order to obtain a clearer understanding on the behaviour of it in some prefixed circumstances. Testes are needed to characterize the property of the material, even if the test set-up is not representative of a real situation. As previously mentioned, delamination appears in three different modes, however the pure modes are only an idealization. A pure mode I delamination does not appear in any real application case, instead every fracture is always a mixed one. In some situation one mode could be predominant but a mixing part would be in any case present. Although the previous sentence is correct, the mixed mode is difficult to be studied, and it requires necessarely a preliminary study on the pure delamination modes. Once the pure modes are characterized it is possible to study how the two effects combine in a mixed mode case. in this section it is presented the experimental campaign conducted in the Aerospace Polimi's laboratory for the mode i an mode II charaterization of the PEKK unidirectional laminate.

2.3. Double cantilever beam

The double cantilever beam is the most used experimental method to evaluate the mode I fracture toughness. In this particular case, it is used to study the interlaminar fracture toughness of a unidirectional laminate. The experimental setup exploited is coherent with the ASTM standard [12].

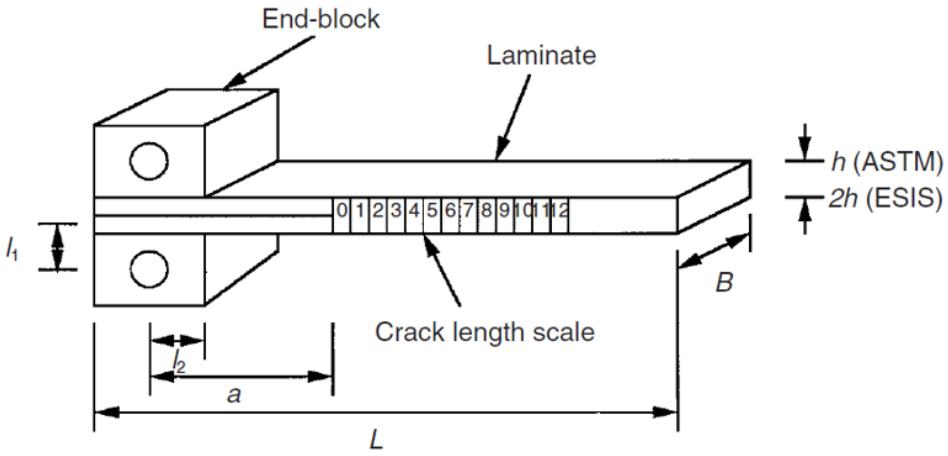

Figure 2.4: DCB test configuration

The unidirectional laminate has been produced with an insert in the middle of the plies.

This insert is used to have a pre-crack in the middle of the laminate. The pre-crack is the starting point of the delamination, from the end of the pre-crack the front crack will develop and continue on the interlaminar matrix. The laminate is then composed by an undamaged part, in which the plies are all bonded together and a part in which there is a separation between plies in the middle of the laminate. Two flaps, with half of the ply of the entire laminate each, compose the damage part. These two sub-parts are free to bend.
The dimension of the specimen is reported in Table 2.1.

Parameters	**Unit**	**Value**
Arm height	mm	1.91
Length	mm	140
Width	mm	21.89
Pre-crack	mm	48
N^o of ply	[–]	32

Table 2.1: DCB specimen geometry.

In the test configuration the two beams are glued with two hinges that are attached to the tensile testing machine. the hinges are then gradually separated, depending on the testing machine the separation can happen in different ways, in the considered test the bottom hinge remain fixed while the other moves upwards. The tensile testing is capable of control how the hinge moves upward, so the increment of deflection rate, and it records the load needed to obtain such separation at each moment. The beginning of the test is reported in Figure 2.5.

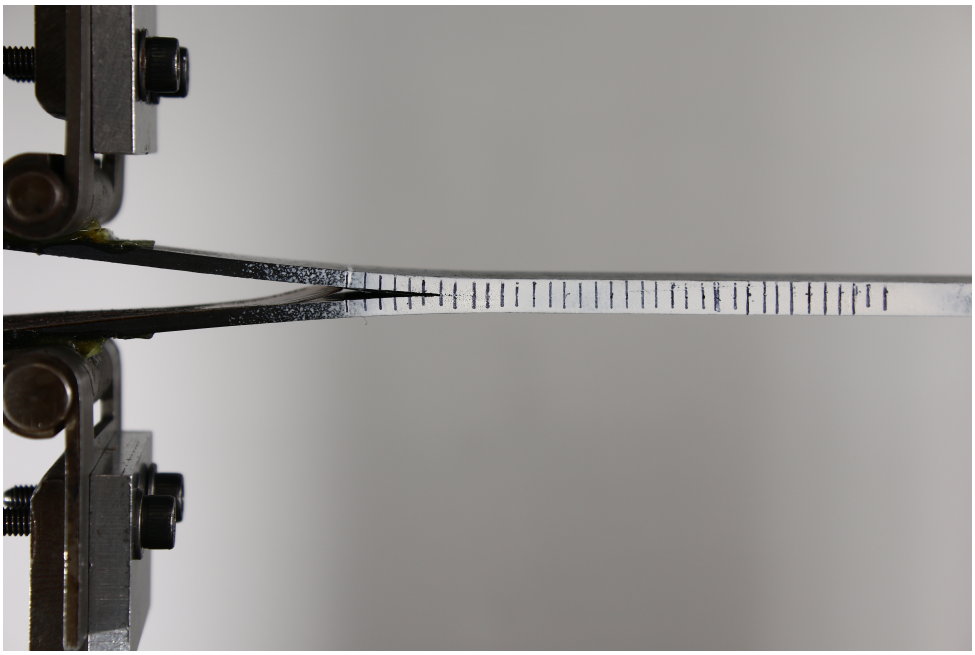

Figure 2.5: DCB test beginning.

The test procedure requires a low increment of the separation between the two hinges. This precaution helps to avoid the contamination induced by the high speed degradation. The presence of a fast dynamics alters the response of the matrix. The photo above has been taken with a camera placed right in front of the test specimen. The camera has been set to take a picture every 5 seconds. The images give information regarding both the status of the phenomena observed, but also, thanks to the scale written on the specimen's side, to detect the position of the front crack respect to the pre-crack.
The data retrieved by the test are the load, displacement and crack length at each time step. From these information it is possible to compute the real objective of the experiment, the fracture toughness This property cannot be detected directly by classical methods, but requires a further computation combining the retrieved parameters.
Various methods, for the computation of the fracture toughness, exist. Depending on the hypothesis considered the results slightly change between procedures. In fact there are models that overestimate the fracture toughness, due to a low prediction on the elastic response of the laminate.

The first data reduction method is the *modified beam theory* [13]. The expression of the energy release rate for this method is reported in Equation 2.4.

$$G_{MBT} = \frac{3P\delta}{2ba} \tag{2.2}$$

Where P is the load applied, δ is the displacement at the load point, a is the crack opening, and b is the specimen width. This is one of the most conservative methods that overestimate fracture toughness. This small excess in the prediction is due to the abstraction used by the method, in fact, this result is obtained considering the two parts of the laminate as 2 beams, so the energy release rate is the energy required to separate the two beams. The result of this computation on 4 different specimens is reviewed in Figure 2.6.

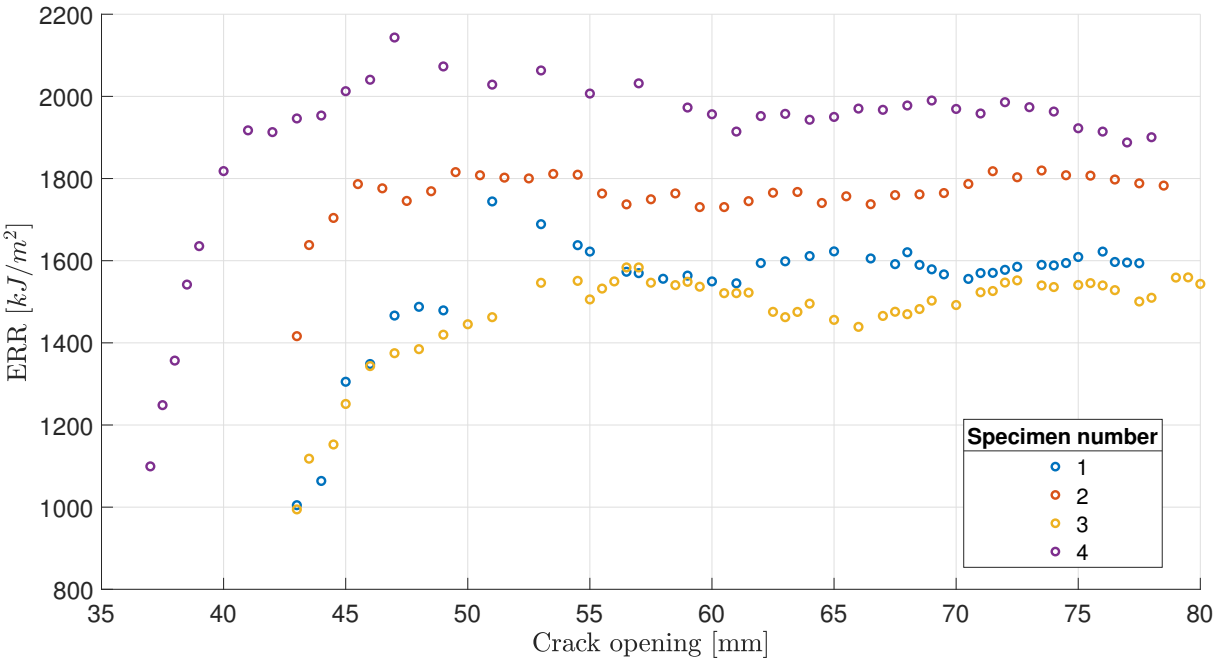

Figure 2.6: Mixed beam theory energy release rate

The second method used is compliance calibration, based on Berry [14]. It makes a least squares plot of $log(\delta_i/P_i)$ vs $log(a_i)$ based on the visually detected delamination starting values and all propagation data. Draw a line through the data to achieve the greatest least-squares fit. Then calculate n as the slope of the line in the $log(C) - log(a)$ graph with the compliance C defined as $C = \delta_i/P_i$.

$$G_{CC} = \frac{nP\delta}{2ba} \tag{2.3}$$

The results of the model for the considered specimen is reported in Figure 2.7.

The previously presented method can be corrected as proposed by Kageyama [15], as reported in Equation 2.4.

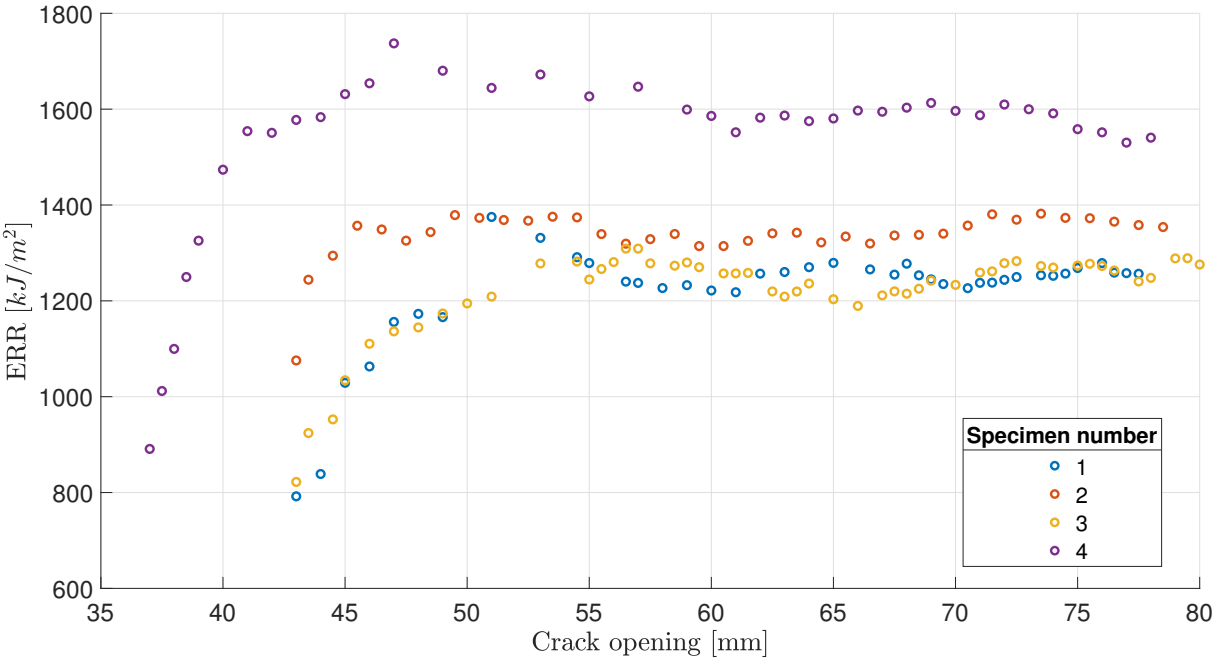

Figure 2.7: Compliance calibration theory energy release rate

$$G_{MCC} = \frac{3P^2C^{\frac{2}{3}}}{2A_1bh} \tag{2.4}$$

The most important output of the experimental campaign comes directly from the visual inspection of the test as presented in Figure 2.8.

During the mode I traction the fiber-bridging phenomena occurred, this experimental artifact modify the response of the specimen and drastically change the properties of the material. Fiber bridging has historically been ascribed to next-layer fiber nesting and weak interfaces as observed by Johnson [16], Crews [17] and Sakai [18]. This mechanism is more visible in a zoomed image such as Figure 2.9.

Fiber-bridging induces an alteration of the fracture toughness during the experiment. In fact, it enhances the mechanical properties of the laminate as it is possible to see in Figure 2.7. The fracture toughness increases during the crack growth, and it arrives at a constant value when the process zone is fully developed.

2.4. End notched flexure

The second test performed during the experimental campaign is the end-notched flexure. The configuration is the one described by the ASTM in [19]. This method aims to find the fracture toughness for pure mode II delamination. In this case, it is expected a common

Figure 2.8: Final configuration.

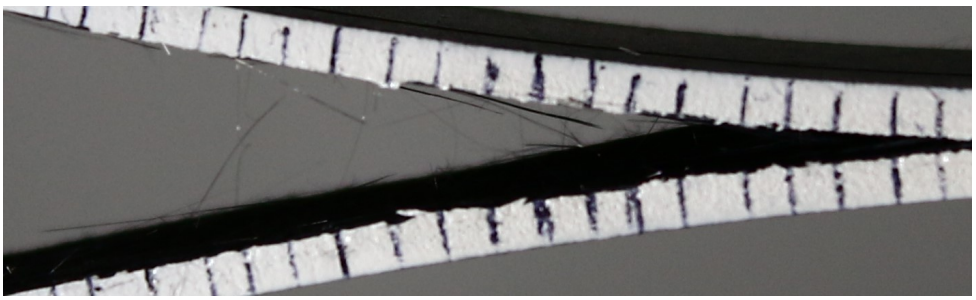

Figure 2.9: Experimental fiber bridging

material response. In fact, the delamination in the ENF happens suddenly, without the formation of the fiber bridging, the contact plies just slide one above each other. The configuration of the test is resumed in Figure 2.10.

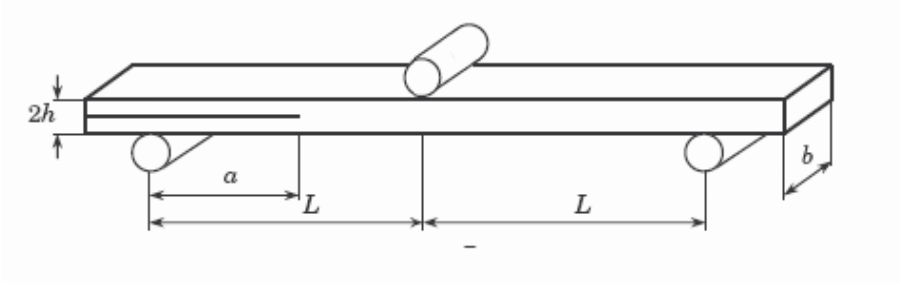

Figure 2.10: ENF test configuration

The specimen has the same characteristics as the DCB one, the only difference is that this one does not require attachments, such as the hinges in the previous configuration. The pre-cracked laminate is supported by two steel cylinders with a standardized diameter and a third cylinder is used to apply a controlled displacement load. The position of the load is changed throughout the test. At first, the compliance of the specimen is computed by two loading-unloading cycles, the load point is placed at 20 and 30 mm. The experimental results are reported in Figure 2.11.

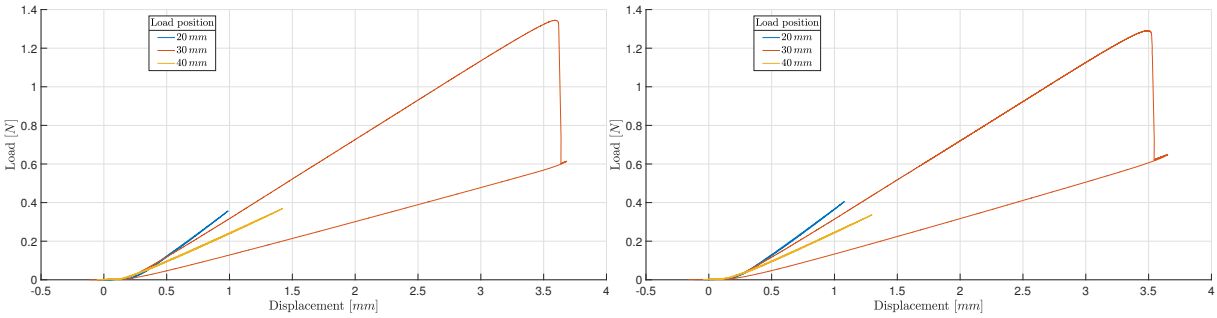

Figure 2.11: End notched flexure experimental tests

The ENF experimental campaign is not been a success, in fact, the crack propagation happens suddenly. This jump is represented in the load-displacement curve, it manifests a problem in the specimen creation or in the test configuration that has not been detected. This issue has not been solved and it will be a matter of interest in further developments.

3 | Numerical approaches to delamination

Differently from other study cases in the numerical analysis of fractures, delamination is a phenomenon that occurs in a prescribed direction. From a mesoscale point of view, this sentence is not correct, in fact, the propagation of delamination does not follow a precise fracture plane but it is influenced by many properties of the materials such as defects of any kind, this causes a propagation that has some fluctuation. This fluctuation is considered to contribute in a negligible manner to the large-scale phenomena studied, it could be more interesting for a mesoscale analysis. Historically the numerical assessment of delamination has been conducted with two different approaches based on different assumptions, the first is based on fracture mechanics while the second is on damage evolution. Traditionally these two categories have been exploited the most, however different numerical techniques such as the extended finite element method [20] have been used in this application. These tries are more based on a numerical experiment fashion, in fact, they are fitted the most for problems in which the direction of propagation is a matter of interest.

3.1. Review of numerical methods

3.1.1. Mechanical Description of Discontinuous Deformation

Considering a general continuum body, that has a boundary part with a constrained displacement and applied distributed force and an already existing crack as defined in Figure 3.1 [21].

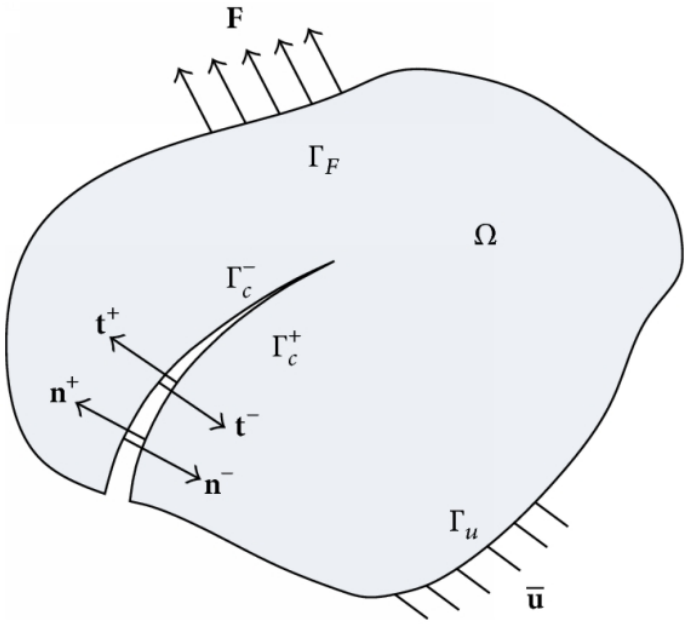

Figure 3.1: Body with discontinuity

In the infinitesimal small strain regime, the governing equation of the entire body except for the crack region is described as [22] and it is reported in Equation 3.1.

$$\nabla \sigma = \mathbf{f} \qquad in\ \Omega \tag{3.1}$$

In the considered case the governing equation shall be flanked by a series of boundary conditions that allow the solution of the differential problem. In the region Γ_F the body is subjected to a load, in Γ_u to a known displacement, and in the crack part Γ_c on both sides of the aperture, Γ_c^+ and Γ_c^-, the traction caused by the crack. The conditions are formalised in Equation 3.2.

$$\begin{cases} \sigma \cdot \mathbf{n} = \mathbf{F} & on\ \Gamma_F \\ \mathbf{u} = \bar{\mathbf{u}} & on\ \Gamma_u \\ \mathbf{t}^+ = \sigma \cdot \mathbf{n}^+ = \mathbf{t} & on\ \Gamma_c^+ \\ \mathbf{t}^- = \sigma \cdot \mathbf{n}^- = \mathbf{t} & on\ \Gamma_c^- \end{cases} \tag{3.2}$$

In the previously mentioned infinitesimal small strain and displacement regime it is assumed an elastic response of the material surrounding the crack. It is then defined a

constitutive tensor $\mathbb{C}$ and the strain tensor ε.

$$\begin{aligned} \sigma &= \mathbb{C} : \varepsilon \quad (\text{ in } \Omega \backslash \Gamma_c)\,, \\ \varepsilon = \varepsilon(\mathbf{u}) &= \frac{\left[\nabla \mathbf{u} + (\nabla \mathbf{u})^T\right]}{2} \quad (\text{ in } \Omega \backslash \Gamma_c) \end{aligned} \tag{3.3}$$

The displacement must be one of the kinematically permissible displacements listed in Equation 3.4.

$$\mathbf{u} \in \mathbf{U} = \{\mathbf{v} \in \mathbf{V} : \mathbf{v} = \mathbf{0} \text{ on } \Gamma_u\} \tag{3.4}$$

In many computational approaches to differential problems, it is applied the principle of virtual work. A weak formulation of the problem permits obtaining in a single equation the governing equation and all the boundary conditions. The integral form is then easier to be solved with approaches such as the Ritz[23] and FEM methods [24]. In this load case, the variational principle is written in Equation 3.5 as suggested in [25] [26].

$$\int_\Omega \sigma : \varepsilon(\mathbf{v}) \mathrm{d}\Omega + \int_{\Gamma_c} \mathbf{t} \cdot \mathbf{w}(\mathbf{v}) \mathrm{d}\Gamma = \int_{\Gamma_F} \mathbf{F} \cdot \mathbf{v} \mathrm{d}\Gamma \quad \forall \mathbf{v} \in \mathrm{U} \tag{3.5}$$

The variational principle is then rearranged in order to take into consideration the numerical approximations involved by the method selected. Depending on the approach selected to model the crack however the variational principle can be applied differently. In this case it is presented the FEM approach with cohesive elements, that will be reviewed in subsection 3.1.3. The new formulation as proposed by Spring [27] is reported in Equation 3.6.

$$\left[\int_\Omega \mathbf{B}^T \mathbb{C} \mathbf{B} \mathrm{d}\Omega + \int_{\Gamma_c} \mathbf{N}^T \frac{\partial \mathbf{t}}{\partial \boldsymbol{w}} \mathbf{N} \mathrm{d}\Gamma_c\right] \mathbf{u} = \int_\Gamma \mathbf{F} \mathrm{d}\Gamma \tag{3.6}$$

Where $\mathbf{N}$ is the shape functions tensor and $\mathbf{B}$ is the strain displacement matrix.

3.1.2. Virtual crack closure technique

One of the most popular methods for predicting fracture propagation is the virtual crack closure method[28]. This method is based on Irwin's hypothesis [29] that, when a crack grows just a little bit, the energy produced in the process is equivalent to the work needed to shrink the crack back to its original size. The break will spread if the energy released per unit area is greater than or equal to the critical value, G_c. The nodal forces and displacements derived from the solution of a finite element model may be used to calculate the mode I, mode II, and mode III energy release rates, G_I, G_{II}, and G_{III},

respectively [30].
Considering a finite model such as the one represented in Figure 3.2, where non-filled node is the crack tip, u,v and w are the horizontal,vertical and out-of-plane displacement, in the $x-y-z$ directions.

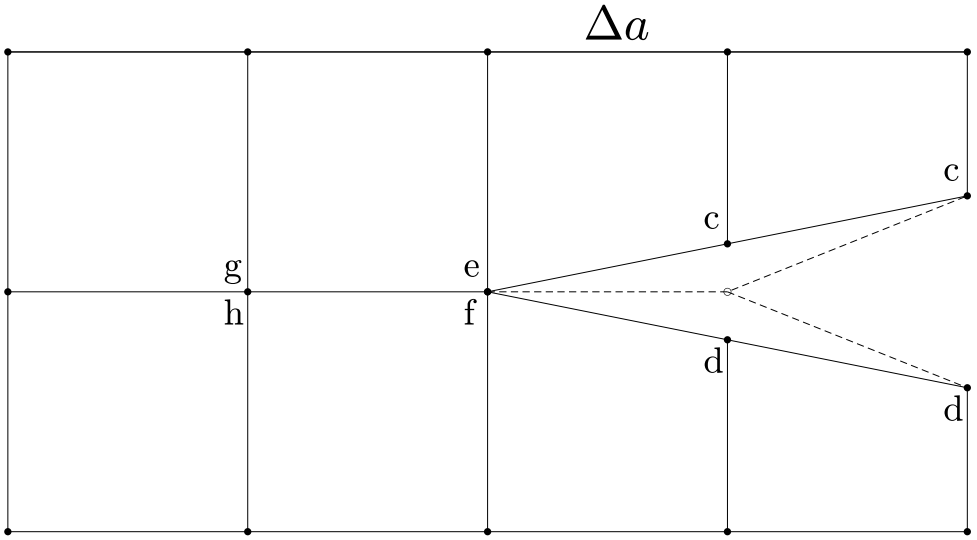

Figure 3.2: VCCT scheme

The energy released during the crack propagation is equal to the work required by the nodal forces to close the gap as reported in Equation 3.7.

$$G_I = \frac{1}{2b\Delta a} F^y_{cd}(v_c - v_d) \qquad G_{II} = \frac{1}{2b\Delta a} F^x_{cd}(u_c - u_d) \qquad G_{III} = \frac{1}{2b\Delta a} F^z_{cd}(w_c - w_d) \tag{3.7}$$

where F^k_{ij} is the nodal force between nodes i and j in the k direction. However, utilizing the assumption put out by Rybicki and Kanninen [31], the analysis may be simplified. They stated that the values of the nodal forces in Equation 3.7 can be substituted by the equivalent components of nodal forces F_{ef} in the three directions.
Once the nodal forces are computed the three components of the energy released are computed and summed together to obtain G_T.

$$G_T = G_I + G_{II} + G_{III} \tag{3.8}$$

The model predicts crack propagation when the energy release computed is equivalent or greater than the fracture toughness of the material $G_T \geq G_c$.

The VCCT method is useful because it deals with energy rather than stress, this is a huge advantage because it easier to be combined with experimental data. One of the main drawbacks of this approach is related to the self-similar assumption on the computation of the nodal forces, this method requires an already existing crack to work with, so it is not suitable for un-cracked bodies and short crack parts. Moreover this method is the mesh dependent, and it requires a extreme refined one to obtain fair results, there is not a modular response of the interface but only an abrupt change in the configuration.

3.1.3. Cohesive zone modeling

In the field of damage evolution modeling the most historically important progress has been obtained through the theorization of the cohesive zone. Cohesive zone modeling is a numerical artifact that aims to model the degradation of material during the crack propagation phase. The main reason of the born of this numerical method has been the need to obtain a clear representation of the high non-linearities experimented on the crack regions during crack propagation. This method has been exploited in various sectors interested in fracture mechanics, for example, to underline the wideness both in the frame of delamination for fiber reinforced polymers and for localized degradation in concrete for structural application. The first conceptualization of this method has been proposed by Dugdale [32], who understood that in crack propagation phenomena the stresses are limited by the yield stress and then it begins a plastic phase. Barembratt [33] subsequently, studying the equilibrium of elastic cracked bodies, firstly introduced the concept of the cohesive zone as forces generated at the molecular level that granted an intensification of stresses in the crack tip location. Finally, Hilderborg [34] stated the equilibrium problem differently moving from the molecular forces to tensile stresses, moreover from a static point of view it dealt also with crack evolution and cracks onset, Figure 3.3.

Cohesive zone modeling is based on the introduction on the material of interest of fictitious material, used only in the crack propagation path location, that has different properties with respect to the one of interest. This added material shall be used in a part of the numerical assessment characterized by a negligible thickness or in some cases, with numerical addition to avoiding singularities, of null thickness. This new material has a particular constitutive law based on a traction-separation relationship. This numerical model fits particularly well in the finite element (FE) context, due to the flexibility of FE respect to material description. Due to the easy implementation of the model, in particular in the commercial software environment it has been implanted in a various manners. In fact, normally cohesive law can be applied to standard iso-parametric elements. These

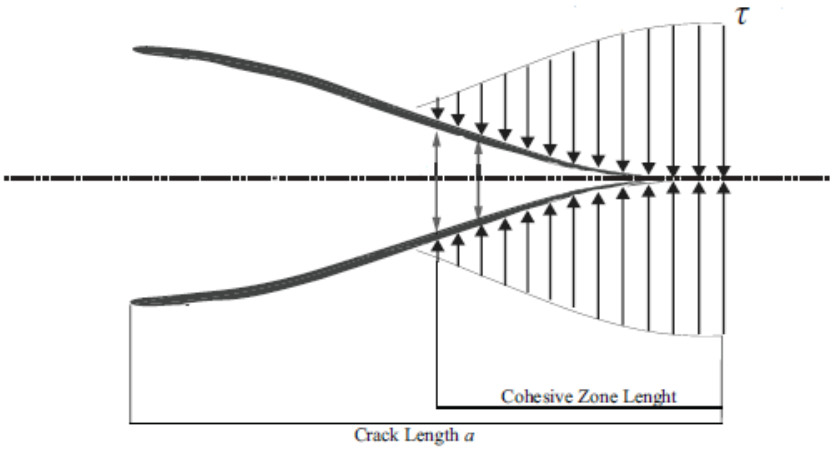

Figure 3.3: Hillerborh's cohesive model

elements behave such as a planar stress or strain element with a variable matrix stiffness that varies depending on the elongation of the element itself, so the implementation needs only the characterization of the constitutive law of a fictitious material. This last aspect links cohesive elements to plasticization phenomena due to the non-linearities present in the material description. From now on it will be referred to as 'cohesive law' as the constitutive relationship that links elongation and stresses.

3.1.4. Cohesive constitutive law

The constitutive law relates the displacement jump between the two surfaces, Γ^+ and Γ^- to the interface traction. The relative displacement jump is defined as Equation 3.9 and the element representation in Figure 3.4.

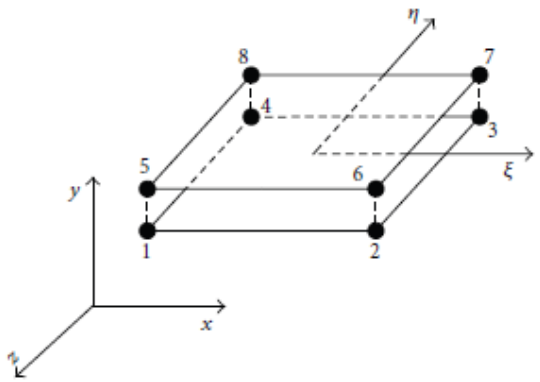

Figure 3.4: Cohesive element nodes jump

$$\delta_{rel}(\xi,\eta) = \sum_{i=1}^{4} \mathbf{N}_i(\xi,\eta)\,(\mathbf{u}_{i+4} - \mathbf{u}_i) \tag{3.9}$$

Once the relative displacement is transformed in local coordinates by means of a rotation, $\delta = T^T \delta_{rel}$, It is possible to formally express the constitutive laws in the material discontinuity as Equation 3.10.

$$\mathbf{t} = \tilde{t}(\delta) \tag{3.10}$$

Depending on the application different models have been proposed, some of them are illustrated in Figure 3.5.

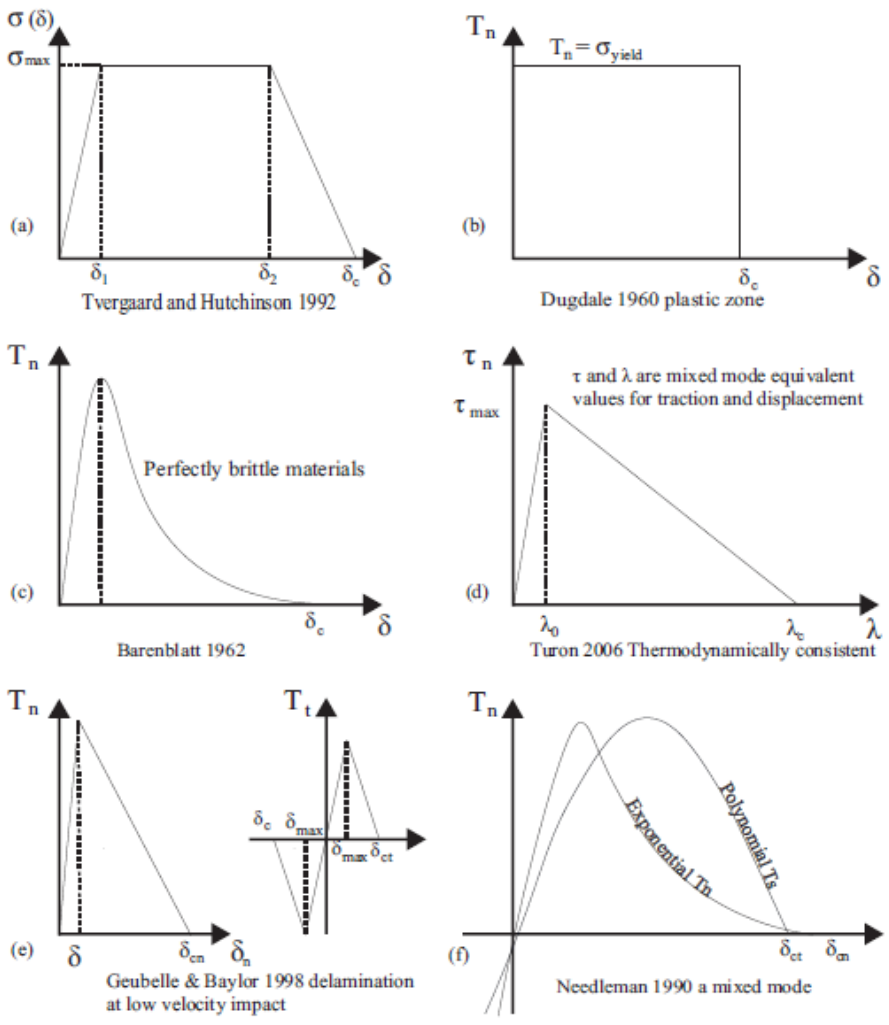

Figure 3.5: Cohesive law models

Besides the already mentioned Dugdale and Barenblatt, Tvergaard and Hutchinson proposed a trapezoidal law [35], then slightly modified by Cui et all [36], in the field of elastoplastic materials and in the study of adhesive joints. Xu and Needleman [37] proposed an exponential model, which considered the mixed mode effect too. Geubelle [38] and Turon [39] developed bi-linear law. From now on it will be considered the cohesive law as a traction separation law (TSL) in particular a damage law. The major emphasis is reserved for the evolution of the damage as a function of the element separation. The traction separation law in the field of damage evolution can be written as Equation 3.11.

$$\begin{bmatrix} t_n \\ t_{s1} \\ t_{s2} \end{bmatrix} = \left(\mathbf{I} - \begin{bmatrix} D_1 & 0 & 0 \\ 0 & D_2 & 0 \\ 0 & 0 & D_3 \end{bmatrix} \right) \begin{bmatrix} k_1 & 0 & 0 \\ 0 & k_2 & 0 \\ 0 & 0 & k_3 \end{bmatrix} \begin{bmatrix} \delta_1 \\ \delta_2 \\ \delta_3 \end{bmatrix} \tag{3.11}$$

That can be rearranged in a compact form as Equation 3.12.

$$\mathbf{t} = (\mathbf{I} - \mathbf{D}(\delta))\mathbf{K}\delta \tag{3.12}$$

The $\mathbf{K}$ is the matrix of the stiffness parameter, in the 3 direction, of the cohesive element before the onset of the damage. Depending on the material analyzed and the purpose of the analysis the 3 parameters can present the same characteristics both in the normal and shear directions, or they can be characterized by a normal to shear stiffness ratio.

3.1.5. Bi-linear cohesive law

The easiest cohesive law is a perfectly rigid element endowed with a linear damage increase. This method allows considering the element only for its decrement in stiffness, starting from an infinite one. The law is represented in Figure 3.6. This relationship however shares with infinitely rigid elements some computational issues and it causes several convergence problems during simple analysis. In many FE models of real structure even if theoretically speaking a rigid connection shall be needed a high modulus spring is introduced to speed up the computation and smooth the analysis. Usually, a high modulus spring that substitutes a rigid link it is called penalty stiffness.

The same approach is applied in this field where a high elastic response is added before the start of damage begins. This penalty term gives the origin to the classical 'bi-linear' cohesive law represented in Figure 3.7. There is an elastic response until a certain separation and then the degradation starts. The separation at which the degradation starts has a small magnitude compared to the rest of the cohesive law and due to the limited

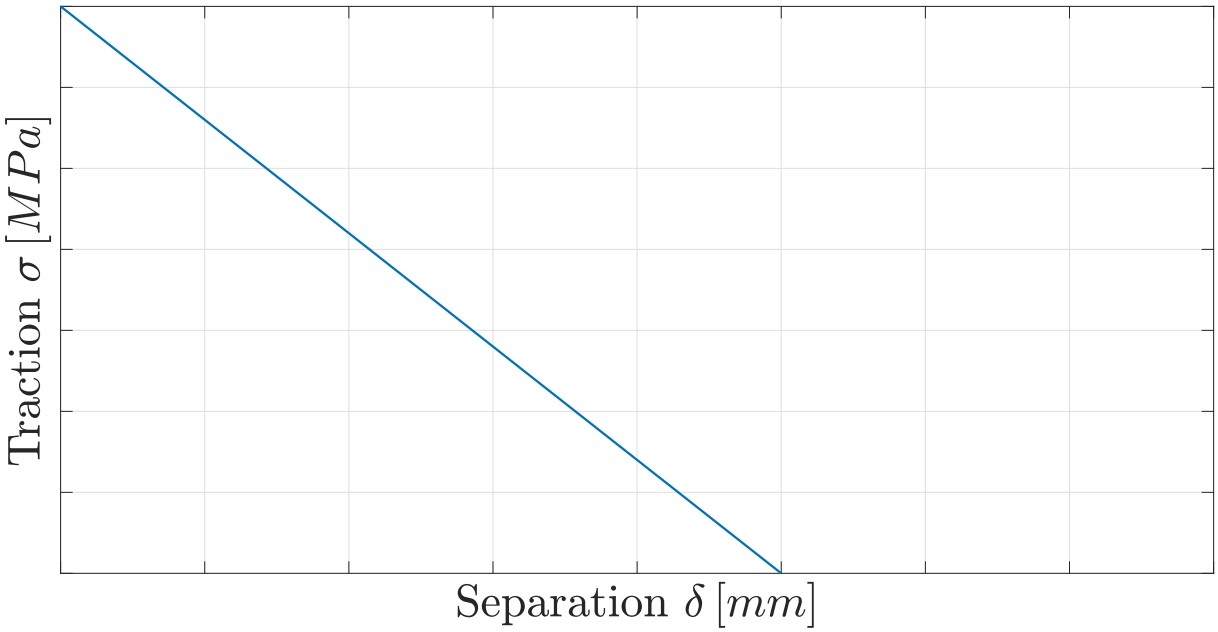

Figure 3.6: Rigid cohesive law

maximum traction experimented by the element as expected the elastic modulus of the first part is of high order, in literature, such as Dogan [40] and [41],it is widely referred to $10^4 MPa$ or even more. As in the first case after the end of the linear damage evolution the traction response of the element is null, the first point of this zone, the ultimate degradation of the element determines the end of life of the element itself, after that in fact the element reaches the complete degradation and the model can eliminate it.

Different implementations can lead to the same law, in this case, is selected the method as represented in Figure 3.7. The considered approach is only valid for the pure mode I crack. The end of the elastic response part is dictated by a maximum strength σ_0 at a separation δ_0 and the end of life of the element is indicated through the maximum separation δ_f.

$$\begin{cases} D = 0 & if\ \delta \leq \delta_0 \\ D = \dfrac{\delta_f\left(\delta - \delta_0\right)}{\delta\left(\delta_f - \delta_0\right)} & if\ \delta_0 < \delta < \delta_f \\ D = 1 & if\ \delta \geq \delta_f \end{cases} \tag{3.13}$$

From zero through the fracture opening, the energy absorbed per unit area of the crack is in Equation 3.14.

$$G = \int_0^{\delta^*} \sigma d\delta \tag{3.14}$$

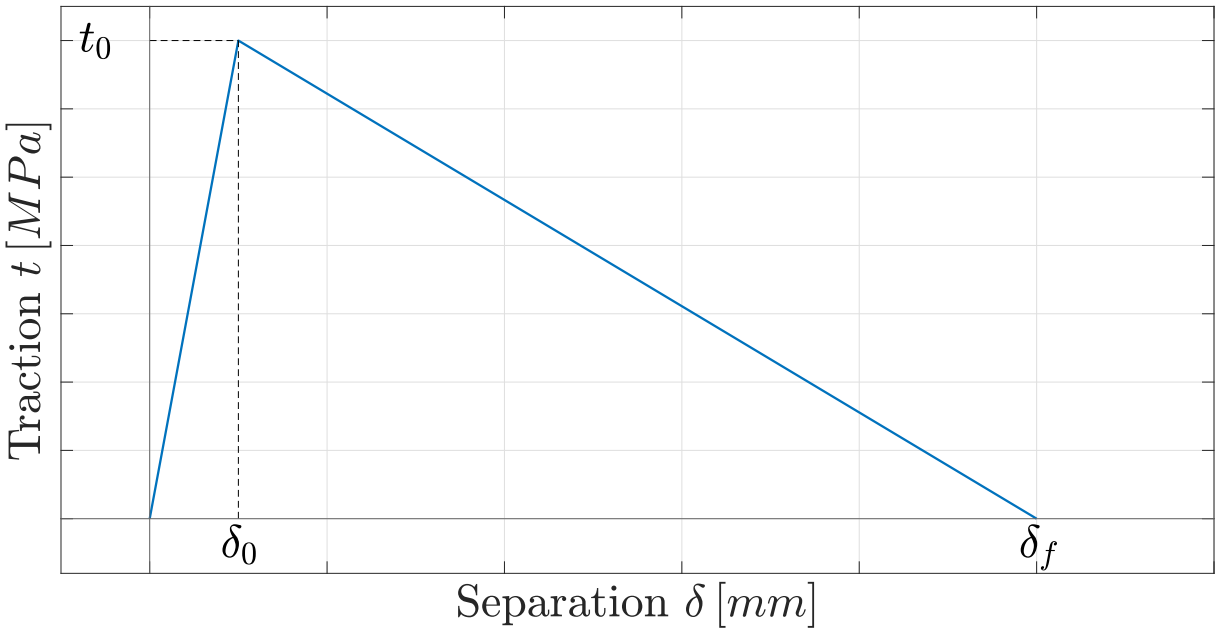

Figure 3.7: Bi-linear cohesive law

The surface area under the traction-separation curve is equivalent to this energy. When the CZM is fully developed, the cohesive zone dissipates its maximum amount of energy. At that point, the stress begins at 0 at the tip and steadily decreases to 0 at δ_f. In that situation, the energy is equal to the entire region under the traction-separation law, and new traction-free crack surfaces are produced for displacements greater than δ_f. This energy is equivalent to the material's crucial Energy release rate G_c. Figure 3.8 shows two distinct situations at two different separation conditions.

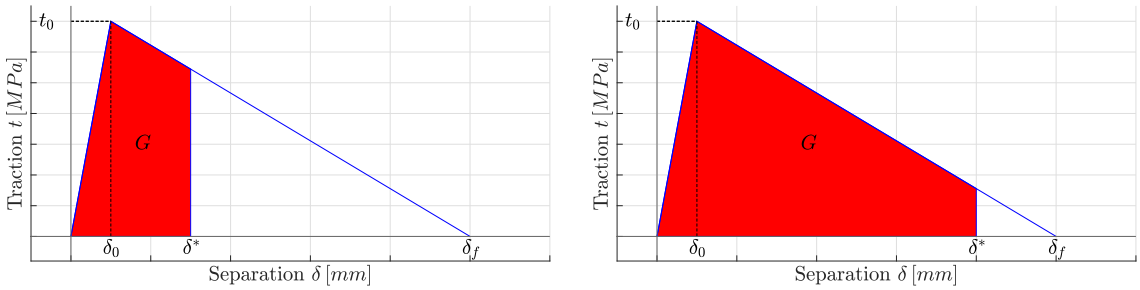

Figure 3.8: G function on TSL.

For mixed mode crack propagation, it is required a refined analysis of the crack onset and damage propagation, which can be faced with a separation combination such as Turon or Benzeggagh [39] [42], or through a potential-based model such as Park[43][44].

This model is suitable in particular in the case of brittle fracture, this condition is highly representative for many applications, such as concrete but also for carbon-reinforced

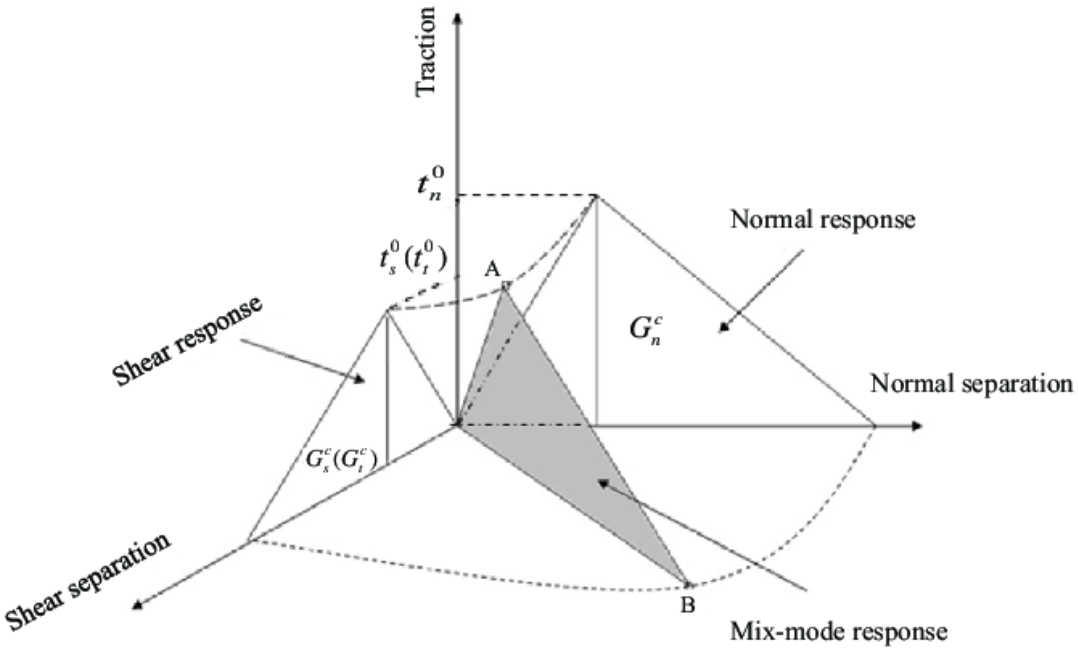

Figure 3.9: Mixed mode cohesive zone model

thermo-setting composites. This model is used for materials characterized by an R-curve that has a shape similar to Figure 3.10. However, this condition is not representative of the phenomena observed so a different model shall be considered.

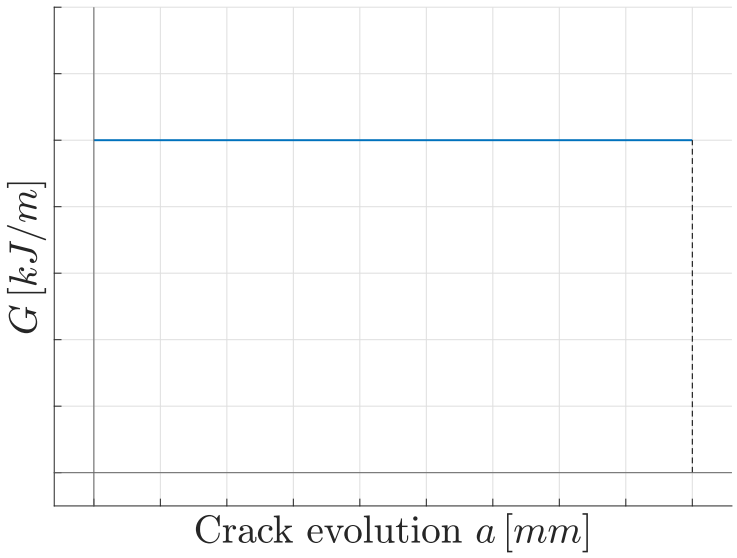

Figure 3.10: Constant R-curve

3.2. Numerical analysis of a tri-linear cohesive law

In the chapter 2 the evolution of the fracture toughness obtained during the experimental campaign has been analyzed. During the delamination, the laminate is subjected to the phenomenon of fiber bridging, which determines an increase in fracture toughness during the test. The R curve does not have the shape typical of common composites such as Figure 3.10 but it has an increasing behavior in the first part and then it reaches a steady state value Figure 3.11. Many models have been proposed to fill the gap left by the bi-

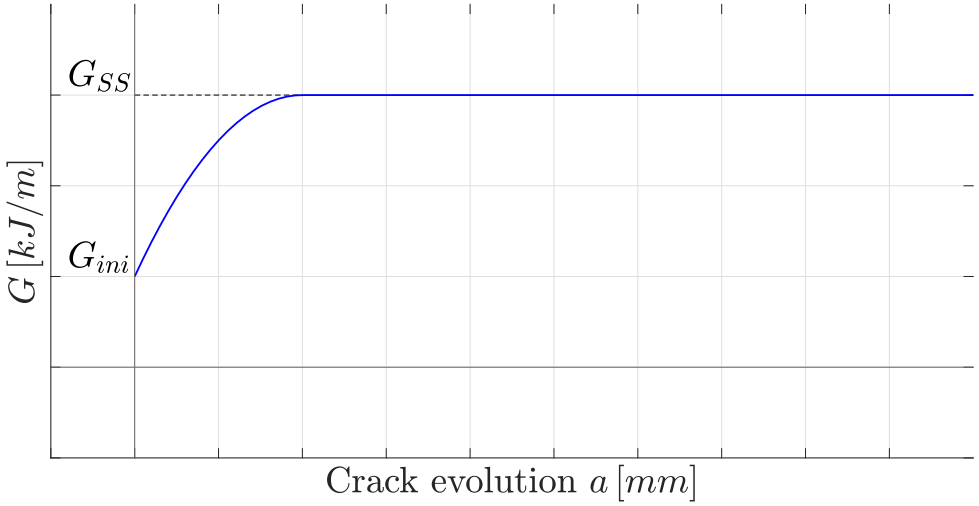

Figure 3.11: Variable R-curve

linear model in the description of the R curve, one of the most interesting is the tri-linear one which is just a continuation of the bilinear model in the increasing fracture toughness domain.

3.2.1. Bi-linear model issues

First, it is important to understand the bi-linear behavior to better qualify the objectives of a proposed cohesive law. It is used as a starting point the built-in Abaqus bi-linear cohesive law as a reference. The definition used is based on fracture toughness, so the area under the traction separation law. In the previous sections, the fracture toughness behavior has been formulated. In the experimental test it is possible to distinguish an initial and a steady state fracture toughness. The comparison, reported below, uses the same formulation of the cohesive except for the fracture toughness G. In the first case, it is considered the fracture toughness equal to the initial one, while in the second it is taken as the final one. This analysis's results are reported in Figure 3.12.

In this figure, the load-displacement curves of the two cases are represented. Both the

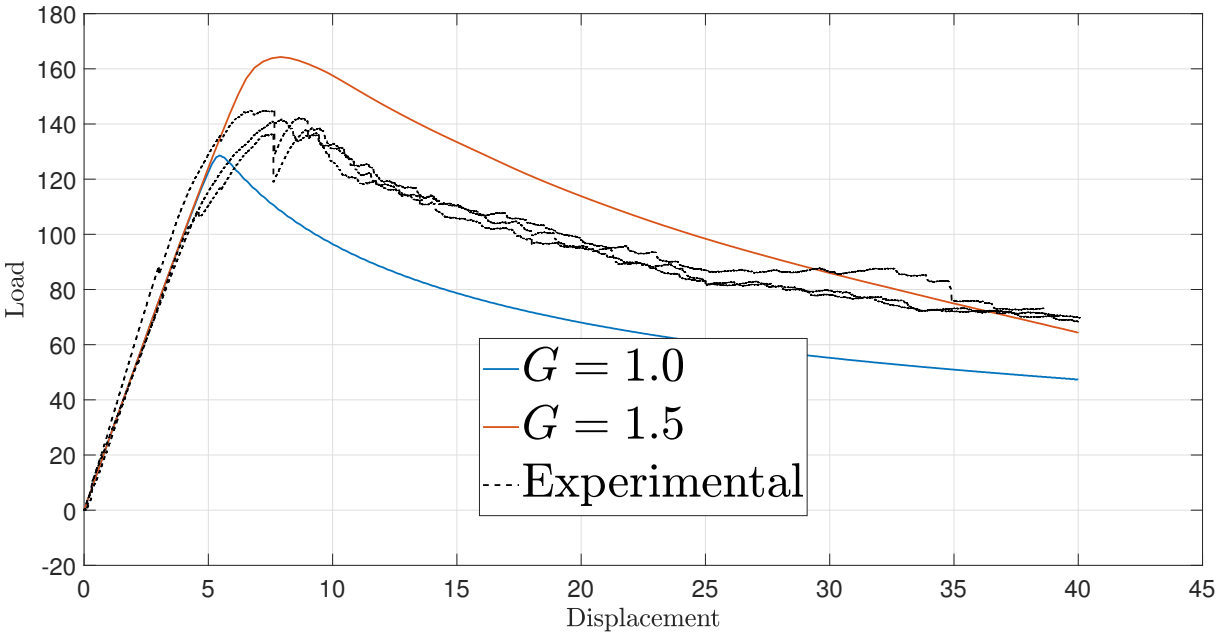

Figure 3.12: Bi-linear traction separation results

curves are far from the experimental one, however they catch a different particular of process. In fact, the lower value fracture toughness gives the beginning of the decreasing part of the curve, while the higher one the end part. This result explain better the necessity of a more complex cohesive law for this kind of material.
Another factor to be considered is the process zone of the fracture. Bi-linear models work fine with material characterized by a brittle behavior, where the crack is well localized and the process zone has a small extension. The higher fracture toughness process zone, the bigger one, is represented in Figure 3.13.

The process zone has a length close to $1\,mm$, far from the objective one.

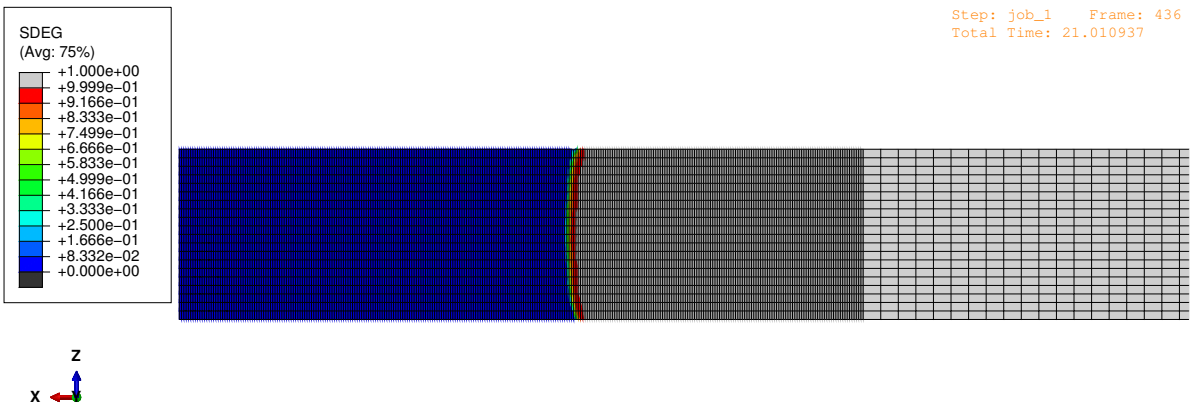

Figure 3.13: Bi-linear process zone

3.2.2. Tri-linear cohesive law

The conventional three-linear CZM suggested by Davila [45] and Heidari [46] is depicted in Figure 3.14. The two bilinear CZMs are supposed to peak at the same displacement jump δ_0. A three-linear CZM is produced by adding two arbitrary bi-linear CZMs that describe bridging phenomena. The blue line is a bilinear CZM that characterizes the quasi-brittle matrix fracture or microcracking development and has a small critical opening displacement (δ_a). The red line indicates a bilinear CZM that better describes fiber bridging by having a greater critical opening distance δ_f. The initial interfacial stiffness K, the interfacial strength, and the fracture toughness G are the three crucial characteristics that each bilinear CZM includes.

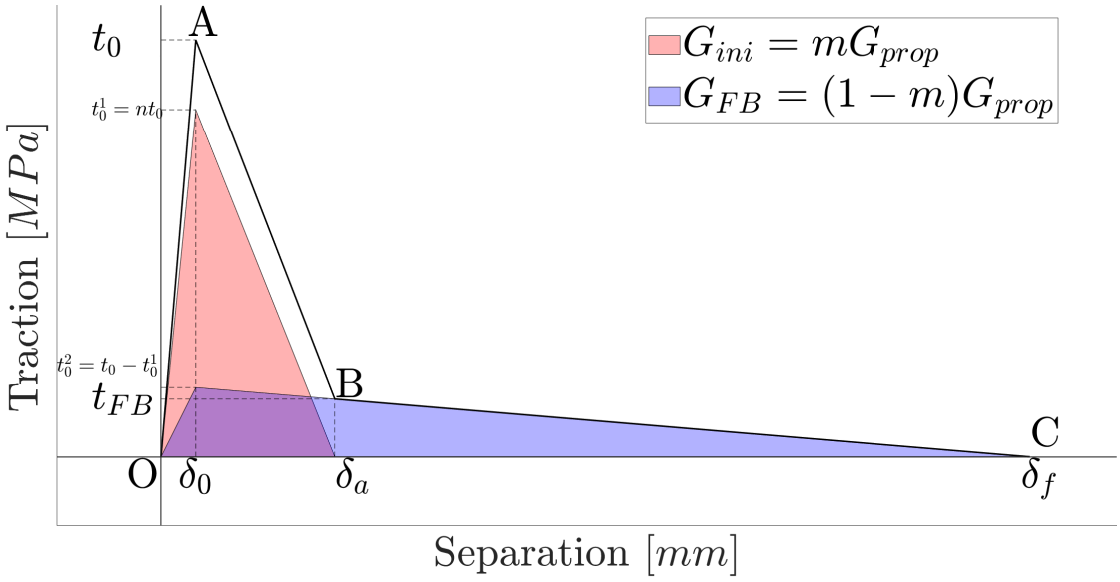

Figure 3.14: First version tri-linear TSL

The two bilinear laws are presented with proportional characteristic parameters, one for the maximum strength and one for the fracture toughness. The peak values of the two laws are respectively $t_0^1 = nt_0$ and $t_0^2 = (1-n)t_0$. While for the fracture toughness the relations are $G_{ini} = mG_{prop}$ and $G_{bri} = (1-m)G_{prop}$. The m and n parameters are called fracture toughness ratio and the strength ratio and can be defined as Equation 3.15,Equation 3.16.

$$m = \frac{G_{ini}}{G_{prop}} \tag{3.15}$$

$$n = \begin{cases} 1 - \frac{2}{3}\gamma \frac{(1-m)}{l_{\text{cz}}} \frac{E_z \cdot G_{\text{prop}}}{t_0^2} & \frac{m}{n} \leq \frac{1-m}{1-n} \\ \frac{2}{3}\gamma \frac{m}{l_{\text{cz}}} \frac{E_z \cdot G_{\text{prop}}}{t_0^2} & \frac{m}{n} > \frac{1-m}{1-n} \end{cases} \tag{3.16}$$

Where E_z is the laminate's Young modulus in the z direction,l_{cz} is the length of the process zone and γ is an experimental parameter that is usually equivalent to $\gamma = 0.884 l_{cz}$. Different studies have been conducted on the selection of the parameters of the traditional cohesive law. Airoldi and Davila [47] have used two procedures to identify the parameters, one through an experimental procedure looking at the R-curve and one numerical approach with the minimization of the error between the FEM and experimental load-displacement curves. A semi-analytical procedure for the estimation of the parameters has been proposed by Gutkin et al. [48]. The maximum stress in the fiber bridging region of the TSL can be computed as Equation 3.17.

$$t_{FB} = t_0(1-n)\left(1 - \frac{1-n}{n} \cdot \frac{m}{1-m}\right) \tag{3.17}$$

For simulating delamination propagation with large-scale fiber bridging, the CZM generated through superposition is effective. However, it is presumed that the two bi-linear law peak at the exact same displacement jump 0. The actual microscopic process of delamination failure does not support this notion.

In order to obtain a TSL that is more compliant with the experimental phenomena, it is used the law implemented by Gong et al. [49]. The reviewed three-linear CZM is depicted in Figure 3.15. The red and blue lines indicate bilinear CZMs that, respectively, characterize the quasi-brittle matrix fracture and the fiber bridging Both the interface and the fibers are subject to tensile tension at the beginning. The fibers, however, are unable to span the delamination faces because they are not pulled away from the matrix. The interfacial traction is dominating and significantly greater than the bridging adhesion in this situation. The interface rapidly deteriorates with a diminishing load capability as the crack opening displacement rises. The bridging fibers are enveloped by the matrix and the bridging tension is rather small because the complete delamination has not yet occurred. Only when the two faces are separated the fibers detach from the matrix and originate the bridging. There is an onset of a new interface with a new tensile strength only after the matrix detachment. When the two bridged surfaces reach a determined separation the tensile resistance of the fibers is overcome and no traction remains. There is a clear separation between the two moments, during the first stage the matrix opposes to the separation and it occurs the classic brittle resistance then there is a second stage

in which the matrix is no more present but some fibers remain attached to the opposite surface and generate a second-hand traction. The two phenomena are disconnected, this consideration is omitted in the previously mentioned tri-linear cohesive law, where the two bilinear super-imposed TSL peak at the same displacement. In this method, the peak of the fibers strength is moved to the moment in which the matrix completely fails.

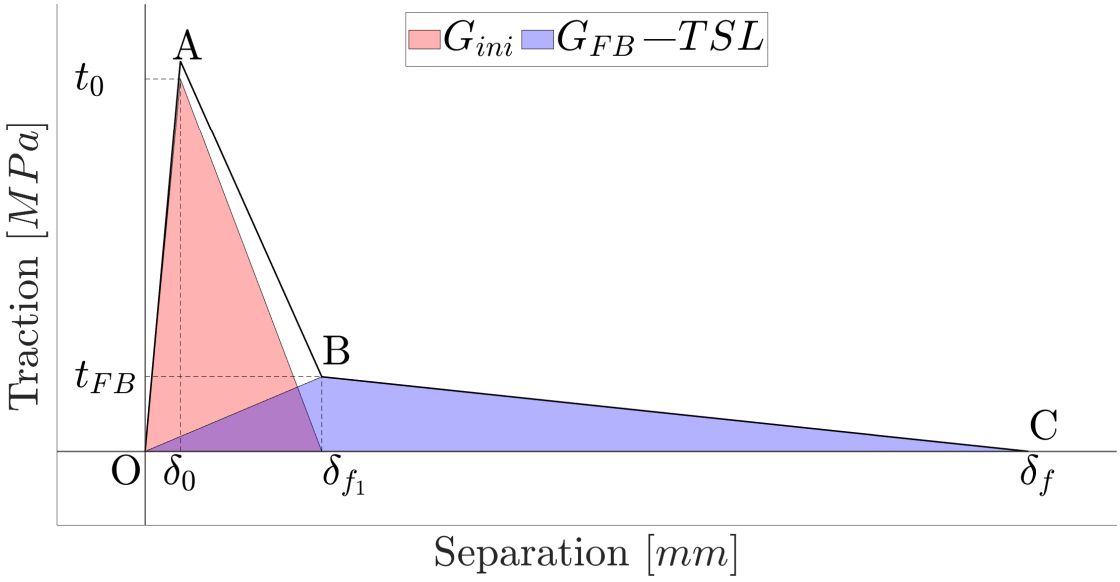

Figure 3.15: Second version version tri-linear TSL

The TSL for the mode I tensile response can be written as Equation 3.18.

$$t = (1 - d)K_0\delta \tag{3.18}$$

The damage function is formalized as a piece-wise defined function, characterized in each part by a slope. The damage function is written in Equation 3.19.

$$d = \begin{cases} 0 & \delta \leq \delta_0 \\ \left(1 - \dfrac{K_{\mathrm{AB}}}{K_0}\right)\left(1 - \dfrac{\delta_0}{\delta}\right) & \delta_0 < \delta \leq \delta_{\mathrm{f_1}} \\ 1 - \dfrac{K_{\mathrm{BC}}}{K_0}\left(1 - \dfrac{\delta_{\mathrm{f}}}{\delta}\right) & \delta_{\mathrm{f_1}} < \delta \leq \delta_{\mathrm{f}} \\ 1 & \delta > \delta_{\mathrm{f}} \end{cases} \tag{3.19}$$

Where the slope of segments are delineated in Equation 3.20.

$$\begin{cases} K_{0A} = K_1 + K_2 \\ K_{AB} = \dfrac{t_b - (t_0 + K_2\delta_0)}{t_{fb} - t_0} \\ K_{BC} = \dfrac{t_b}{\delta_{f_1} - \delta_f} \end{cases} \tag{3.20}$$

3.2.3. Algorithm implementation

The constitutive law discussed in the previous section is implemented in the commercial FEM software ABAQUS [50]. Many elements for both structural and fluid dynamics applications are implemented in Abaqus. In this field there is also the possibility to use cohesive elements implemented both as 2D-3D elements but also there is the possibility to use cohesive law as surface contact. In the mentioned platform two cohesive model are already present, the bi-linear and the exponential ones. The bilinear law will be used in the next sections in order to discuss the advantages found by the implementation used. One of the main advantages of the software, in the academic environment, is the possibility to use user-defined material law. The user subroutine is called UMAT, where the user can implement the subroutine written in FORTRAN programming language [51]. The UMAT subroutine is called during each iteration of the FE analysis in all the integration points considered. The subroutine requires the definition of some parameters at the beginning of the analysis, that are not updated during the iterations. At each step, the routine has as input parameters, besides the UMAT properties, the strain, and stresses at the previous step plus the strain increment of the iteration step. The routine can update some parameters called state variables during the process, these state variables are both an input for the subsequent step but also a user-visible output. The main outputs of the subroutine are the stresses increment and the tangent stiffness matrix required for the solution of the variational principle Equation 3.5. The flow chart of the discussed application is reported in Figure 3.16. Due to the high non-linearity of the problem, the analysis of this cohesive law is subjected to severe convergence problems. Different solutions can be found to curb the phenomena, for example, it is required a fine mesh and the use of small integration steps. It is also implemented in the subroutine a viscous regularization that allows the smoothness of the response and a higher convergence rate during the analysis that, if used with the correct parameters, does not influence the goodness of the results. It is used a Duvaut-Lions viscous regularization technique [52], already implemented in the field of cohesive elements by Caggiano [53] and Viñuela [54]. This regularization works with the damage parameter and its increment from the previous step. The regularized damaged variable formula is reported in Equation 3.21.

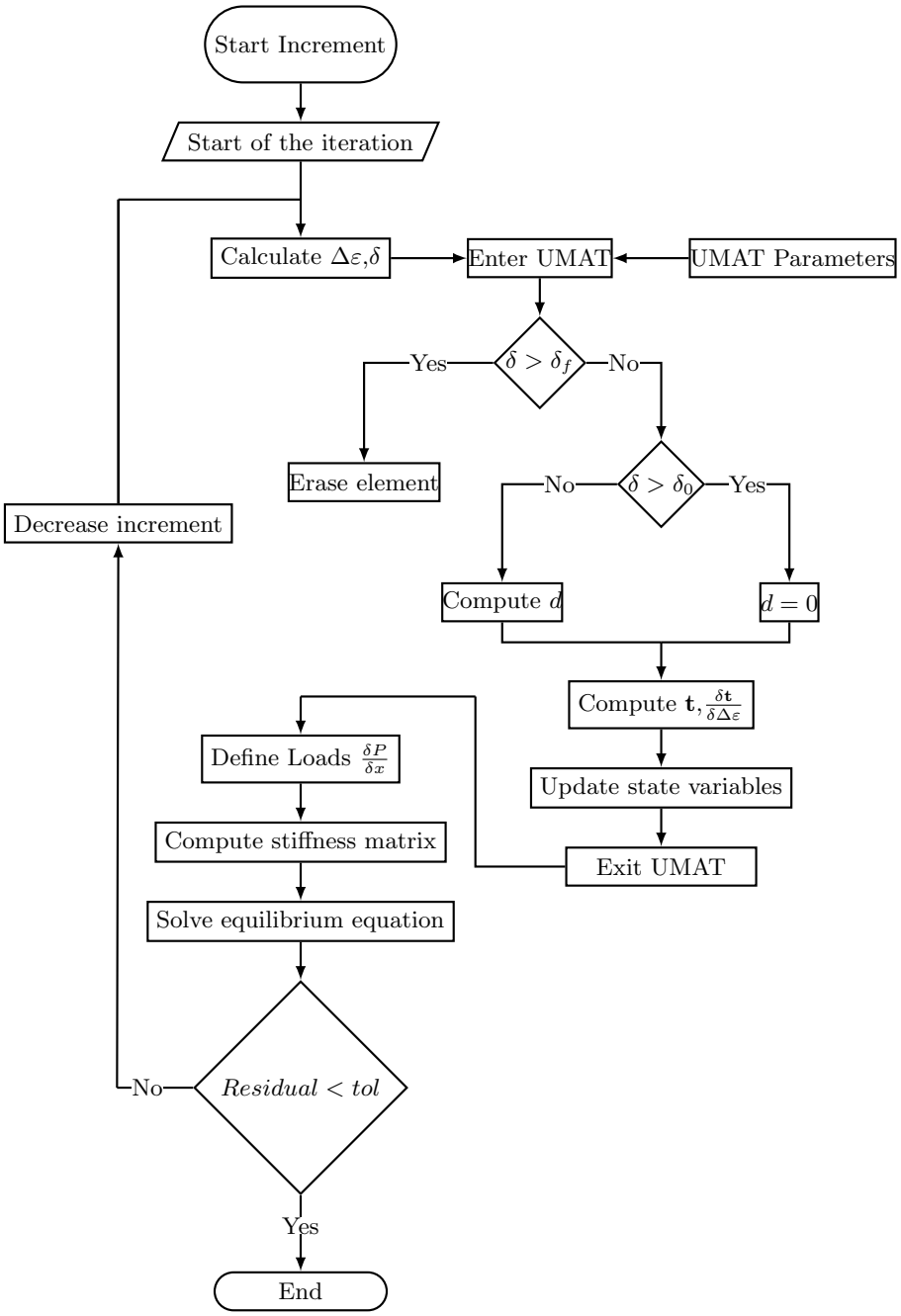

Figure 3.16: Static UMAT implementation.

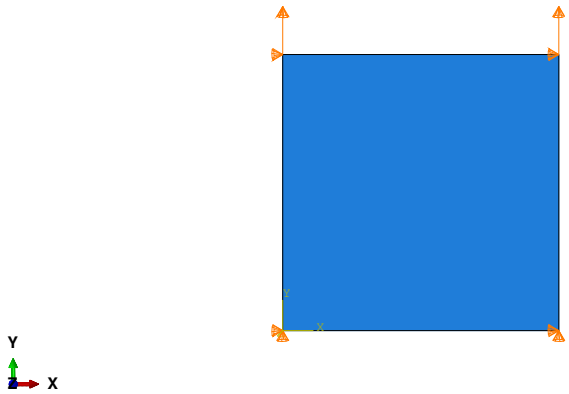

Figure 3.17: 1D test configuration

$$d_v = \left(\frac{\mu}{\mu + \Delta time}\right) d_n + \left(\frac{\Delta time}{\mu + \Delta time}\right) d_{n+1} \tag{3.21}$$

3.2.4. 1D FEM test

The first analysis to be carried out when dealing with a new UMAT is the 1D approach. This analysis is taken into consideration a single element that is stretched in order to see the response in correspondence to a prescribed displacement. In Figure 3.17 it is represented the 1D analysis configuration.

The single element, in this case, is presented in a 2D configuration, the same could be replicated also the 3D environment. The bottom two nodes are fixed while at the upper two is applied a vertical displacement. The magnitude of the displacement is equal to the maximum separation expected for the cohesive law. If the UMAT implementation is correct the traction separation law obtained is the same as the one prescribed theoretically. It is retrieved the displacement and the stress in the vertical direction. The two arrays combined together are reviewed in Figure 3.18.

The UMAT after this brief analysis is considered validated.

3.2.5. 3D FEM analysis

In this section, the FEM model of the DCB test is built in ABAQUS. After a small presentation of the model the results of the analysis conducted with the tri-linear cohesive law presented are reported.
The model has a simple shape and it is composed of two laminae connected by a layer of cohesive elements. The implementation uses only two typologies of elements, the com-

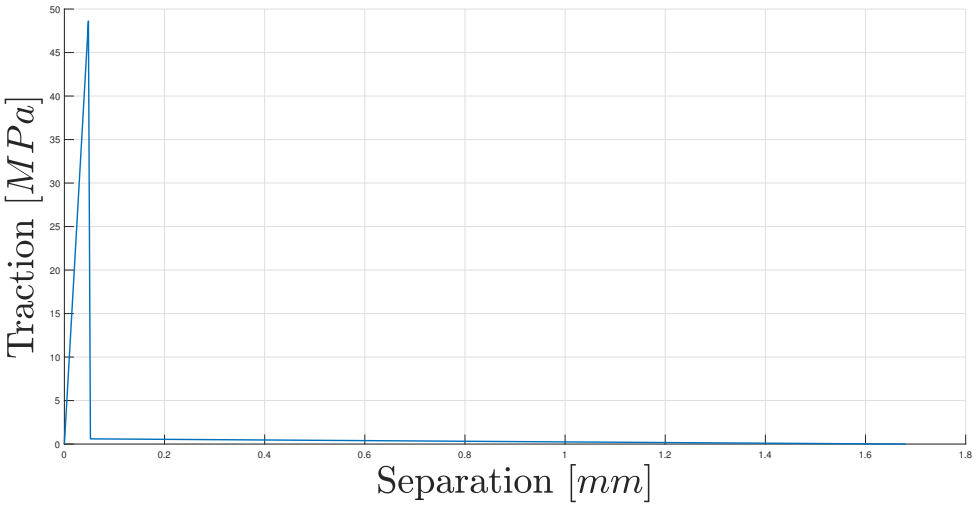

Figure 3.18: 1D traction separation

Part	Element type	Number
Laminate	Plane Stress	
Interlaminar	Cohesive elements	

Table 3.1: Tri-linear cohesive optimization parameters.

posites are modeled with plane stress elements endowed with an orthotropic material definition and the cohesive elements. The geometry is taken equal to the one presented in chapter 2, the only difference is the cohesive layer with a height of 0.001 , a measure that does not alter the behavior. The Abaqus's elements used are reviewed in Table 3.1.

In Figure 3.19 the model with the boundary conditions is represented. As it is possible to see there is different element popularity between the first part of the laminates and the second, this has been done in order to increase the number of elements the cohesive region. Increasing the number of elements in the crack direction allows the system to have fewer distorted elements during the delamination analysis.

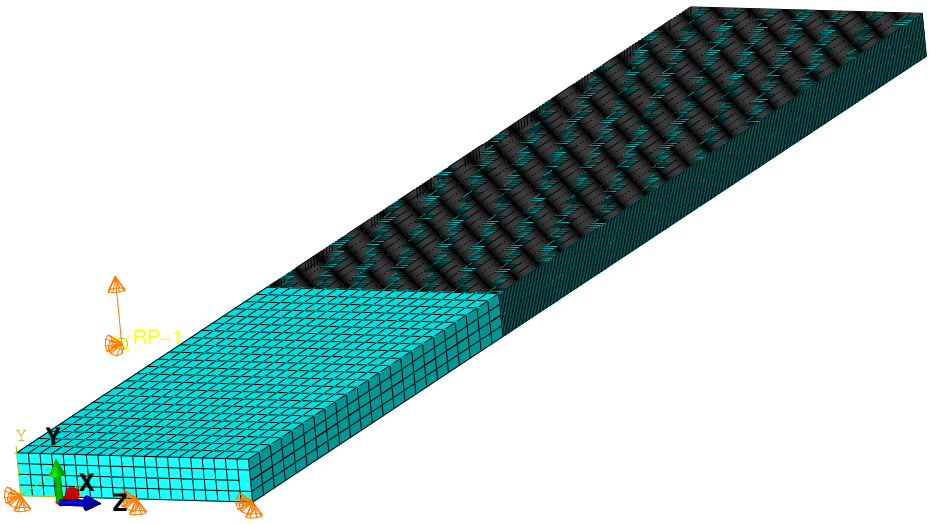

Figure 3.19: 3D FEM mesh and BC

The encastre constraint on the bottom cantilever is directly applied at an element level while the upper part is constrained through a rigid element to a reference point. The displacement is then applied to the reference point, this has been done to retrieve easier the reaction force committed by the specimen against the separation. A displacement of $40\,mm$ is applied, the same as to the experimental test, this moving constraint is applied with a ramp law, in order to have a progressive convergence during the non-linear analysis.

The nine engineering constants required to describe an orthotropic material are reported in Table 3.2. The laminate has been produced with unidirectional plies, so the parameters obtained are the one of a single ply.

The parameter of the cohesive elements are the one discussed in the previous section, and they are summarized in Table 3.3.

The displacement map at the end of the test is pictured in Figure 3.20.

The displacement contour plot is compliant with the experimental one. The part of the laminate interested in which the delamination occurs remain parallel to the floor, only the two flaps change the disposition. Some modeling approach for the DCB test uses an rigid element to block the relative motion of the laminate part in contact with the test

Parameters	Unit	Value
E_{11}	MPa	13000
E_{22}	MPa	10300
E_{33}	MPa	10300
ν_{12}	–	0.3
ν_{13}	–	0.3
ν_{23}	–	0.3
G_{12}	MPa	5200
G_{12}	MPa	5200
G_{12}	MPa	5200

Table 3.2: PEKK parameters.

Parameters	Unit	Value
K_I	MPa/mm	10^4
K_{II}	MPa/mm	-
t_0	MPa	50
t_{FB}	MPa	0.7
G_{ini}	kJ/m^2	1.0
G_{SS}	kJ/m^2	1.5

Table 3.3: Cohesive element parameters.

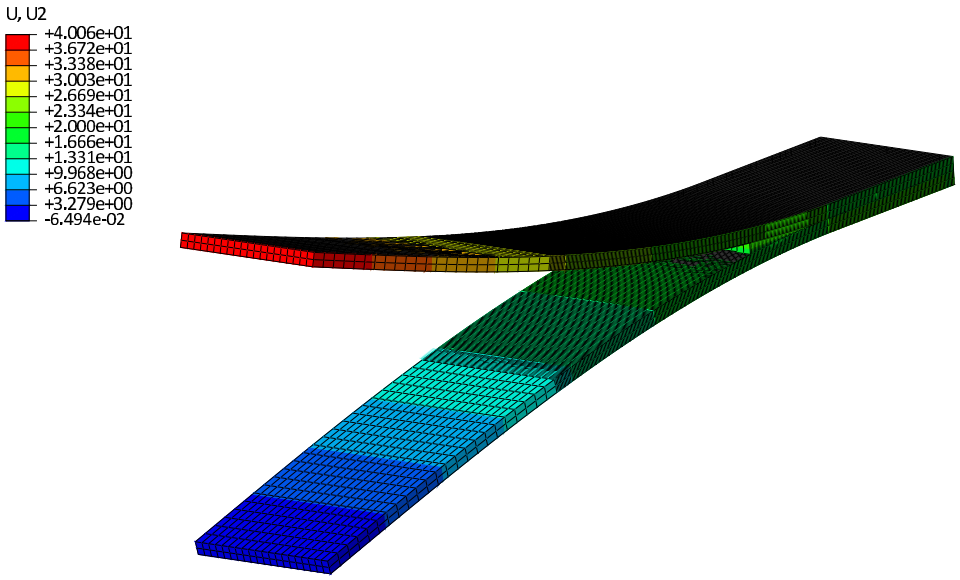

Figure 3.20: 3D displacement results

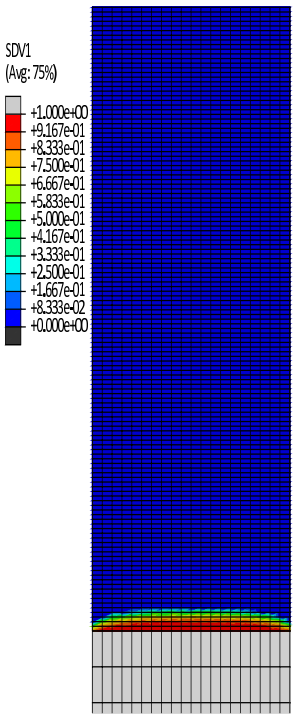

Figure 3.21: SDV1 beginning

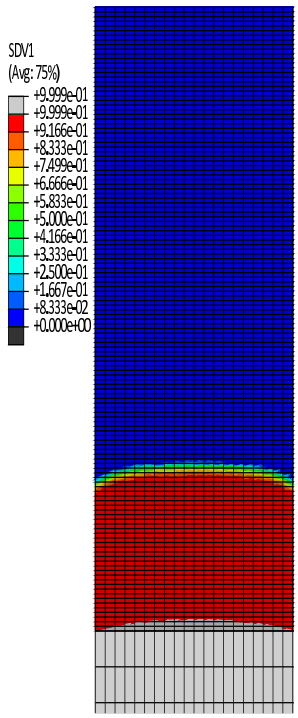

Figure 3.22: SDV1 detachment

hinges. This constraint aims to avoid a deflection of last part of the beams. Even if in this model it has not been added this feature the two beam does not deflect at the end. The constrained is avoided to introduce a possible source of error due to the excessive rigidity that increase the numerical weight of he entire system.
One of the main advantage of a cohesive law characterized by a higher maximum separation δ_f is the possibility to model the long process zone that is characteristic of the fiber-bridging phenomena. The length of this region is difficult to be detected from the experimental measure because it is not possible to understand at which stage of the degradation of the bridging fibers they end to contribute to the traction. That being said changing the parameters of the degradation law it is possible to obtain a correct fiber-bridging process zone.
During the first part of the displacement increasing the degradation of the elements remains almost unaltered, there is only the linear deflection of the beam and the interlaminar part is barely not interested. Once the deflection starts affecting the interlaminar part the degradation of the cohesive elements starts showing. In Figure 3.21 the beginning of the degradation of the cohesive layer is pictured.

The picture represents the degradation parameter D on the cohesive elements, right after the end of the linear part of the load-displacement curve. As already discussed in the previous sections this moment is highly affected by the magnitude of the initial cohesive

strength, the greater the value the slower this phenomenon. It represents the toughness of the matrix itself.
In this image is also possible to see the curve behavior of the degradation, which is more intense in the middle of the section and less severe at the borders. Even if the deflection induced by the hinge is the same all over the hinge the boundary effects contribute to the establishment of this curvature in the process zone region. This phenomenon is much more visible when the crack propagation as in Figure 3.22.

It is possible to see the process zone at its full development, and the curve boundary is present both at the crack front and at the detachment part. The detachment of the process zone from the crack marks the beginning of a new part of the delamination. From the beginning of the crack establishment to this moment the fracture toughness has increased due to the increase in the region's interest by the fiber bridging. The increasing part of the fracture toughness induces a plateau in the load-displacement curve. The stationarity of the load in this context can be explained by the increase of the area resisting the detachment with a parallel degradation of the matrix. However, there is a point at which the degraded area stops expanding, the new area, which is subjected to delamination, is equal to the area that reaches the end of life of the cohesive law. Once the process zone arrives at its maximum extension then there is a decrease in the load, because the arms become longer the resistance remains the same. As experimentally verified at this point, in fact, the fracture toughness arrives at a steady state condition. Figure 3.23 shows the propagation of the crack in the next steps.

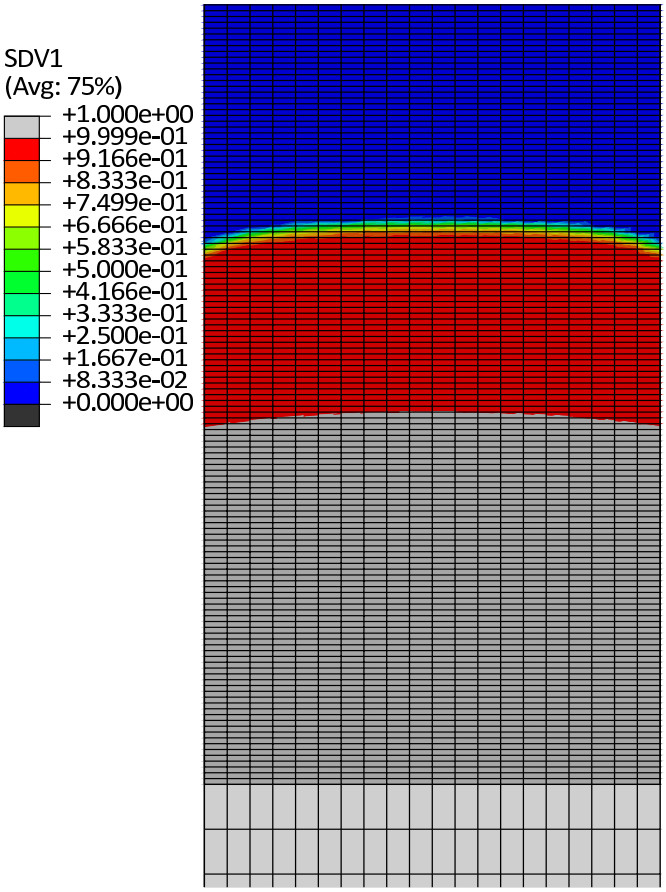

Figure 3.23: SDV1 end

The length of the process zone keeps the same shape and the crack propagates at a constant speed.

3.2.6. Mesh dimension convergence study

One of the main drawbacks of the cohesive model but in general of the finite element method is mesh dependence. Many studies underline the need of a particular mesh in order to avoid these issues as Rimoli [55], Harper [56] and Pascuzzo [57]. Rimoli proposes the progressive split of the elements to achieve an isotropic behavior of the mesh [58] and Park solved the problem with a dynamic adaptive mesh [59]. In the context of static analysis and fixed mesh, one possibility is to increase the refinement of the elements in the fracture process zone. The goodness of finite element analysis, besides the topological decisions on the model, is strictly related to the mesh size. The shape function of this method is simple polynomials that in most cases are linear or quadratic depending on the application. So in order to obtain a more accurate result, the mesh size is decreased, but *a priori* it is impossible to determine the ideal element size. For this reason, it is

common to proceed by trial and error until the mesh size does not influence anymore the model response. Five analyses have been performed to decide the correct mesh size. Five models, with progressive refined meshes have been built. The mesh has been refined until the result of the last two analyses is close enough. Once the convergence is reached it is selected the element size that grants a good accuracy with a fair computational time. In Figure 3.24 it is represented the error decrease by increasing the refinement, where the error is computed as the average difference between the considered model and the most refined one. It is possible to notice how the last two models even with a less refined mesh can be a good approximation of the finer one.

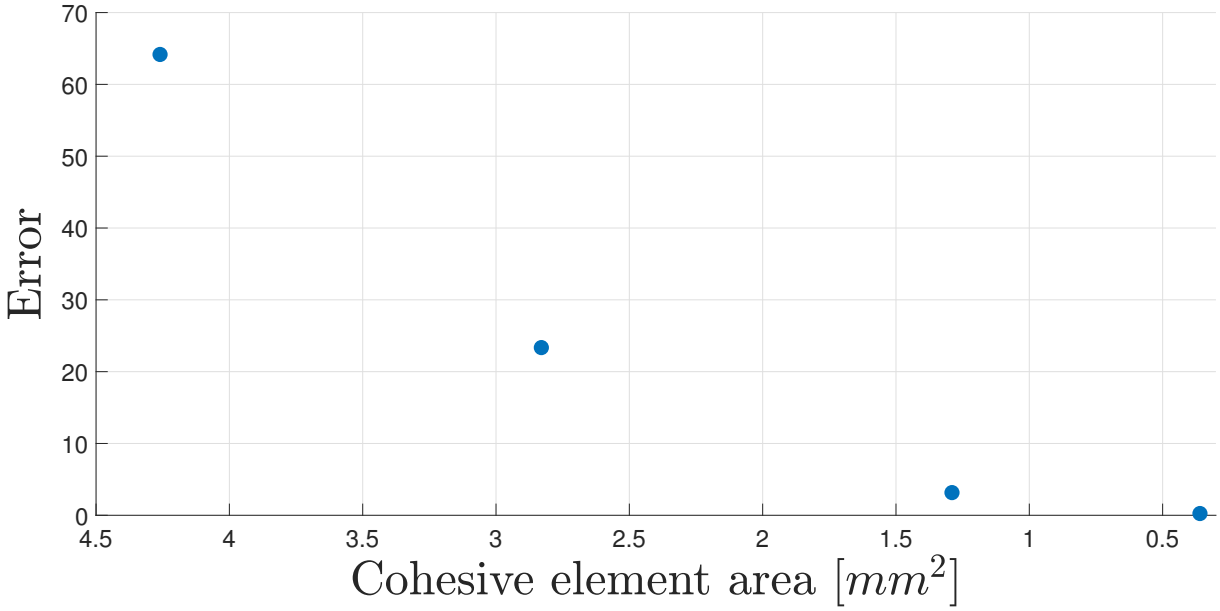

Figure 3.24: Mesh refinement error

One of the main outputs of the analysis is the load-displacement curve. In Figure 3.25 it is represented this output for the five models and they are compared with the experimental curve.

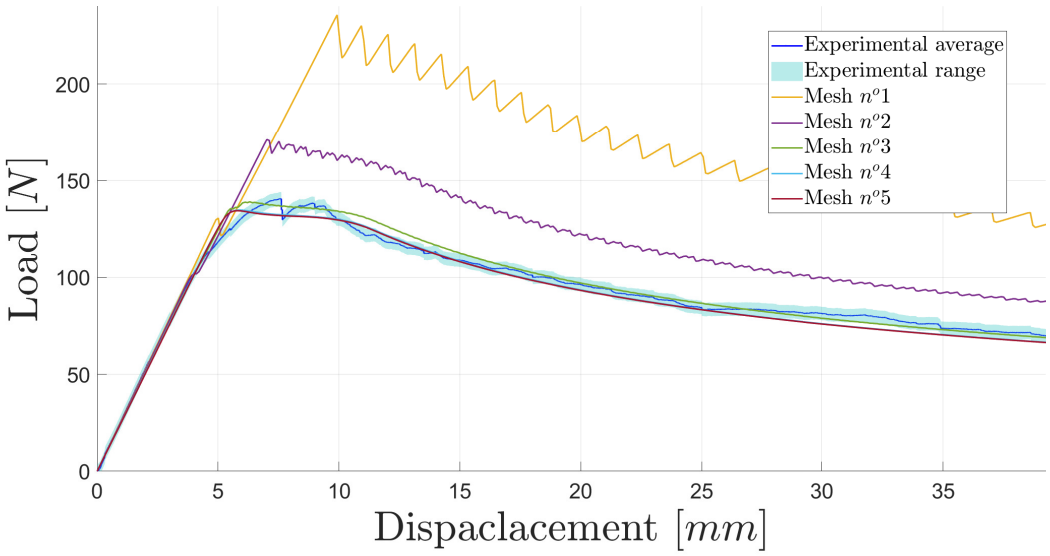

Figure 3.25: Mesh refinement Traction separation

The coarser the mesh the higher the induced numerical stiffness of the model. In fact, the less refined meshes give a higher value of the reaction force at the moving constraint. Another important feature is the aliasing in the load decrement. Due to the big dimension of the elements, when a row of elements is deleted a significant variation in the geometry and in the stress distribution is induced, the smaller the element the smaller this effect. A further interesting consideration can be deducted from the observation of the process zone. The five models process zone at the end of the opening of $40\,mm$ is reported in Figure 3.26.

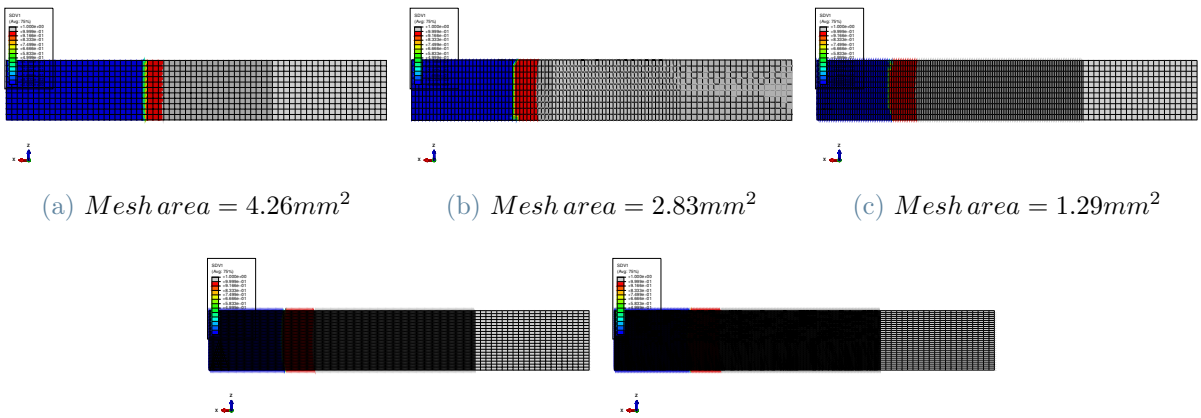

(a) $Mesh\,area = 4.26mm^2$ (b) $Mesh\,area = 2.83mm^2$ (c) $Mesh\,area = 1.29mm^2$

(d) $Mesh\,area = 0.36mm^2$ (e) $Mesh\,area = 0.21mm^2$

Figure 3.26: Process zone for different mesh size

In order to achieve a correct concave process zone, a reduced element size shall be used. Even if a finer mesh grants always a better result, the time efficiency is relevant, mainly because the already present non-linearity of the constitutive law provides a high computational cost. In order to obtain simulations of feasible duration, it is mandatory to select a mesh with the right amount of nodes that grants both accuracy and admissible computational time. In Table 3.4 the error of the five models and their respective computational times are summarized.

Mesh area $[mm^2]$	**Average Error** $[N]$	**Computational time** $[s]$
4.26	64.11	2507
2.83	23.35	6960
1.29	3.15	19500
0.36	0.24	39300
0.21		95850

Table 3.4: Mesh refinement error and computational time.

The coarser and finer meshes lie at the opposites, the former is fast but completely inaccurate while the latter requires a huge amount of time. It is selected the mesh area of $0.36\,mm^2$ due to the accuracy,the computational time and well-represented process zone.

3.3. Parameters fitting

Even if the cohesive law formulated has a strong relationship with the experimental data a further step is needed in order to obtain a better fitting between the FEM and experimental load-displacement curve. In fact, the cohesive law is based on the computation of the fracture toughness at the beginning and at the end of the experiment, however, the fracture toughness is not directly computed but extrapolated and approximated by various models. That being said the cohesive law found is just a good first approximation to be better analyzed. An optimization algorithm is used to find the correct parameters of the cohesive law that can retrieve the most similar load-displacement curve with respect to the experimental one. For the parameter fitting purpose, the FEM model is considered as a black box that given the parameters of the cohesive law returns only the load-displacement curve at the hinge of the specimen. The FEM analysis however presents a high level of non-linearity and a high computation cost, from an optimization point of view this shall be taken into account because it is needed an algorithm capable of obtaining a fair result

with a low number of function calls. Moreover, the difference function between the FEM and experimental curve has not a prescribed gradient and a local approximation of the derivative of the function would require too many function calls that would generate an infeasible computation time. For all of these reasons, a gradient-free simple algorithm has been exploited for the computation of the parameters. The Neldel-Mead method has been selected for this purpose, which is based on an algorithm with a huge heritage and high reliability without convergence issues. The parameters fitting procedure is applied both to the bi-linear and tri-linear cohesive law, in order to see how a good parameter selection can improve the efficiency of the model.

3.3.1. Nelder–Mead method

The Nelder-Mead method is an optimization method developed in the 60s by Nelder and Mead [60][61]. This method has been highly applied in many computation-related fields, such as this case for engineering optimization [62]. A stable and efficient implementation is present in the SciPy library [63]. This method is part of the direct search methods family because it only evaluates function values and their pattern and it does not require the derivative of the function. The method works for unconstrained multi-variable non-linear problems.

The objective of the method is to find the minimum of a function, this is achieved by an iteration process in which a simplex is modified gradually with the aim of diminishing the function value at the vertexes of the simplex. A simplex is the simplest spatial configuration of $n - dimensions$ that can be built with $n + 1$ vertex in a space of n dimension, for example in $2D - space$ the simplex is the triangle, and in the $3D - space$ the tetrahedron. At each iteration, a simplex, of $n - dimesion$ in which n is the variable number, is built. The algorithm is reviewed in Algorithm 3.1.

Algorithm 3.1 Nelder Mead optimization algorithm

Initial simplex construction
while $Termination\,test == False$ **do**
  Ordering simplex vertex respect to the function value
  $f_h = \max_i f_i \;\; f_s = \max_{i \neq h} f_i \;\; f_l = \min_{i \neq h} f_i$
  Compute the **centroid** on the best side
  $c \equiv \frac{1}{n} \sum_{i \neq h} x_i$
  Compute **reflection** point x_r and its function value f_r
  if $f_l \leq f_r < f_s$ **then**
    Accept x_r
  else if $f_r < f_l$ **then**
    Expand the simplex compute x_e and f_e
    if $f_e < f_r$ **then**
      Accept x_e
    else if $f_e > f_l$ **then**
      Accept x_r
    end if
  else if $f_r \geq f_s$ **then**
    Compute the **contraction** point x_c and f_c
    if $f_c \geq f_r$ **then**
      Accept x_c
    else
      Shrink the simplex
    end if
  end if
end while
Return best vertex of the final simplex

Different methodologies can be applied to terminate the optimization without spending a useless amount of computation time. In this analysis, as stop condition is used the difference between the function values of the simplex vertexes. The iteration process is quit when this difference is less than a prescribed tolerance as Equation 3.22.

$$f_h - f_l \leq tol \tag{3.22}$$

The most important part of the algorithm is the transformation of the simplex, by chang-

ing the transformation procedure different convergence behaviour can be obtained. The transformations are controlled by four parameters, that are subjected to some constrained and can be modified in order to achieve a different response of the algorithm. At each step, it is performed a reflection as reported in Figure 3.27. The reflection point is obtained as Equation 3.23.

$$x_r \equiv c + \alpha(c - x_h) \tag{3.23}$$

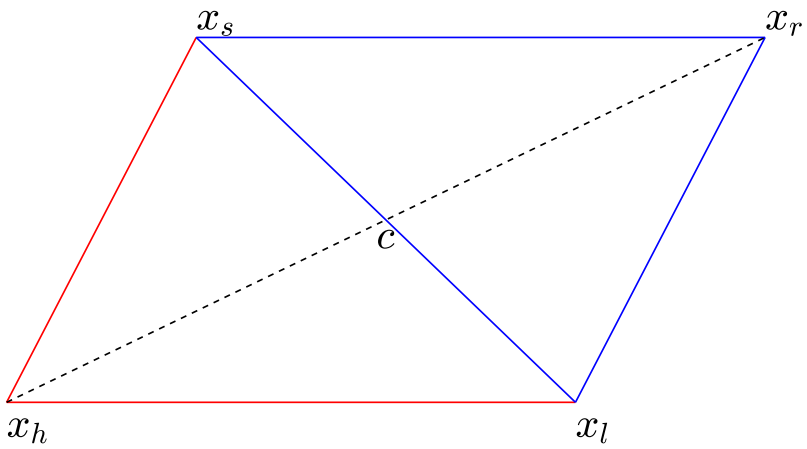

Figure 3.27: Neldel-Mead reflection.

The reflection is controlled by the α parameter, in this case it is considered $\alpha = 1$.

To decide if the direction used is favorable it is performed an expansion thanks to Equation 3.24 and Figure 3.28, the expansion is controlled by the γ parameter, which shall be greater than one to increase the dimension of the simplex, increasing its magnitude can imply a faster convergence but also the default discard of the expanded simplex. In this case it is applied a parameter $\gamma = 2$.

$$x_e \equiv c + \gamma(x_r - c) \tag{3.24}$$

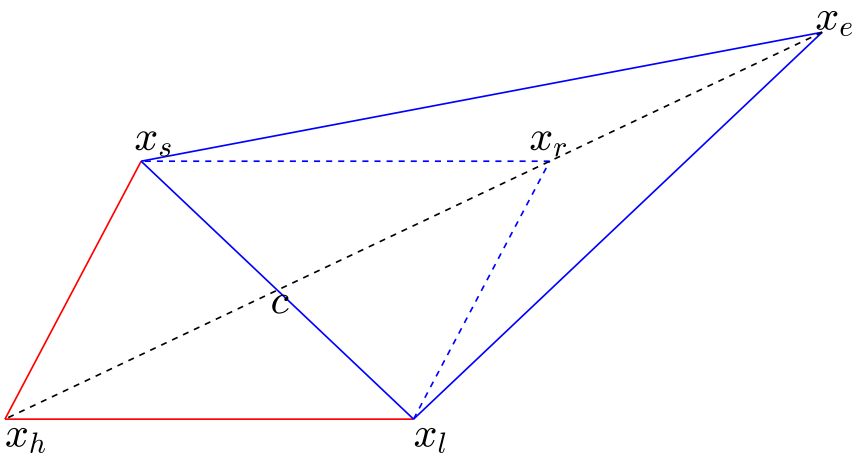

Figure 3.28: Neldel-Mead expansion.

If the direction pursued leads to an increment of the function value a contraction of the simplex is tried to investigate better the region in which the simplex lies. The contraction point is obtained through Equation 3.25 and it is governed by the parameter β, which shall be included in the zero to one range, in this case, $\gamma = \frac{1}{2}$. This transformation is represented in Figure 3.29.

$$x_c \equiv c + \beta(x_r - c) \tag{3.25}$$

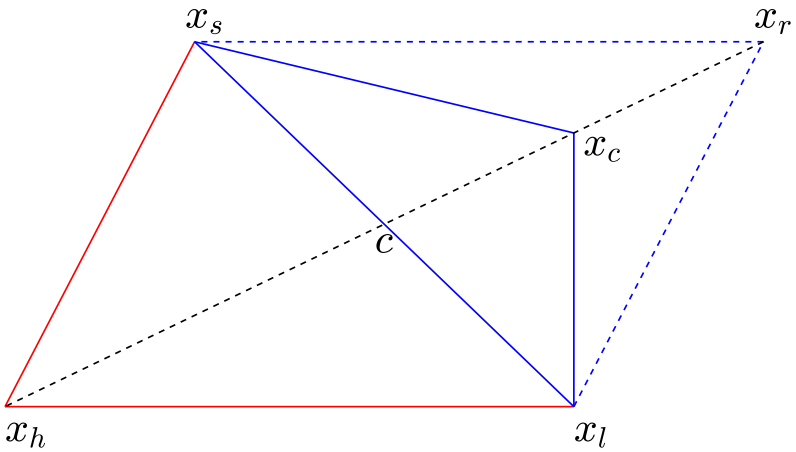

Figure 3.29: Neldel-Mead contraction.

In the case of collapsing simplex after the contraction, further investigation of the method has led to the implementation of the shrinkage that built a smaller simplex with two new

vertexes as reported in Figure 3.30. The new vertexes are found in Equation 3.26, with parameter $\delta = \frac{1}{2}$.

$$x_i \equiv x_l + \delta(x_i - x_l)\, with\, i \neq l \tag{3.26}$$

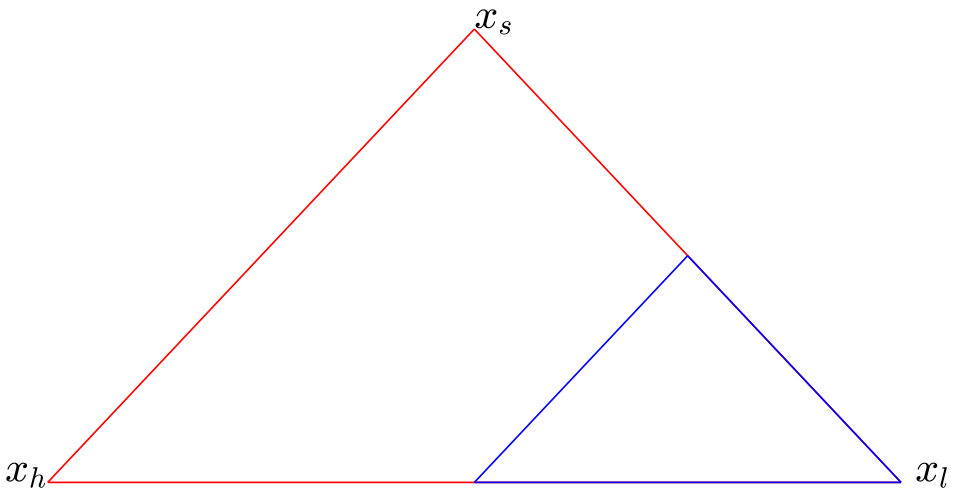

Figure 3.30: Neldel-Mead shrink.

The major drawback is that the method is heuristic, so it does not guarantee the retrieve of a global optimum, in fact, the search can stagnate to a local minimum without arriving at the desired solution. Although there is the possibility of obtaining a result that is far away from the solution, due to the nature of the problem the method is used in any case in particular for its simplicity and for its high convergence rate.

3.3.2. Error defintion

The first step and one of the most crucial parts of the parameter fitting is the parameter of merit definition. The optimization algorithm is a blind solver that can only find the best parameter that expresses the minimum of a determined function. The study case aims to find the parameters that allow the best fitting between the numerical and experimental curve, the fitting problem is then translated into an error minimization problem. The optimization algorithm shall be used to minimize the error between the two different curves. Depending on the definition of the error different behaviors can be obtained. For example by exploiting a local error, such as the maximum difference between the two curves Equation 3.27, the proximity of the two curves is taken into consideration but not the behavior.

$$err = \max_i Load_{FEM}(\delta_i) - Load_{exp}(\delta_i) \tag{3.27}$$

In this study, however, the most interest is reserved to understand if the proposed cohesive law can return a good approximation of the phenomena observed. The magnitude of the distance is not considered of great interest for this analysis, it is then defined a global error that considers all the intervals and aims to find an error that captures the difference between the two behaviors. The error function is defined in Equation 3.28.

$$err = \frac{\sqrt{\sum_{i=1}^{N} \Big(Load_{FEM}(\delta_i) - Load_{exp}(\delta_i) \Big)^2 \Big(\delta_i - \delta_{i-1} \Big)}}{\sqrt{\sum_{i=1}^{N} \Big(\delta_i - \delta_{i-1} \Big)}} \tag{3.28}$$

The error definition presented above it is only valid for the comparison of one FEM and one experimental curve, however, as previously mentioned different tests have led to slightly different results. Since the attention of the analysis is reserved to the material and not on the single laminate, the fitting shall consider different experimental curves to be a better representation of the material. For this reason, it is defined an average error that comprehends different tests. The new formula is reported in Equation 3.29.

$$err_{avg} = \frac{\sum_{i=1}^{N} err_i}{N} \tag{3.29}$$

A single curve fitting would lead to a better result, however, the general comprehension of the material is considered of primary importance.

3.3.3. Bi-linear curve fitting

The first optimization has been performed on the bi-linear cohesive law. In this case the error minimization has been conducted on two parameters of the law while the others have been considered fixed. As reported in Figure 3.31 the inputs of the optimization are the maximum strength, σ_0 and the fracture toughness,G that is the area underneath the curve.

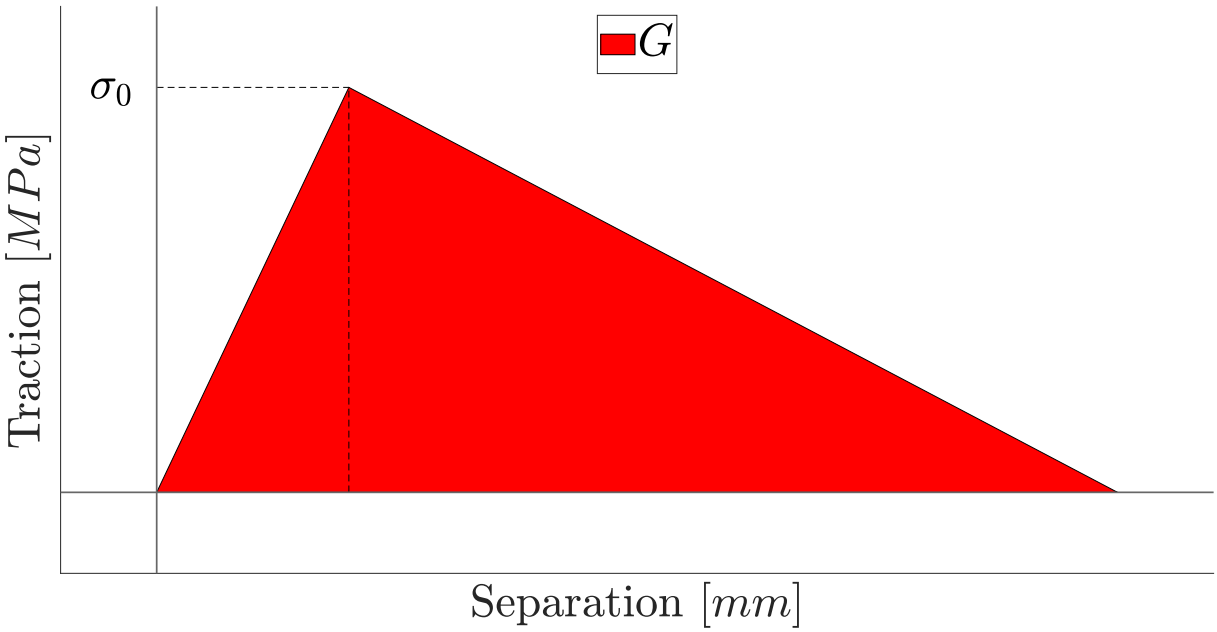

Figure 3.31: Bi-linear cohesive parameters

The penalty stiffness is the only term that remains fixed throughout the fitting, in fact, it is only a numerical artifact. Its change could eventually obtain a better result but would invalidate the goodness of the analysis, removing it from the variables of the problem allow a better understanding of the optimization and the characteristics of the material. The output of the process is reported in Figure 3.32, in which the cohesive law before and after the parameter fitting are compared. While in Table 3.5 the parameters obtained are reported.

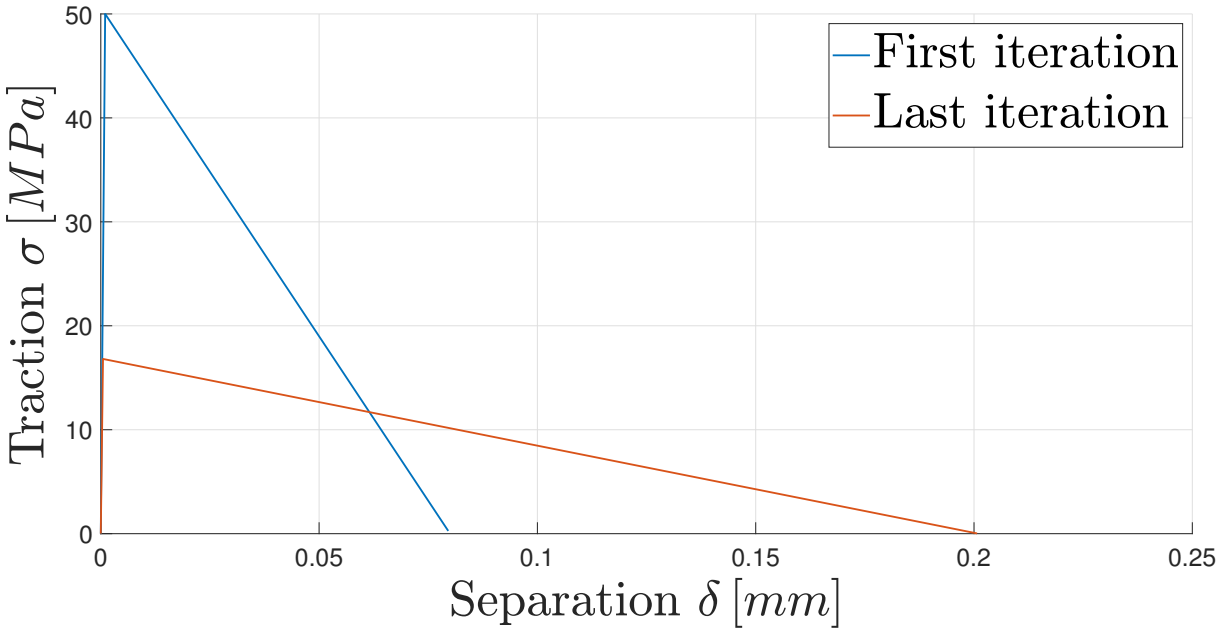

Figure 3.32: Bi-linear constitutive law optimization.

	Maximum strength $\sigma_0\,[MPa]$	**Fracture toughness** $G\,[kJ/m^2]$
Initial	50	2.0
Final	17.34	1.69

Table 3.5: Bi-linear cohesive optimization parameters.

The initial maximum strength selected does not have a physical meaning in this case but it is a common value found in literature [64] [65] [66]. Even if the parameter indicates the strength at which the interface matrix starts to degrade, it is not easy to retrieve it from experimental measures so it is often found through a trial and error procedure.
As it is possible to see from Figure 3.32 the new cohesive law presents a lower degradation rate with respect to the initial one and a higher rupture separation δ_f. The maximum elongation witnessed by the element is almost four times higher with respect to the initial one. This is caused by both the parameters, the maximum strength is lowered and the fracture toughness is increased. The algorithm has converged to a σ_0 that is not compliant with previous studies on similar composites, this topic will be better analyzed at the end of the section. The fracture toughness found instead has a value that lies in the middle between the maximum and minimum fracture toughness experimentally recorded, so it is considered a valuable result. A better understanding of the optimization procedure can be gained looking at Figure 3.33.

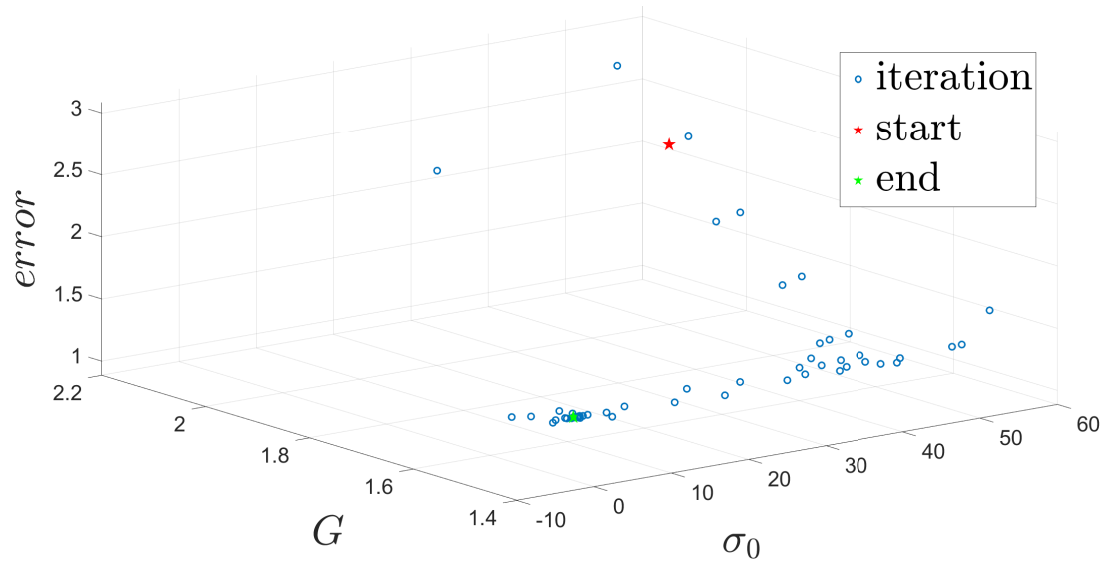

Figure 3.33: Bi-linear error minimization.

The image shows the various function calls performed by the algorithm during the iterations and their relative error. From the starting point, the algorithm builds its first simplex and finds a steep descent decreasing the G parameter. After a fast error decrease in the first iteration due to the change in the fracture toughness, the method starts a long series of iterations mainly changing the σ_0 parameter. The second phase does not provide a significant decrease in the error but it finds in any case a minimum of the function. The final error is reported in Table 3.6.

Initial error	2.333
Final error	0.89

Table 3.6: Bi-linear cohesive optimization parameters error.

The physical understanding of the parameters obtained is expressed in Figure 3.34. The final result displayed is acceptable, even with a bi-linear cohesive model it is possible to reach a good approximation level. The reduction of the fracture toughness has lowered the waning side of the curve. The G parameter in fact in this configuration controls, in particular, the degradation of the interface, and how much after the beginning of the damage the element fails completely. One of the biggest disadvantages of the bi-linear cohesive model is the peak formation and the end of the linear part, this model is not capable of describing the part in which the degradation zone propagates without breaking

with the pre-crack. To avoid this overshoot, the algorithm has found the loophole of decreasing the maximum strength σ_0. This trick returns in slightly better error, due to a lower peak at the end of the linear part, but compromises the linear growth of the load. As already mentioned the linear part of the curve is only a function of the dimension of the pre-crack, the thickness of the beams, and the strength along the fibers, and not the strength of the interface. The result found is a numerical trick used by the algorithm found to fill in the gaps in the model. A huge decrease in the maximum strength inserts a numerical weak region in the interface, that eclipses the linear nature of the first part. The main lesson given by these results, in particular looking at Figure 3.32, is that a longer separation is required by the elements to have a load-displacement curve that is closer to the original one, so also this analysis underlines the importance of developing a cohesive law with an extended degradation region as tri-linear one.

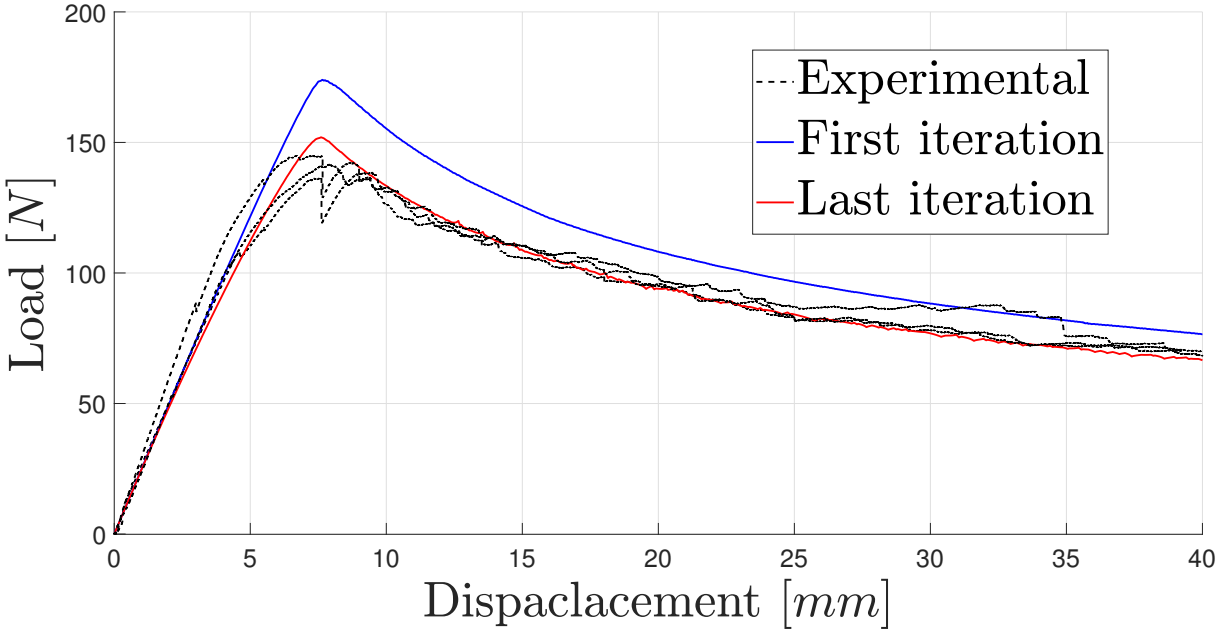

Figure 3.34: Bi-linear load-displacement curve.

3.3.4. Tri-linear curve fitting

The tri-linear cohesive model is governed by more parameters concerning the bi-linear one. The adaptive nature of the model implies the need for a greater number of variables. Excluding the numerical parameters, such as the penalty stiffness, four variables are required to define this law. In this analysis, however, two of them are frozen, to avoid the effects encountered in the previous section. In the previous analysis, the variability of the maximum strength has led to a numerical weakness in the model that has compromised the linear nature of the first part of the deformation. Even if the parameters regarding the

maximum strength, of both the two super-imposed bi-linear laws, are considered known *a priori*. This choice wants to avoid numerical tricks lacking a physical meaning. It could be argued that it is possible to achieve meaningful variables if constrained correctly, however, the range bounds are not clear and this should be the focus of further analysis. In the previous sections, the tri-linear cohesive law has been explained as a superposition of two bi-linear cohesive laws. The variables decided for the parameter fitting are the areas underneath the two cohesive laws, so the fracture toughness at the beginning and at the steady state as reported in Figure 3.35. The fixed parameters of the law are reported in Table 3.7.

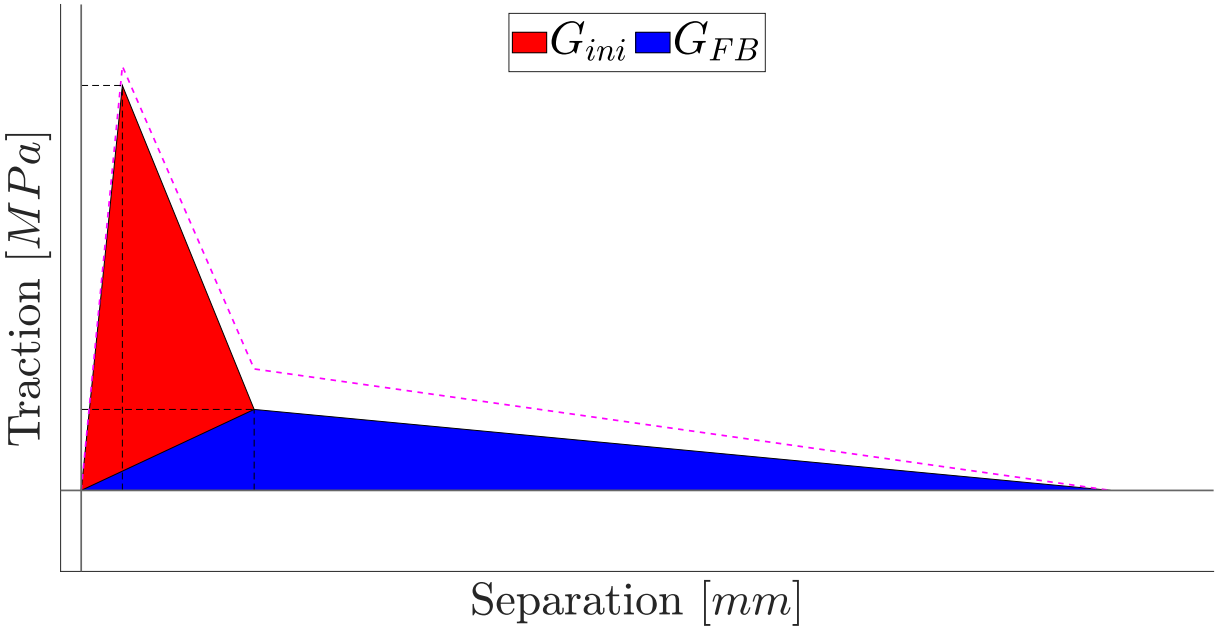

Figure 3.35: Tri-linear constitutive law parameters.

$\sigma_0\,[MPa]$	$\sigma_{FB}\,[MPa]$
50	0.7

Table 3.7: Tri-linear cohesive optimization parameters.

The parameters decided do not influence the linear part of the load-displacement curve and they are related to two different behavior of the curve itself. The initial fracture toughness influences the first degradation region it is responsible for the higher damage increase, while the second is for the residual stresses present in the fiber bridging phenomena.
The change of the cohesive law is reported in Figure 3.36, while the final parameters obtained in Table 3.8.

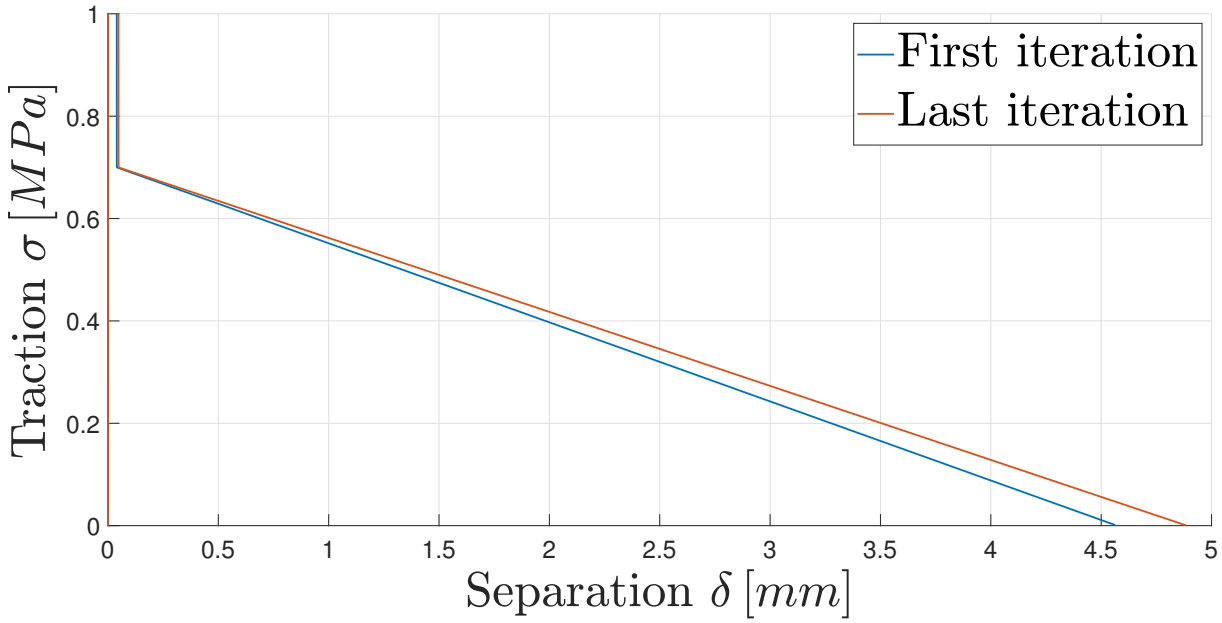

Figure 3.36: Tri-linear constitutive law optimization.

	Initial G $G_{ini}\,[kJ/m^2]$	**Steady state G** $G_{SS}\,[kJ/m^2]$
Initial	1.0	1.6
Final	1.24	1.70

Table 3.8: Tri-linear cohesive optimization parameters.

The figure represents only a zoomed part of the entire cohesive law, for clearness reasons it has been given more relevance to the bridging part. The second part is more subjected to a change of parameters. Also in this case it is possible to see an adjustment in the maximum separation of a single element and the degradation slope. Differently from the previous case, the change of the parameters is less significant, this is caused by the fact that the law has an intrinsic relationship with the experimental phenomena observed, so the adjustment of the parameter is a fine calibration and not a fictitious numerical revolution. Even if the algorithm has found the G_{FB} Table 3.8 reports the initial and steady-state fracture toughness. This decision is more relevant concerning the material point of view because experimentally it is observed only an increment in $R-curve$ and the fiber-bridging fracture toughness is an eternal explanation that cannot be measured. The Nelder-Mead iterations conducted to obtain the final result are reported in Figure 3.37.

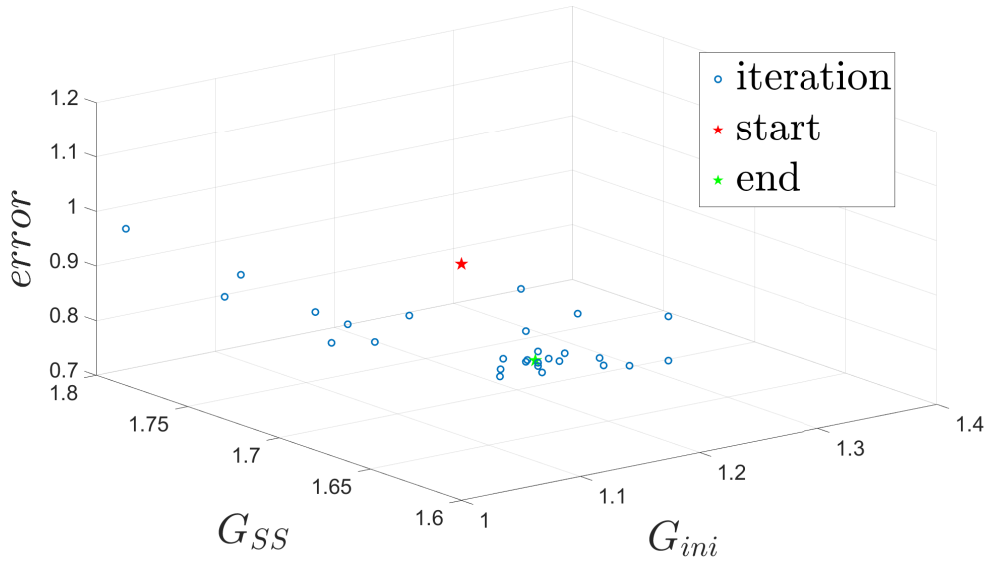

Figure 3.37: Tri-linear error minimization.

As in the previous study, the algorithm finds a path in which the error reduction is steeper and it follows it until the reduction ends, then the second parameter optimization follows. Firstly it is modified the fiber-bringing toughness because it allows a faster error decrement, this is related to the error definition. Indeed while the initial toughness works with the plateau after the linear part, the fiber one works in a higher region, and small changes in the parameter give the origin of higher error modification. The error contraction is reported in Table 3.9.

Initial error	1.13
Final error	0.71

Table 3.9: Tri-linear cohesive optimization parameters error.

As anticipated the error reduction is less significant with respect to the previous case, on the tri-linear parameters fitting it has only reached a reduction of 37% against a reduction of 61% of the previous one. Although the best performances of the optimization algorithm in the bi-linear case, and the numerical tricks adopted, the tri-linear model confirms its superiority. The optimized error with the tri-linear model is 20% less with respect to the bi-linear one.

The final load-displacement curve obtained is reported in Figure 3.38, where the fitting performances are clearly visible. It is possible to notice how the two increments in the

parameters have led to an enlargement of the load witnessed by the FEM model. The change in the initial fracture toughness has elongated the linear part of the curve, this elongation loses the behavior of two of the three experimental curves in the linear part, however, this allows a higher plateau. The elevation of the plateau implies a reduction of the error in a very sensitive part, in this region, many defects emerge and it is very difficult to predict a correct behavior.

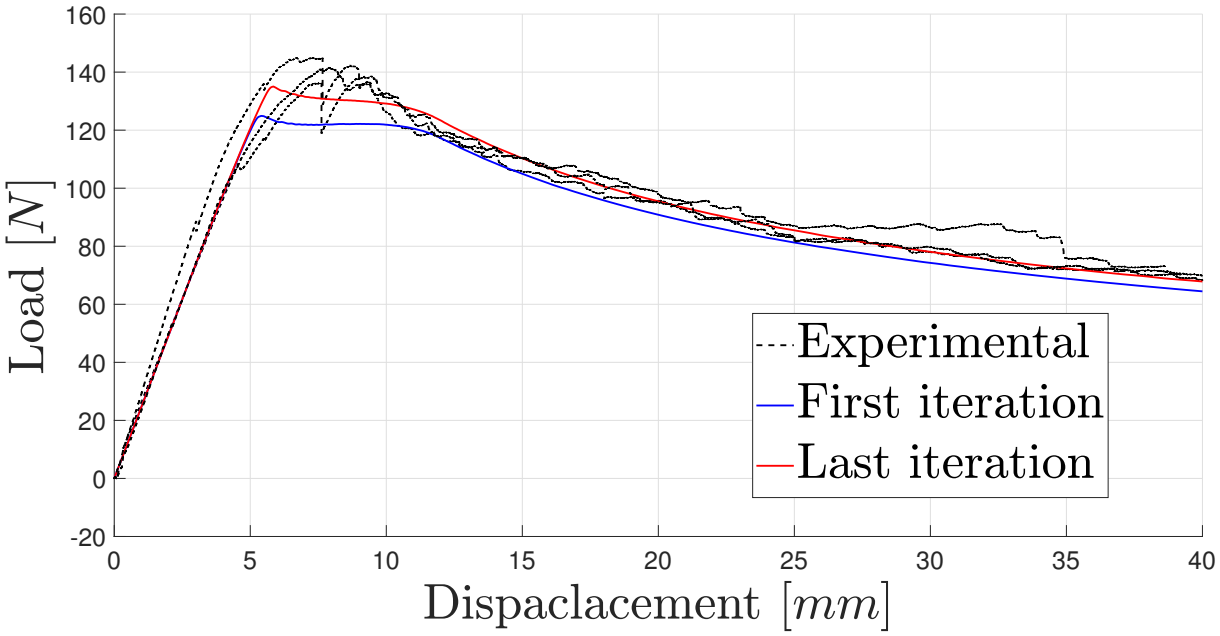

Figure 3.38: Tri-linear load-displacement curve.

4 | Fatigue Analysis

4.1. Fatigue model

Delamination in the presence of cyclic stress is a complex problem. It can cause the strength and stiffness of laminated composites to deteriorate and potentially cause them to fail. On the other side, delamination absorbs strain energy, which can be helpful in some cases, such as impact performance, and influences their failure processes. Over the last several decades, extensive research has been conducted to comprehend the fatigue delamination process and methods for controlling it in composites to assure the dependability of composite structures and extend their service life. This chapter provides an overview of prior work on the experimental characterization and numerical simulation of fatigue delamination, emphasizing unidirectional laminated composites with 0/0lay-up. The beginning of delamination in composite materials relies on the expansion of an existing fracture. Typically, a fixed maximum load/displacement is provided to the specimen in the fatigue onset test, and loading cycles are performed with a constant R-ratio, which refers to the ratio of maximum and minimum applied load/displacement until some signs of crack propagation are discovered. Its output is presented as a G-N curve, akin to the S-N curve for metallic materials, describing the connection between the driving power, G, and the number of cycles, N. It is possible to develop the G-N curve, where G_{max} is the maximum SERR delivered to the crack tip and N_{onset} is the number of loading cycles prior to the commencement of the delamination as Equation 4.1.

$$G_{max} = \hat{f}(N_{onset}) \tag{4.1}$$

The fatigue delamination spread test is used to determine how the delamination expands after the onset with increased loading cycles. In accordance with the Paris' law for metals, a linear log-log plot of the delamination growth rate da/dN vs the provided SERR G, such as the maximum SERR Gmax, is used to describe composite materials. Equation 4.2 is the mathematical formulation of Paris' law.

$$\frac{\mathrm{d}a}{\mathrm{d}N} = C(G_{max})^m \tag{4.2}$$

4.2. Experimetal results

In order to characterize the material in the fatigue environment a mode I fatigue test is carried out. The procedure uses a specimen that is equivalent to the one presented in the first chapter and the machine test configuration is the same, however, it combines a static part and a cyclic one. In the former the specimen is opened to obtain a determined aperture, that is small enough to appreciate the further fatigue part, but not big enough to obtain a development of the crack process zone. In the latter, the specimen is subject to a cyclic aperture with a ratio between the bigger and smaller aperture equal to R. The configuration data are reported in Table 4.1.

Aperture $[mm]$	$R\,[-]$
3.2	0.1

Table 4.1: Experimental fatigue configuration.

From the experiment load, crack propagation and aperture are retrieved with respect to the number of cycles. From this information, it is possible to compute the speed of propagation of the crack and the fracture toughness, with the $modified\,beam\,theory$. Once both are retrieved they can be combined together to shape the relation between the two parameters of merit. However this combination appears as a scatter of points, then to obtain the classic formulation of the Paris law Equation 4.2, a parameter fitting is performed. The result of the fitting is reported in Table 4.2.

$C\,[m^3/kJ]$	$m\,[-]$
0.0229	2.8438

Table 4.2: Paris law fitted parameters.

The experimental and fitted result is then represented in Figure 4.1, where it is possible to notice a common behavior of the material in the condition presented.

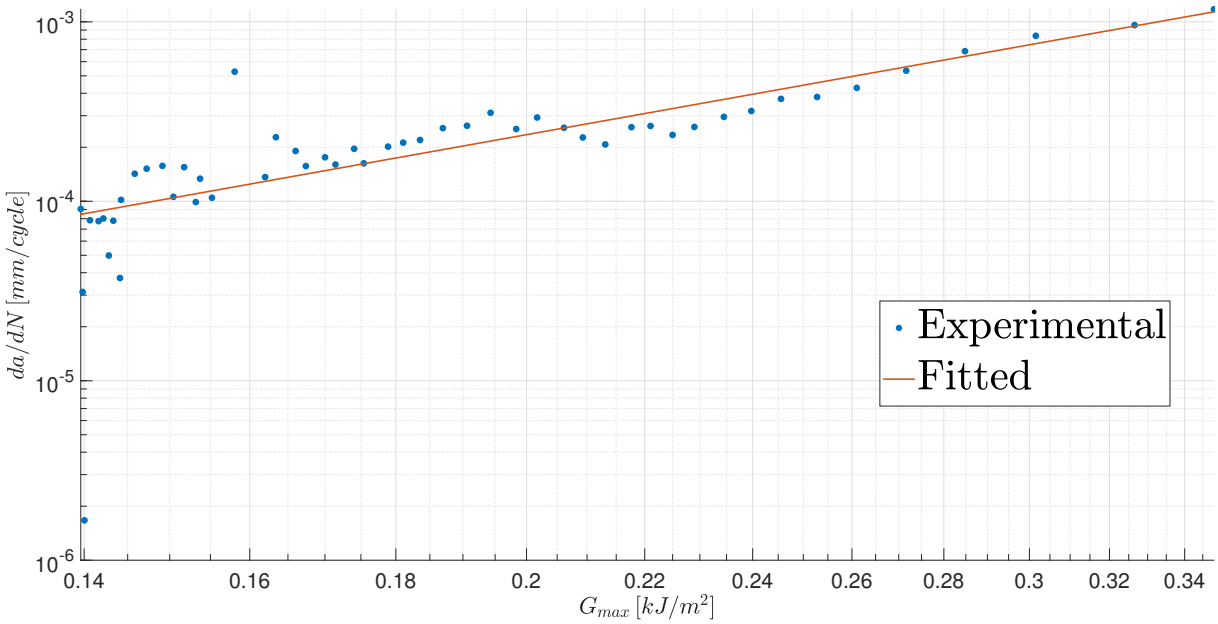

Figure 4.1: Experimental fatigue law fitting

4.3. Fatigue in Cohesive Zone Modelling

A cohesive zone model of delamination's static constitutive law, which is based on the initial stiffness K_0, peak traction t_0, and fracture toughness G_c, serves as the foundation for all fatigue degradation strategies. As previously mentioned, static constitutive law can take many different forms. With regard to static behavior, a cohesive zone forms before the fracture point. It relies on the opening displacement in the cohesive zone and the ultimate displacement δ_f at which the components break under fatigue loading, both of which are initially unknown, therefore the length l_{cz} of this zone will differ from that for the static case. All of the models covered in the preceding chapter employ a two-step simulation process: the components are initially subjected to a quasi-static load while adhering to the static traction-displacement response. Following the discovery of this static equilibrium, blocks of loading cycles are applied, which, ideally, cause deterioration and eventual failure of the interface parts within the specified number of cycles outlined by the Paris legislation. This triggers a brand-new constitutive reaction. The fatigue model and load level dictate the form. The applied energy release rate G_a must be equal to the integral under the constitutive response in the steady state.

4.3.1. Review of fatigue cohesive models

Table 4.3 lists the five most often used fatigue damage models in the literature. The fatigue damage rate, $\frac{\mathrm{d}D_f}{\mathrm{d}N}$, is proportional to the fracture crack development rate, $\frac{\mathrm{d}a}{\mathrm{d}N}$, in all models. Fatigue cohesive zone length, l_f. Paris' law, static damage, and element size all influence fatigue damage rate. The static damage variable is replaced by the overall amount of static damage, D_s, in Kiefer's fatigue damage model. Equation 4.3 may be used to calculate the fatigue cohesive zone length, which is dependent on the static cohesive zone length l_s, static fracture toughness G_c, and maximum applied strain energy released rate during the cyclic loading.

$$l_f = \frac{G_{max}}{G_C} l_S \tag{4.3}$$

The cited models have different strategies for the computation of the static cohesive length.

Model	Cohesive law
Kiefer	$\frac{\delta d_f}{\delta N} = \frac{1 - d_{\mathrm{s.t}}}{l_f} \frac{da}{dN}$ [67]
Turon	$\frac{\delta d_f}{\delta N} = \frac{\left(\delta_1^f (1 - d_s) + d_s \delta_1^0\right)^2}{\delta_1^f \delta_1^0 l_f} \frac{da}{dN}$ [68]
Perov	$\frac{\delta d_f}{\delta N} = \frac{\delta_1^f \delta_1^0}{\delta_1^2 l_f} \frac{da}{dN}$ [69]
Pirondi-Moroni	$\frac{\delta d_f}{\delta N} = \frac{1}{l_f} \frac{da}{dN}$ [70]

Table 4.3: Fatigue cohesive models

4.3.2. Kawawhita-Harper model

The selected method for modeling the material's fatigue behavior is the one developed by Kawawhita and Harper [71] [72]. The authors both implemented a local model and a non-local one, due to the nature of the user-defined cohesive law it is selected for this study the former. In fact, the user-defined constitutive law is exploited by the FEM solver at each integration point at the same time, so in order to preserve this methodology the local cohesive law is exploited. As in the previous methods listed the fatigue implementation is obtained by adding a fatigue degradation at the cohesive level as in Equation 4.4.

$$D_{tot} = D_s + D_f \tag{4.4}$$

The variation of fatigue degradation depending on the number of cycles is expressed by the model in Equation 4.5.

$$\frac{\mathrm{d}D_f}{\mathrm{d}N} = \frac{1 - D_s}{l_e}\frac{\mathrm{d}a}{\mathrm{d}N} \tag{4.5}$$

Where D_s is the static degradation and l_e is the element length in the crack propagation direction. The increment in fatigue degradation after a certain amount of cycles is obtained by integrating the variation on the interval of cycles Equation 4.6.

$$D_f(N + \Delta N) = D_f(N) + \int_N^{N+\Delta N} \frac{\delta D_f}{\delta N}\mathrm{d}N \tag{4.6}$$

Considering the cycle jump is small it is possible to rearrange the previous expression as Equation 4.7.

$$D_f(N + \Delta N) \approx D_f(N) + \frac{\delta D_f}{\delta N}\mathrm{d}N = D_f(N) + \frac{\mathrm{d}D_f}{\mathrm{d}N}\Delta N \tag{4.7}$$

In some implementations, the FEM integration is performed with a fixed pseudo time incrementation, in this way the previous formulation is enough to conclude the algorithm. However in order to avoid a tedious calibration of the time step, in this study the time step is free to change and the previous formula is rearranged to take into consideration different cycle jumps. It is added a fictitious cycle frequency f to compute the number of cycles performed in the integration step.

$$D_f(N + \Delta N) \approx D_f(N) + \frac{\mathrm{d}D_f}{\mathrm{d}N} f \Delta time \tag{4.8}$$

Both the static and the fatigue degradation contribute to the crack growth, the situation of the elements at the crack front is represented in Figure 4.2.

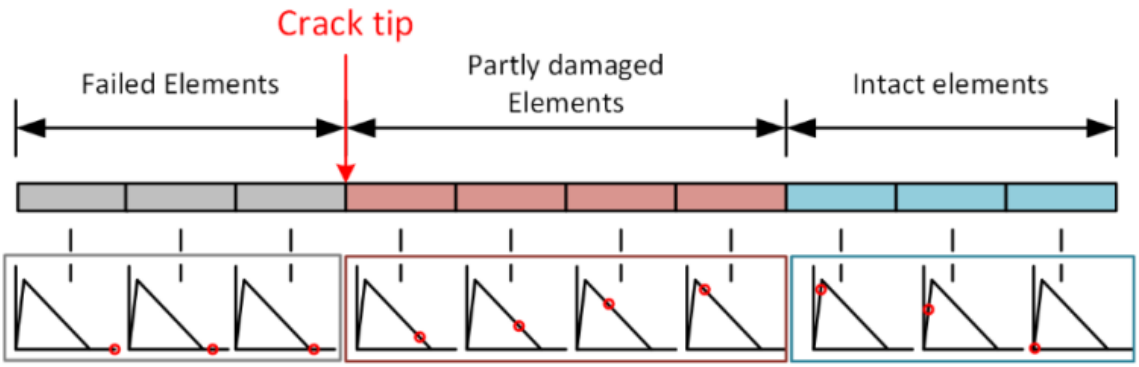

Figure 4.2: Progressive damage status.

The fatigue degradation gets harsher as the element is more deformed in fact Equation 4.5 depends on the Paris law which is a function of the area under the traction separation law.

$$\frac{\mathrm{d}D_f}{\mathrm{d}N} = \tilde{f}\left(G_{max}\right) \approx \tilde{f}\left(\sum_{i=1}^{N} \frac{\left(t_i + t_{i-1}\right)\left(\delta_i - \delta_{i-1}\right)}{2}\right) \tag{4.9}$$

The area under the TSL is computed numerically at each iteration. The model described has been initially formulated for bi-linear cohesive law, however, in this context is then developed in the already studied tri-linear model.

4.3.3. Tri-linear extension model

Teimouri [73] proposed an evolution of the Harper model in the tri-linear cohesive law context. This progress is considered an advantage because it develops the fatigue model starting from the static one, and it is more suitable for materials that experience fiber-bridging even if this phenomenon influences less the fatigue response. This model is just an extension of Harper's model with two different degradation laws as Equation 4.10.

$$\frac{\mathrm{d}D_f}{\mathrm{d}N} = \begin{cases} \dfrac{1 - D_{s1}}{l_e}\dfrac{\mathrm{d}a}{\mathrm{d}N} & if\ \delta_0 \leq \delta < \delta_{f1} \\ \dfrac{1 - D_{s2}}{l_e}\dfrac{\mathrm{d}a}{\mathrm{d}N} & if\ \delta_{f1} \leq \delta < \delta_f \end{cases} \tag{4.10}$$

Where the parameters are the same as the previous one.
In this thesis, it is applied the same methodology is changed to the static cohesive law that lies upon the fatigue one. In fact, Teimouri uses the Davila [45] and Heidari [46] model, in this case, instead, it will be used the Gong one [49].

The algorithm of the new law is expressed in Figure 4.4, where it is possible to see how the fatigue implementation is just an extension of the static one.
Figure 4.3 represents the cohesive law of a single element subjected to a pre-aperture and then a fatigue step. During the static part it proceeds as in the previous analysis however, once the fatigue starts, at a constant aperture, the element starts degrading without further aperture. The solver algorithm in the fatigue analysis is reported in Figure 4.4.

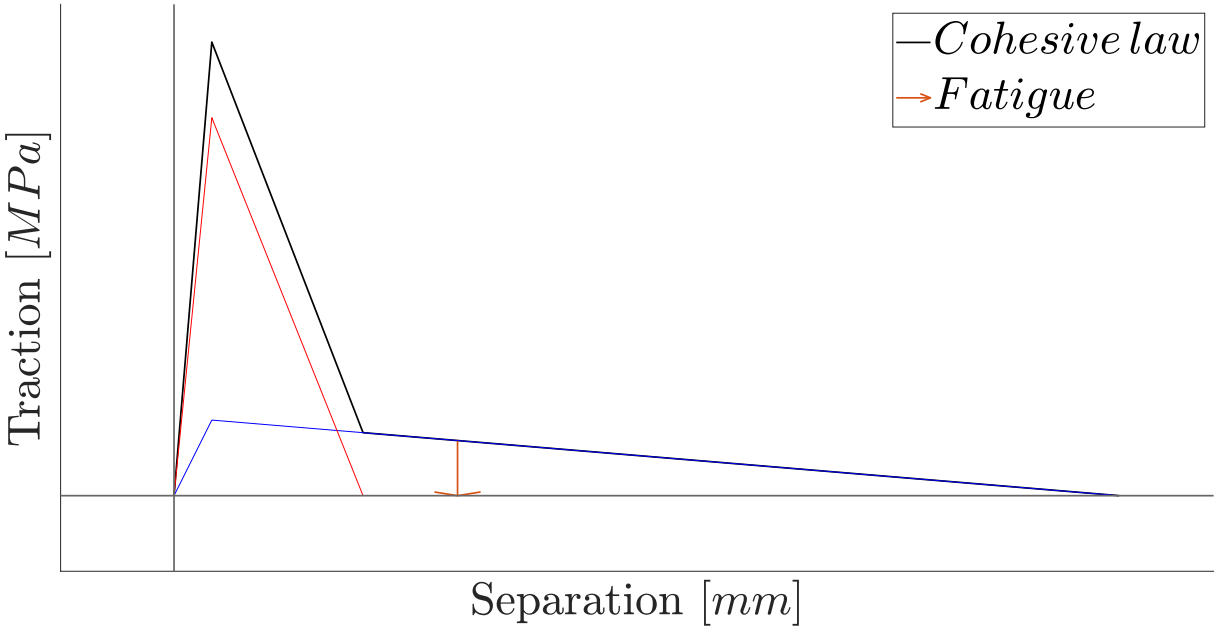

Figure 4.3: Fatigue tri-linear cohesive law

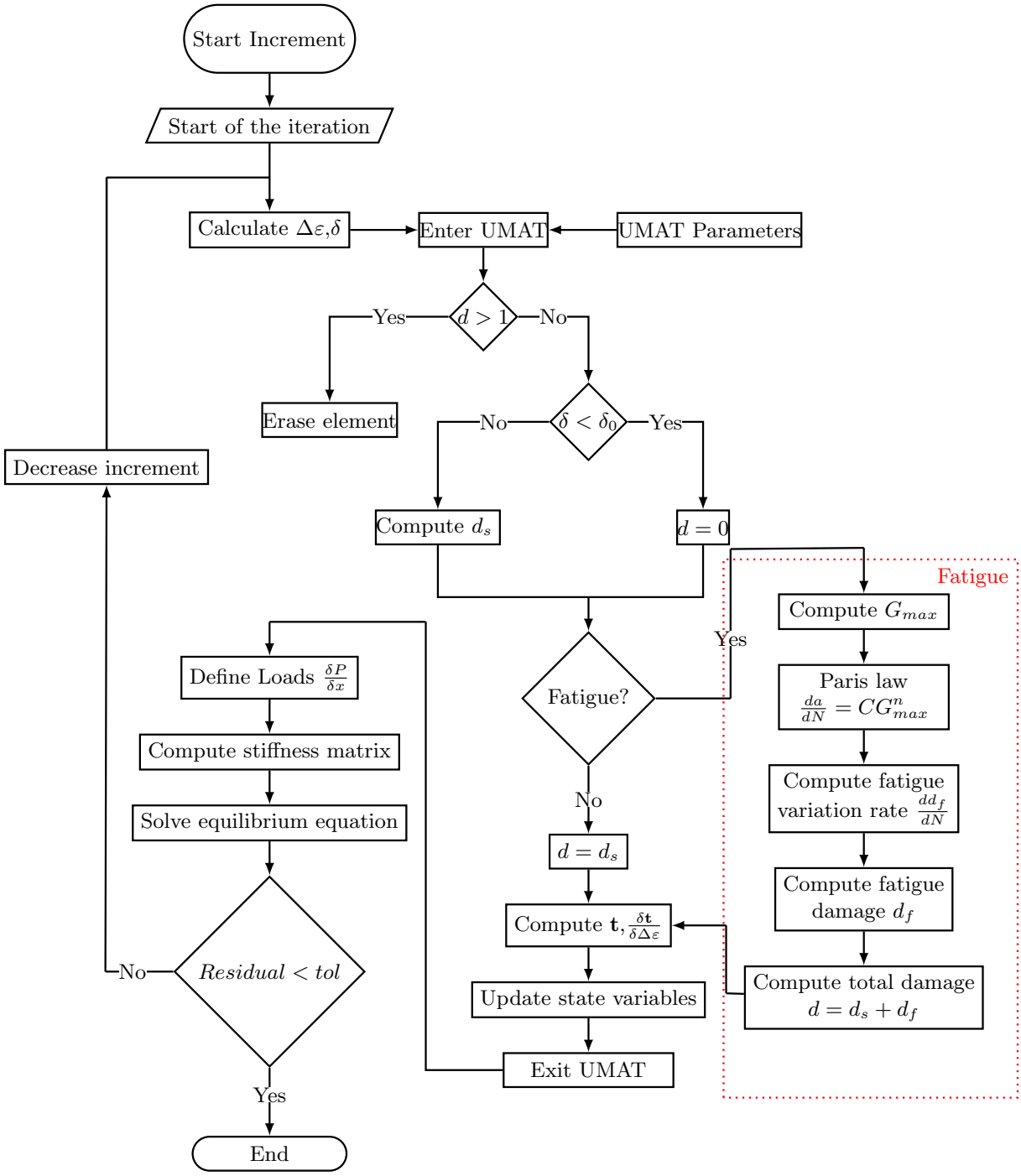

Figure 4.4: Fatigue UMAT implementation.

4.4. Fatigue case analysis

The major distinction in fatigue tests is determined by the type of cyclic load applied. The two possible tests are load-driven and displacement-driven. In the former, the tensile-test machine, controlling the load applied to the specimen, cycles the load with a varying aperture while the latter does the opposite.

In both cases, the fatigue phase is anticipated by a quasi-static one which it is reached the maximum aperture/load that the specimen will withstand during the next step. After the maximum load is obtained then the cyclic phase starts having the maximum load as the one registered at the end of the quasi-static, $Load_{max}$ and as a minimum a load equivalent to $Load_{min} = R\,Load_{max}$, where R is defined as the $R - ratio$.

There is no unique methodology to approach the numerical analysis of fatigue. What is certain in this case is the presence of a strong non-linearity caused by the cohesive law, the choice made has been dictated principally by this characteristic and the need for a reasonable computation time. Fatigue can be studied with dynamic analysis in both linear and non-linear environments, both with implicit and explicit solvers depending on the frequency of the numerical cycles. In this thesis, it is used a non-linear solver in a quasi-static environment, in which the aperture-closure is not reproduced. In fact, the displacement/load is considered fixed during the fatigue step, and degradation is only simulated by the cohesive law depending on pseudo time. So instead of replicating the cyclic behavior of the test, it used only the envelope of the load such as Figure 4.5.

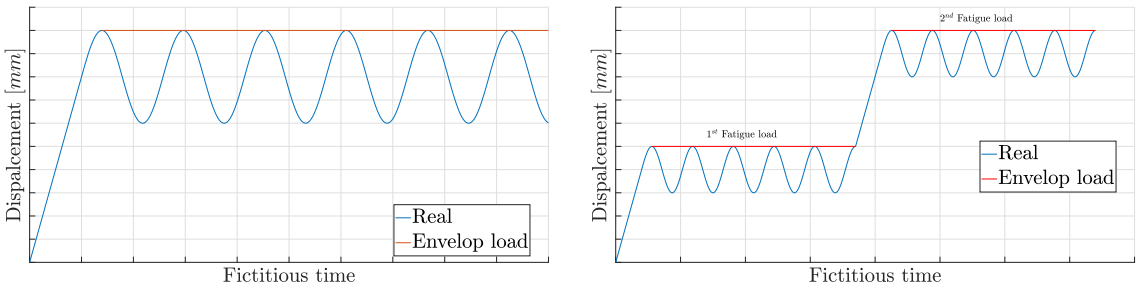

Figure 4.5: Displacement control cases.

As presented in the previous image the fatigue analysis can be split into multiple steps. The multiple aperture/load analysis returns a result more compliant with real applications. In aeronautical applications, in fact, fatigue is always present during the life cycle, however sudden variations in the loads happen, for example, due to out-of-design conditions. The characterization of the material does not change with multiple steps, but it results in a more realistic outcome.

4.5. Numerical Results

In section 4.2 the results of the mode I fatigue test have been presented, with the related fitting of the Paris law. The Paris law parameters are used in the cohesive model previously mentioned. The FEM software first solves the static part and then the fatigue one, the result in the aperture of the model is reported in Figure 4.6.

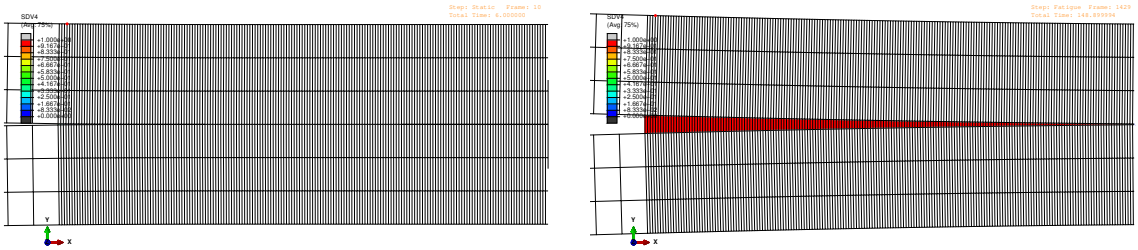

Figure 4.6: Propagation of the degradation during fatigue.

4.5.1. Numerical and experimental comparison

Figure 4.7 represents the crack length growth during the test. The experimental curve, similarly to all the other characteristic curves, presents a jump at 34000 cycles. This phenomenon can be explained by the presence of voids or defects in a particular region of the specimen. Contrary to that the numerical curve is smooth and it reconnects to the experimental one after the jump. The main issue of the numerical curve is the abrupt start of the crack growth, in fact during the experiment the curve starts only after a certain amount of cycles, while the numerical one does not preserve the original pre-crack during the first cycles. The onset of the crack growth is not represented well by the model, and this issue is conserved during the first part of the curve. The gap between the curves built in the first cycle is maintained until the jump of the experimental one. This behavior is easy to see in the crack length history but not in the crack speed Figure 4.8. The speed of the two curves is really close through the all number of cycles, as already anticipated, the speed is the same, and the problems appear at the beginning of the fatigue step.

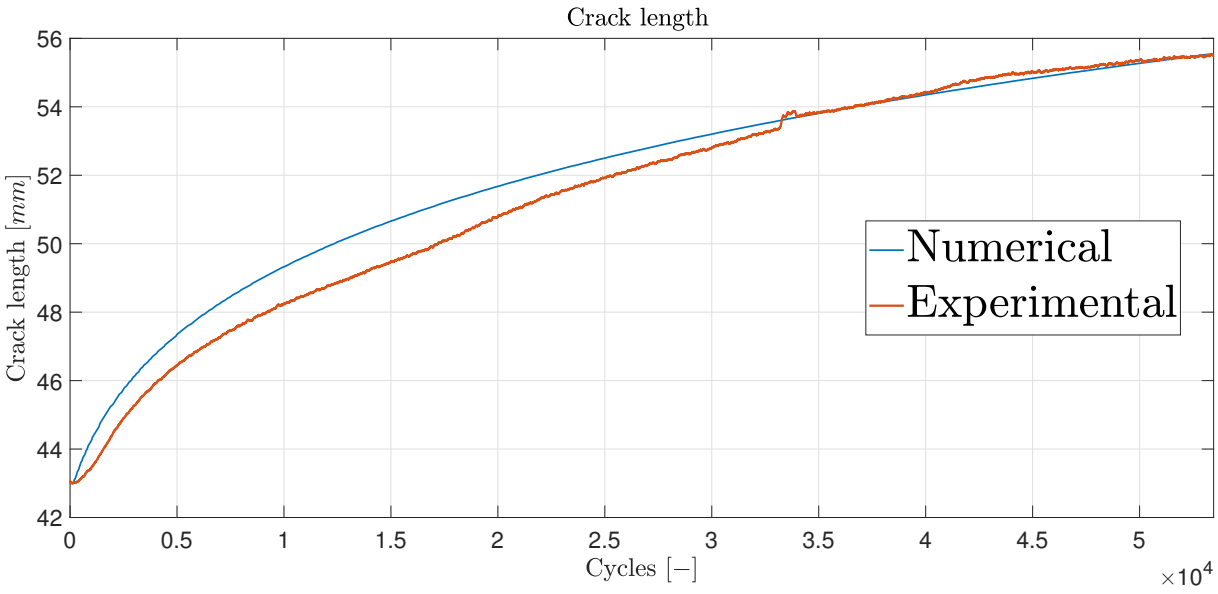

Figure 4.7: Fatigue crack length.

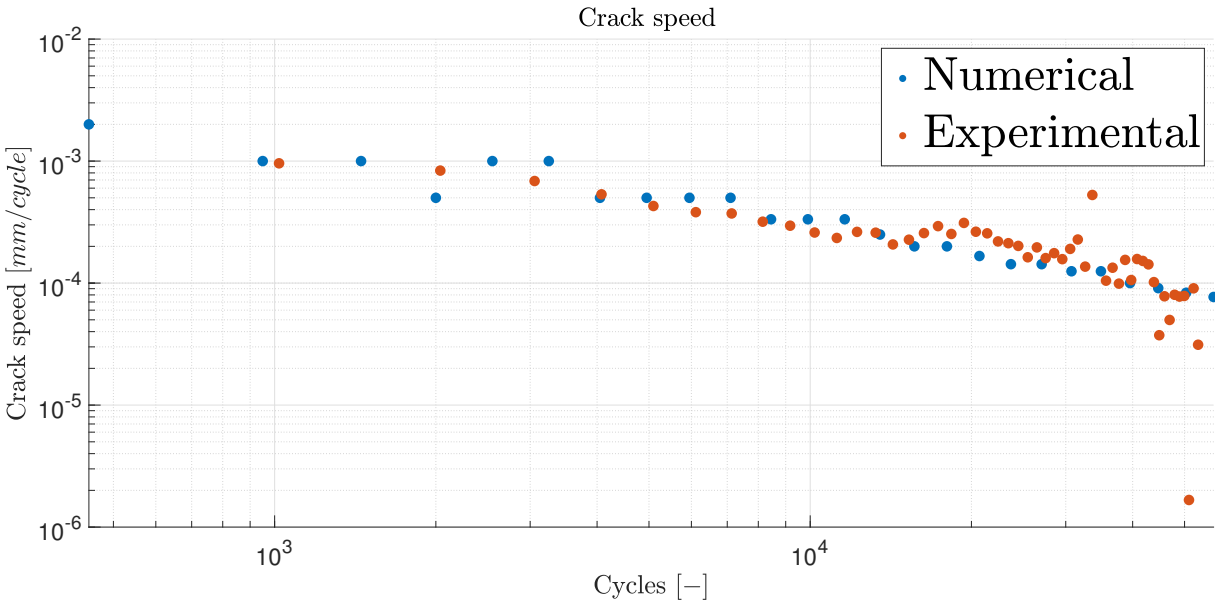

Figure 4.8: Fatigue crack speed.

Other variables taken into consideration are the load decrement Figure 4.9 and the fracture toughness Figure 4.10. Since the test configuration provides a constant aperture and the fatigue induce crack growth the load decrease since the resistance of the material to the aperture decreases. Also in this case the fitting increases the quality at a higher number of cycles.

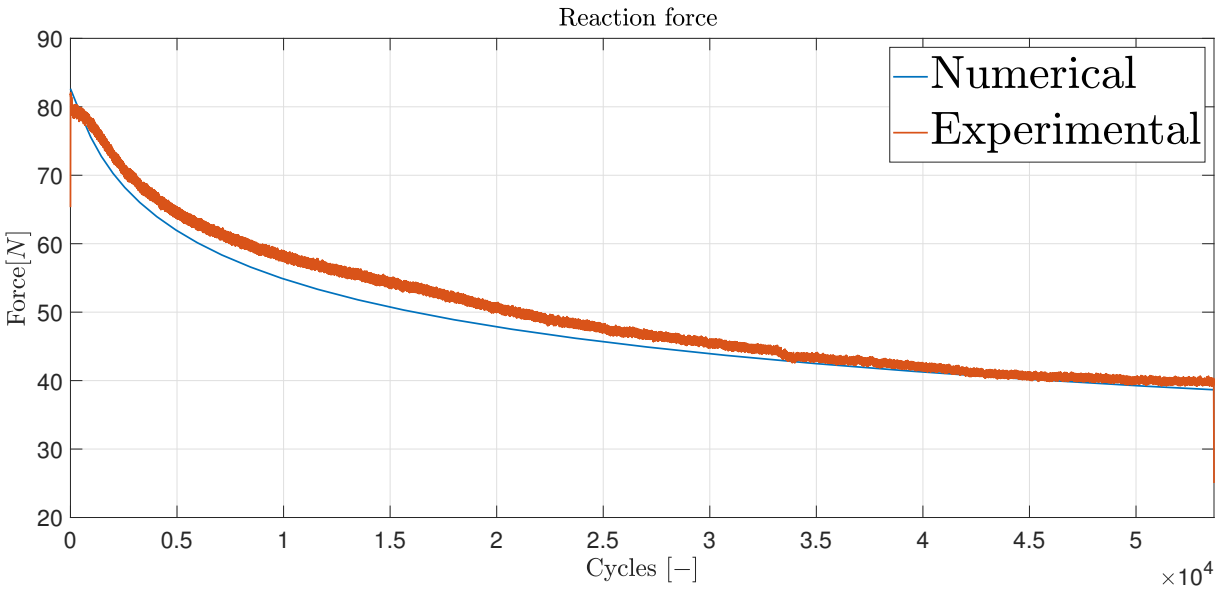

Figure 4.9: Fatigue load decrement.

The fracture toughness, which is a combination of crack propagation and load decrement has a behavior common to the previously mentioned parameters.

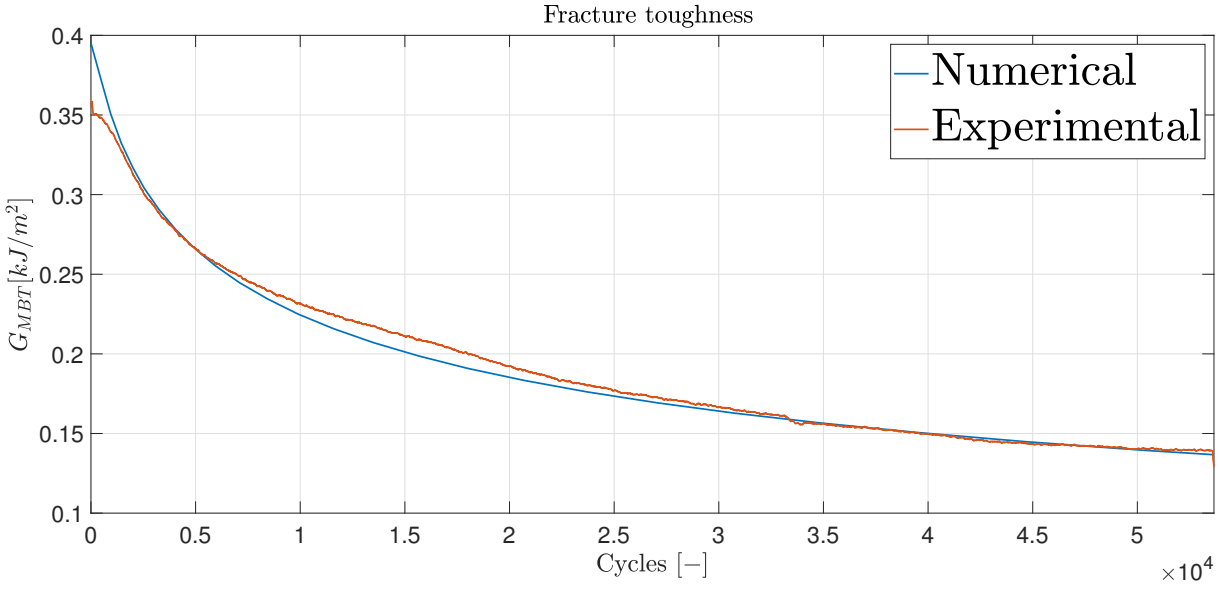

Figure 4.10: Fatigue fracture toughness decrement.

Finally, the last result, which summarizes at best the performances of the method, is reported as the Paris law in Figure 4.11.

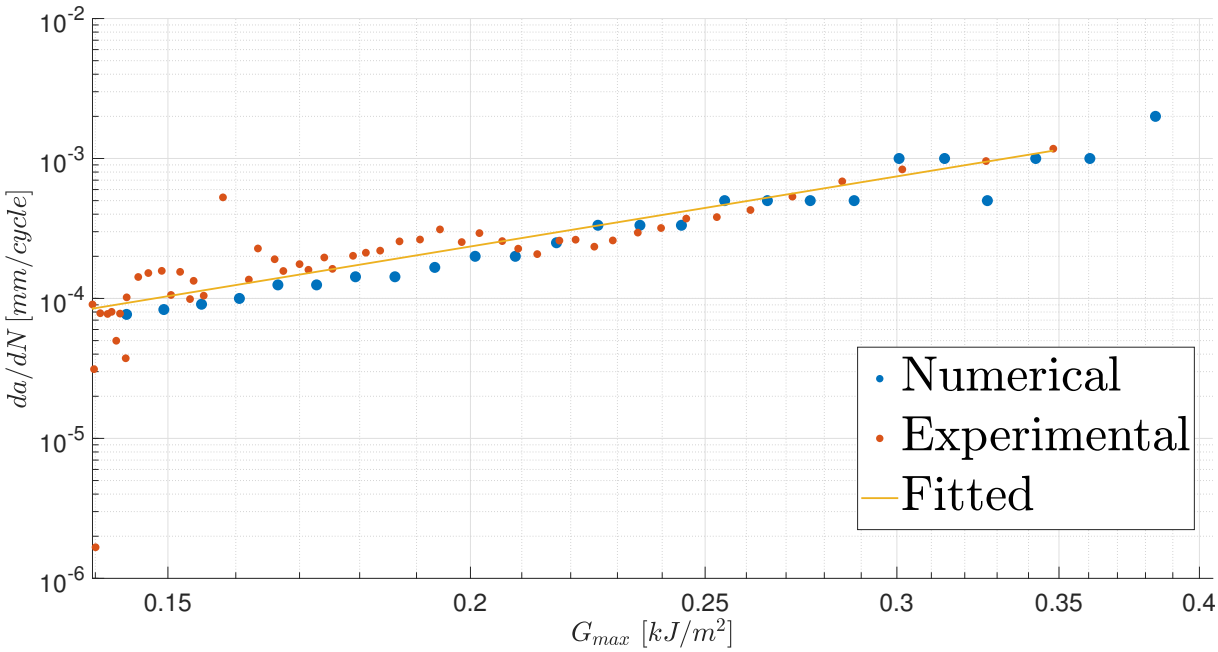

Figure 4.11: Paris law.

A parameter-fitting procedure for the fatigue analysis has not been implemented in this study. The rate of degradation for the fatigue part could be optimized to retrieve a better fitting between numerical and experimental results, but the model itself should be revisited to do so. The static characteristic of the cohesive elements has been considered equal to the one found during the optimization of the static part, without considering a possible discrepancy in the specimen itself. The major problem of the model lies in the onset of the crack propagation, the model is not able to predict the quiescent part at the begging of the fatigue cycle, but it performs well when the crack is fully developed. In the next studies, huge efforts should be added to avoid this difference between numerical and experimental. Nucleation capabilities shall be added to the model, in order to catch the initial response of the model.

5 | Conclusions and future developments

5.1. What has been achieved

During the development of this thesis, it has been performed, initially, an experimental campaign. The tests performed were the double cantilever beam and the end-notched flexure of uni-directional laminates composed of Solvay's PC(PEKK-FC)/S2 plies. The former returned good results in terms of fracture toughness in particular conditioned by the fiber bridging phenomena appearance. The latter, instead, witnessed an awkward behavior, characterized by sudden propagation of the crack tip, not common in literature.

The next step has been the numerical simulation of the obtained result, where the main objective has been to find a numerical representation of what has been observed experimentally. This has been achieved first of all with the implementation of a constitutive law for cohesive elements and then with a parameter-fitting algorithm. A modified tri-linear cohesive law has been coded to simulate the variation of the fracture toughness during the tests caused by the fiber-bridging, which is responsible for the increase of the inter-laminar properties. The model used, with parameters found through the manipulation of the experimental result, retrieves fair results. However, in order to achieve the best possible correlation between numerical and experimental representation an optimization algorithm has been exploited to find the parameters for the cohesive law. The Nelson-Mead algorithm has been the selected one, due to its good minimization properties in a highly demanding computational environment.

After the quasi-static analysis, fatigue has been the next point to be faced. The Kawashita-Harper model has been extended to the context of tri-linear cohesive elements and a numerical study has been performed. Despite the need of a further fix the results of the simulations return good results in terms of the extracted Paris law.

5.2. What comes next

As anticipated in the previous section, the results of the ENF test have not been considered valid, this has led to the impossibility to find the right fracture toughness for mode II delamination, as a consequence numerical analysis of this it has not been performed. That being said further development should move to the solution of these visible issues allowing a better characterization of the material to see if the cohesive law obtained, after some modification, could be applied also to this study case.

Bibliography

[1] Hanna Dodiuk. *Handbook of thermoset plastics*. William Andrew, 2021.

[2] Victor Gold, editor. *The IUPAC Compendium of chemical terminology*. International Union of Pure and Applied Chemistry (IUPAC), Research Triangle Park, NC, 2019.

[3] Stephan A Baeurle, Atsushi Hotta, and Andrei A Gusev. On the glassy state of multiphase and pure polymer materials. *Polymer*, 47(17):6243–6253, 2006.

[4] B.H.A.H. Tijs, S. Abdel-Monsef, J. Renart, A. Turon, and C. Bisagni. Characterization and analysis of the interlaminar behavior of thermoplastic composites considering fiber bridging and r-curve effects. *Composites Part A: Applied Science and Manufacturing*, 162:107101, 2022.

[5] NJ Pagano and GA Schoeppner. Delamination of polymer matrix composites: problems and assessment. 2000.

[6] TE Tay and F Shen. Analysis of delamination growth in laminated composites with consideration for residual thermal stress effects. *Journal of composite materials*, 36(11):1299–1320, 2002.

[7] Allan S Crasto and Ran Y Kim. Hygrothermal influence on the free-edge delamination of composites under compressive loading. *ASTM special technical publication*, 1285:381–393, 1997.

[8] Vladimir V Bolotin. Delaminations in composite structures: its origin, buckling, growth and stability. *Composites Part B: Engineering*, 27(2):129–145, 1996.

[9] VV Bolotin. Mechanics of delaminations in laminate composite structures. *Mechanics of Composite Materials*, 37(5):367–380, 2001.

[10] George R Irwin. Analysis of stresses and strains near the end of a crack traversing a plate. 1957.

[11] Alan Arnold Griffith. Vi. the phenomena of rupture and flow in solids. *Philosophical*

transactions of the royal society of london. Series A, containing papers of a mathematical or physical character, 221(582-593):163–198, 1921.

[12] Standard test method for mode i interlaminar fracture toughness of unidirectional fiber-reinforced polymer matrix composites 1. 2009.

[13] T Kevin O'Brien. *Results of ASTM round robin testing for mode 1 interlaminar fracture toughness of composite materials*, volume 104222. National Aeronautics and Space Administration, Langley Research Center, 1992.

[14] JP Berry. Determination of fracture surface energies by the cleavage technique. *Journal of applied physics*, 34(1):62–68, 1963.

[15] Kazuro Kageyama and Masaki Hojo. Proposed methods for interlaminar fracture toughness tests of composite laminates. *Achievement in composites in Japan and the United States*, pages 227–234, 1990.

[16] W Steven Johnson and PD Mangalgiri. Investigation of fiber bridging in double cantilever beam specimens. Technical report, NATIONAL AERONAUTICS AND SPACE ADMINISTRATION HAMPTON VA LANGLEY RESEARCH ..., 1986.

[17] John H Crews, KN Shivakumar, and IS Raju. A fiber-resin micromechanics analysis of the delamination front in a dcb specimen. Technical report, 1988.

[18] Mototsugu Sakai, Tatsuya Miyajima, and Michio Inagaki. Fracture toughness and fiber bridging of carbon fiber reinforced carbon composites. *Composites science and technology*, 40(3):231–250, 1991.

[19] ASTM WK22949. New test method for determination of the mode ii interlaminar fracture toughness of unidirectional fiber reinforced polymer matrix composites using the end-notched flexure (enf) test. *American Society for Testing and Materials, West Conshohocken*, 2009.

[20] Nicolas Moës, John Dolbow, and Ted Belytschko. A finite element method for crack growth without remeshing. *International Journal for Numerical Methods in Engineering*, 46(1):131–150, 1999.

[21] B. Tafazzolimoghaddam. *Computational Mechanics of Fracture and Fatigue in Composite Laminates by Means of XFEM and CZM*. PhD thesis, University of Sheffield, 10 2017.

[22] William S Slaughter. *The linearized theory of elasticity*. Springer Science & Business Media, 2012.

[23] Journal für die reine und angewandte mathematik, 1909.

[24] Alexandre Ern and Jean-Luc Guermond. *Theory and practice of finite elements*, volume 159. Springer, 2004.

[25] Daosheng Ling, Qingda Yang, and Brian Cox. An augmented finite element method for modeling arbitrary discontinuities in composite materials. *International journal of fracture*, 156(1):53–73, 2009.

[26] Nicolas Moës and Ted Belytschko. Extended finite element method for cohesive crack growth. *Engineering fracture mechanics*, 69(7):813–833, 2002.

[27] Daniel W Spring. Cohesive zone modeling of fracture of sustainable and functionally graded concrete. 2011.

[28] Ronald Krueger. Virtual crack closure technique: History, approach, and applications. *Appl. Mech. Rev.*, 57(2):109–143, 2004.

[29] George R Irwin. Analysis of stresses and strains near the end of a crack traversing a plate. 1957.

[30] Z. Zou, S.R. Reid, P.D. Soden, and S. Li. Mode separation of energy release rate for delamination in composite laminates using sublaminates. *International Journal of Solids and Structures*, 38(15):2597–2613, 2001.

[31] E.F. Rybicki and M.F. Kanninen. A finite element calculation of stress intensity factors by a modified crack closure integral. *Engineering Fracture Mechanics*, 9(4):931–938, 1977.

[32] D.S. Dugdale. Yielding of steel sheets containing slits. *Journal of the Mechanics and Physics of Solids*, 8(2):100–104, 1960.

[33] G.I. Barenblatt. The mathematical theory of equilibrium cracks in brittle fracture. volume 7 of *Advances in Applied Mechanics*, pages 55–129. Elsevier, 1962.

[34] A. Hillerborg, M. Modéer, and P.-E. Petersson. Analysis of crack formation and crack growth in concrete by means of fracture mechanics and finite elements. *Cement and Concrete Research*, 6(6):773–781, 1976.

[35] Viggo Tvergaard and John W Hutchinson. The relation between crack growth resistance and fracture process parameters in elastic-plastic solids. *Journal of the Mechanics and Physics of Solids*, 40(6):1377–1397, 1992.

[36] Weicheng Cui and MR Wisnom. A combined stress-based and fracture-mechanics-

based model for predicting delamination in composites. *Composites*, 24(6):467–474, 1993.

[37] A Needleman. An analysis of tensile decohesion along an interface. *Journal of the Mechanics and Physics of Solids*, 38(3):289–324, 1990.

[38] Philippe H Geubelle and Jeffrey S Baylor. Impact-induced delamination of composites: a 2d simulation. *Composites Part B: Engineering*, 29(5):589–602, 1998.

[39] A Turon, Pedro Ponces Camanho, J Costa, and CG Dávila. A damage model for the simulation of delamination in advanced composites under variable-mode loading. *Mechanics of materials*, 38(11):1072–1089, 2006.

[40] Fatih Dogan, Homayoun Hadavinia, Todor Donchev, and Prasannakumar S Bhonge. Delamination of impacted composite structures by cohesive zone interface elements and tiebreak contact. *Central European Journal of Engineering*, 2(4):612–626, 2012.

[41] Mohsen Moslemim and Mohammadreza Khoshravan. Cohesive zone parameters selection for mode-i prediction of interfacial delamination/izbira parametrov kohezijske cone za napovedovanje medpovrsinske delaminacije tipa i. *Strojniski Vestnik-Journal of Mechanical Engineering*, 61(9):507–517, 2015.

[42] M L Benzeggagh and MJCS Kenane. Measurement of mixed-mode delamination fracture toughness of unidirectional glass/epoxy composites with mixed-mode bending apparatus. *Composites science and technology*, 56(4):439–449, 1996.

[43] Kyoungsoo Park, Glaucio H Paulino, and Jeffery R Roesler. A unified potential-based cohesive model of mixed-mode fracture. *Journal of the Mechanics and Physics of Solids*, 57(6):891–908, 2009.

[44] Kyoungsoo Park and Glaucio H Paulino. Computational implementation of the ppr potential-based cohesive model in abaqus: Educational perspective. *Engineering fracture mechanics*, 93:239–262, 2012.

[45] Carlos G Dávila, Cheryl A Rose, and Pedro P Camanho. A procedure for superposing linear cohesive laws to represent multiple damage mechanisms in the fracture of composites. *International Journal of Fracture*, 158(2):211–223, 2009.

[46] M Heidari-Rarani and AR Ghasemi. Appropriate shape of cohesive zone model for delamination propagation in enf specimens with r-curve effects. *Theoretical and Applied Fracture Mechanics*, 90:174–181, 2017.

[47] Alessandro Airoldi and Carlos G Dávila. Identification of material parameters for

modelling delamination in the presence of fibre bridging. *Composite Structures*, 94(11):3240–3249, 2012.

[48] R Gutkin, ML Laffan, ST Pinho, P Robinson, and PT Curtis. Modelling the r-curve effect and its specimen-dependence. *International Journal of Solids and Structures*, 48(11-12):1767–1777, 2011.

[49] Yu Gong, Yixin Hou, Libin Zhao, Wangchang Li, Jianyu Zhang, and Ning Hu. A modified mode i cohesive zone model for the delamination growth in dcb laminates with the effect of fiber bridging. *International Journal of Mechanical Sciences*, 176:105514, 2020.

[50] Michael Smith. *ABAQUS/Standard User's Manual, Version 6.9*. Dassault Systèmes Simulia Corp, United States, 2009.

[51] William P Heising. Fortran. *Communications of the ACM*, 6(3):85–86, 1963.

[52] Georges Duvant and Jacques Louis Lions. *Inequalities in mechanics and physics*, volume 219. Springer Science & Business Media, 2012.

[53] Antonio Caggiano, Enzo Martinelli, Diego Said Schicchi, and Guillermo Etse. A modified duvaut-lions zero-thickness interface model for simulating the rate-dependent bond behavior of frp-concrete joints. *Composites Part B: Engineering*, 149:260–267, 2018.

[54] Jorge Zahr Viñuela, María Torres, and Rafael Guerra Silva. Cohesive zone modeling in load–unload situations. *International Journal of Mechanical Sciences*, 222:107205, 2022.

[55] Julian J. Rimoli, Juan J. Rojas, and Farah N. Khemani. On the mesh dependency of cohesive zone models for crack propagation analysis. 2012.

[56] Cohesive zone length in numerical simulations of composite delamination. *Engineering Fracture Mechanics*, 75(16):4774–4792, 2008.

[57] Arturo Pascuzzo, Fabrizio Greco, Lorenzo Leonetti, Paolo Lonetti, Andrea Pranno, and Camilla Ronchei. Investigation of mesh dependency issues in the simulation of crack propagation in quasi-brittle materials by using a diffuse interface modeling approach. *Fatigue & Fracture of Engineering Materials & Structures*, 45(3):801–820, 2022.

[58] Julian J Rimoli and Juan J Rojas. Meshing strategies for the alleviation of mesh-

induced effects in cohesive element models. *International Journal of Fracture*, 193(1):29–42, 2015.

[59] Kyoungsoo Park, Glaucio H. Paulino, Waldemar Celes, and Rodrigo Espinha. Adaptive mesh refinement and coarsening for cohesive zone modeling of dynamic fracture. *International Journal for Numerical Methods in Engineering*, 92(1):1–35, 2012.

[60] J. A. Nelder and R. Mead. A simplex method for function minimization. *The Computer Journal*, 7(4):308–313, 01 1965.

[61] Margaret H Wright et al. Nelder, mead, and the other simplex method. *Documenta Mathematica*, 7:271–276, 2010.

[62] Marco A Luersen and Rodolphe Le Riche. Globalized nelder–mead method for engineering optimization. *Computers & structures*, 82(23-26):2251–2260, 2004.

[63] Pauli Virtanen, Ralf Gommers, Travis E. Oliphant, Matt Haberland, Tyler Reddy, David Cournapeau, Evgeni Burovski, Pearu Peterson, Warren Weckesser, Jonathan Bright, Stéfan J. van der Walt, Matthew Brett, Joshua Wilson, K. Jarrod Millman, Nikolay Mayorov, Andrew R. J. Nelson, Eric Jones, Robert Kern, Eric Larson, C J Carey, İlhan Polat, Yu Feng, Eric W. Moore, Jake VanderPlas, Denis Laxalde, Josef Perktold, Robert Cimrman, Ian Henriksen, E. A. Quintero, Charles R. Harris, Anne M. Archibald, Antônio H. Ribeiro, Fabian Pedregosa, Paul van Mulbregt, and SciPy 1.0 Contributors. SciPy 1.0: Fundamental Algorithms for Scientific Computing in Python. *Nature Methods*, 17:261–272, 2020.

[64] Gang Zhao, Jiaqi Xu, Yajie Feng, Jianbo Tang, Yousi Chen, Shiqing Xin, Xigao Jian, Shuxin Li, Shouhai Zhang, and Jian Xu. A rate-dependent cohesive zone model with the effects of interfacial viscoelasticity and progressive damage. *Engineering Fracture Mechanics*, 248:107695, 2021.

[65] Milad Saeedifar, Mehdi Ahmadi Najafabadi, Jalal Yousefi, Reza Mohammadi, Hossein Hosseini Toudeshky, and Giangiacomo Minak. Delamination analysis in composite laminates by means of acoustic emission and bi-linear/tri-linear cohesive zone modeling. *Composite Structures*, 161:505–512, 2017.

[66] M. Heidari-Rarani, M.M. Shokrieh, and P.P. Camanho. Finite element modeling of mode i delamination growth in laminated dcb specimens with r-curve effects. *Composites Part B: Engineering*, 45(1):897–903, 2013.

[67] Konstanze Kiefer. *Simulation of high-cycle fatigue-driven delamination in composites using a cohesive zone model*. PhD thesis, Imperial College London, 2014.

[68] A Turon, J Costa, PP Camanho, and CG Dávila. Simulation of delamination in composites under high-cycle fatigue. *Composites Part A: applied science and manufacturing*, 38(11):2270–2282, 2007.

[69] Yu V Skvortsov, SA Chernyakin, SV Glushkov, and SN Perov. Simulation of fatigue delamination growth in composite laminates under mode i loading. *Applied Mathematical Modelling*, 40(15-16):7216–7224, 2016.

[70] A Pirondi and F Moroni. A progressive damage model for the prediction of fatigue crack growth in bonded joints. *The Journal of Adhesion*, 86(5-6):501–521, 2010.

[71] Paul W Harper and Stephen R Hallett. A fatigue degradation law for cohesive interface elements–development and application to composite materials. *International Journal of Fatigue*, 32(11):1774–1787, 2010.

[72] Luiz F Kawashita and Stephen R Hallett. A crack tip tracking algorithm for cohesive interface element analysis of fatigue delamination propagation in composite materials. *International Journal of Solids and Structures*, 49(21):2898–2913, 2012.

[73] F Teimouri, M Heidari-Rarani, and F Haji Aboutalebi. Finite element modeling of mode i fatigue delamination growth in composites under large-scale fiber bridging. *Composite Structures*, 263:113716, 2021.

A | Numerical representation of non-conformity

The experimental results presented in the thesis contain some behavior that cannot be predicted with standard methods. In this section, an embryonic study on two different issues is presented. Due to the low impact of the research, these studies are reported in the appendix as exercises, which emphasize the possibility related to cohesive elements when dealing with composite fractures.

A.1. Imperfect closure of mode-I test

Following various DCB tests, each specimen exhibits a similar behavior in the un-loading phase, i.e. the presence of residual strain compared to the initial configuration when the piece is completely unloaded.
During the modeling phase of the tensile response of the material, a constitutive law for three-linear cohesive elements was constructed, as reported in Figure A.1. Cohesive elements are used to model the entire area in which the crack is destined to propagate, their contribution, however, occurs only during the activation phase or the phase in which their degradation begins to take place. Their degradation, therefore, shapes the enlargement of pre-existing defects and their union. The traditional description uses an elastic return during the element unloading, as shown in red in Figure A.1. The result for DCB loading and unloading according to the current modeling is shown in Figure A.2:

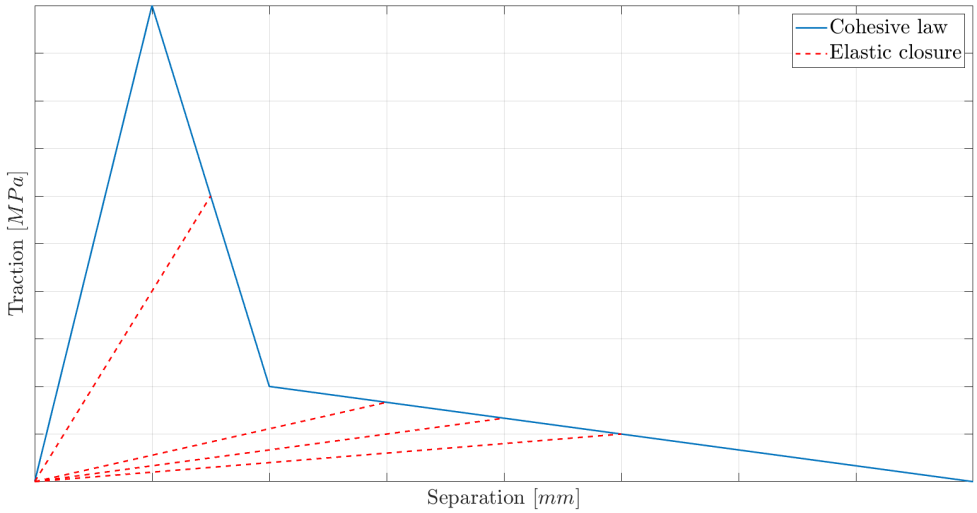

Figure A.1: Cohesive law with elastic un-loading

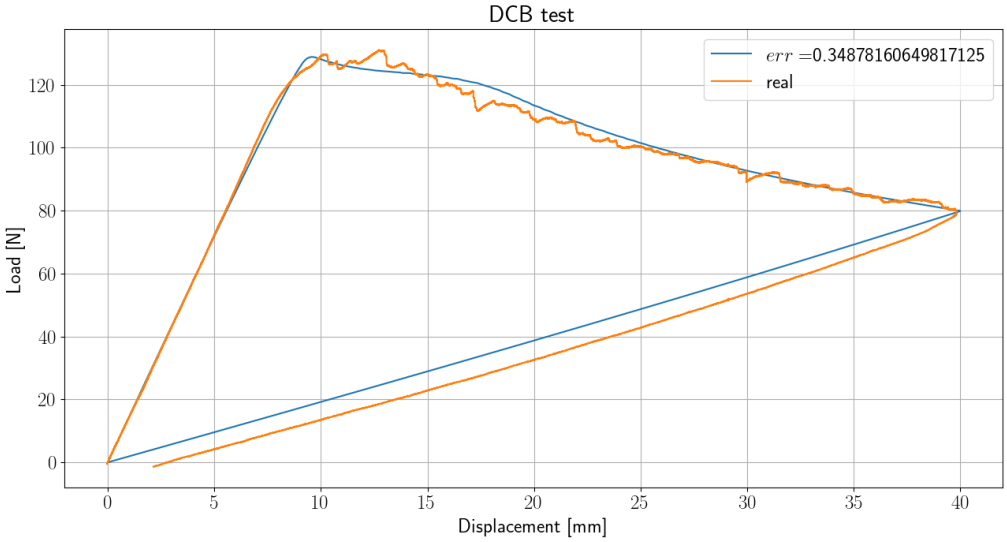

Figure A.2: Load displacement with elastic un-loading

As can be seen from the image, considering each material capable of having an elastic recovery means that in the FEM model the response of the specimen to the unloading is to return to the original configuration, this determines a great discrepancy between the simulated and experimentally observed unloading. Several hypotheses can be advanced to try to explain the phenomenon of the non-elastic return of the DCB test, including the plasticization of the flaps, excluded first for not excessive strain levels, plasticization of

the crack propagation zone, or interference of the fibers detached from the matrix which create a dividing layer between the two arms.
To model this phenomenon, leaving the cohesive load law unchanged, which discretely describes the opening phase, the cohesive unloading response is modified. Here is presented a response that for separations lower than a certain value gives a response equal to the traditional one, ie elastic with an inverse elastic modulus to the degradation factor, while for values higher than this threshold it provides a plastic response. Since the cohesive law in traction has not been modified, there is no plateau typical of a plastic deformation but linear degradation is confirmed. This model is shown in Figure A.3.

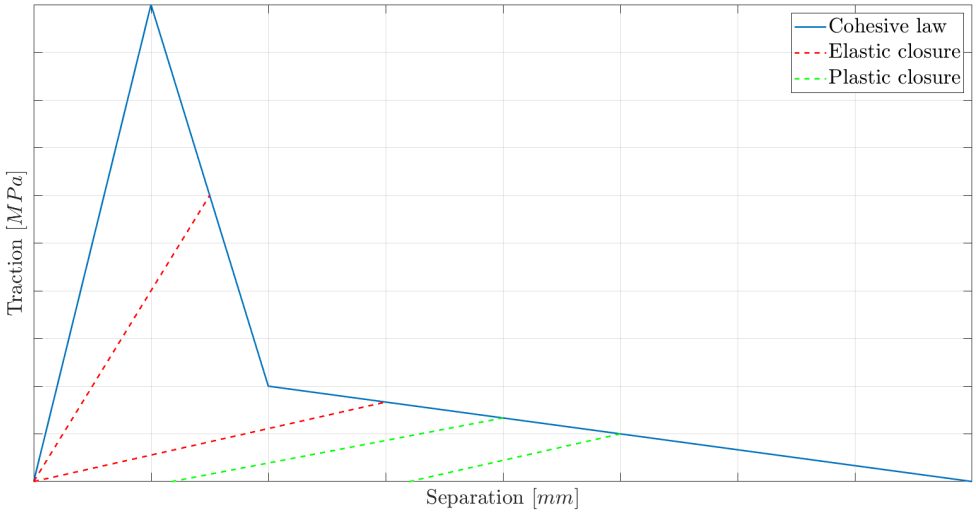

Figure A.3: Cohesive law with Non-elastic un-loading

This cohesive response can model both resistance to flattening of the fibers separated from the matrix and plasticization in the crack propagation zone. The second phenomenon should mainly characterize the first phase of opening, therefore at lower separation levels, this phenomenon is normally modeled on a cohesive level with a trapezoidal law. In this case of analysis, the trapezoidal law is not taken into consideration since it is typical of materials in which almost all of the energy is spent on crack opening and the process area is limited, therefore not in conformity with the phenomenon of fiber-bridging. Figure A.4 shows the trend taking into account the new cohesive law.

The response of the new cohesive law appropriately calibrated allows obtaining a return configuration equivalent to the experimental one. In fact, once the load has ceased, the distance between the pre-test and post-test configuration is the same for the numerical case and the experimental one. A discrepancy between the numerical and experimental

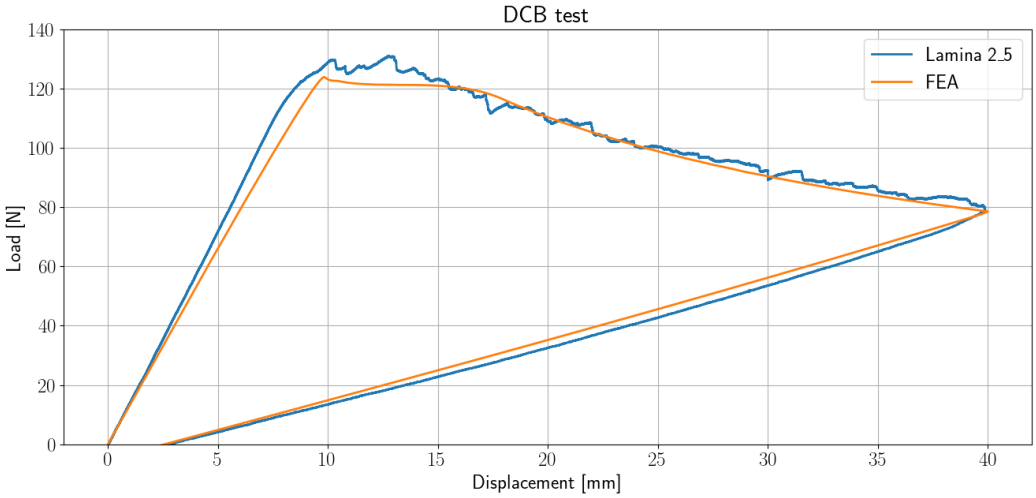

Figure A.4: Load displacement with non-elastic un-loading cohesive

unloading phases is however present; in fact, the experimental curve is slightly more concave than the numerical one.

A.2. Defects study

The second issue encountered during the experimental campaign is the presence of jumps in the load-displacement curve and the correlated instantaneous propagation of the crack. This phenomenon is represented in Figure A.5, where it is visible a moment in which a huge decrement in the load appears suddenly.

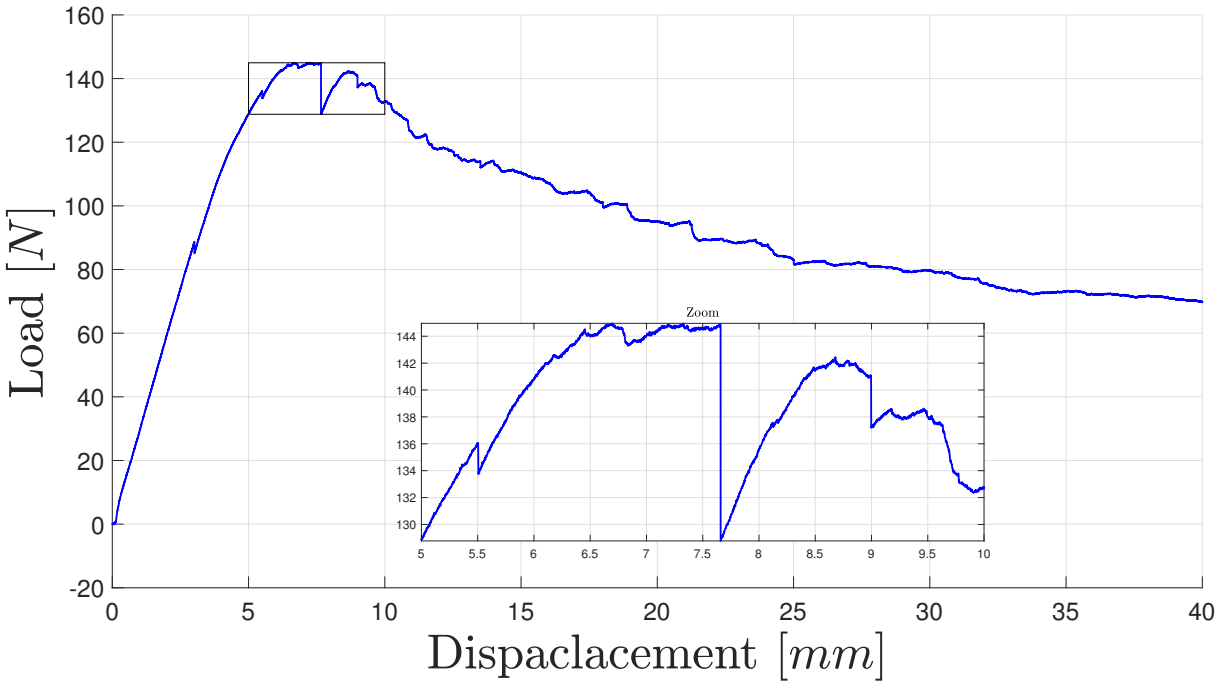

Figure A.5: Load displacement curve jump

The physical reason for what is experienced can be motivated by the presence of defects inside the laminate. In a particular, a weak region is present in a precise reason of the interface between the plies. This weakness causes a sudden propagation of the crack inside the laminate; the tip does not find any barrier on its path and can release the energy collected at the crack's tip faster. The sudden crack propagation generates a jump in the load curve. The presence of a different propagation behavior can be seen also from a fractography point of view. It is possible to distinguish two different fracture surfaces, one almost smooth and polished and one matt and rough. The polished part is related to the region in which the crack propagates instantly.

The open questions related to the subjects are: what is the reason for the weakness and is it possible to obtain a numerical representation of the phenomena? The first step to answer the former question is the identification of the typology of defects present at the interface where the jump happens. This investigation could be performed with SEM.

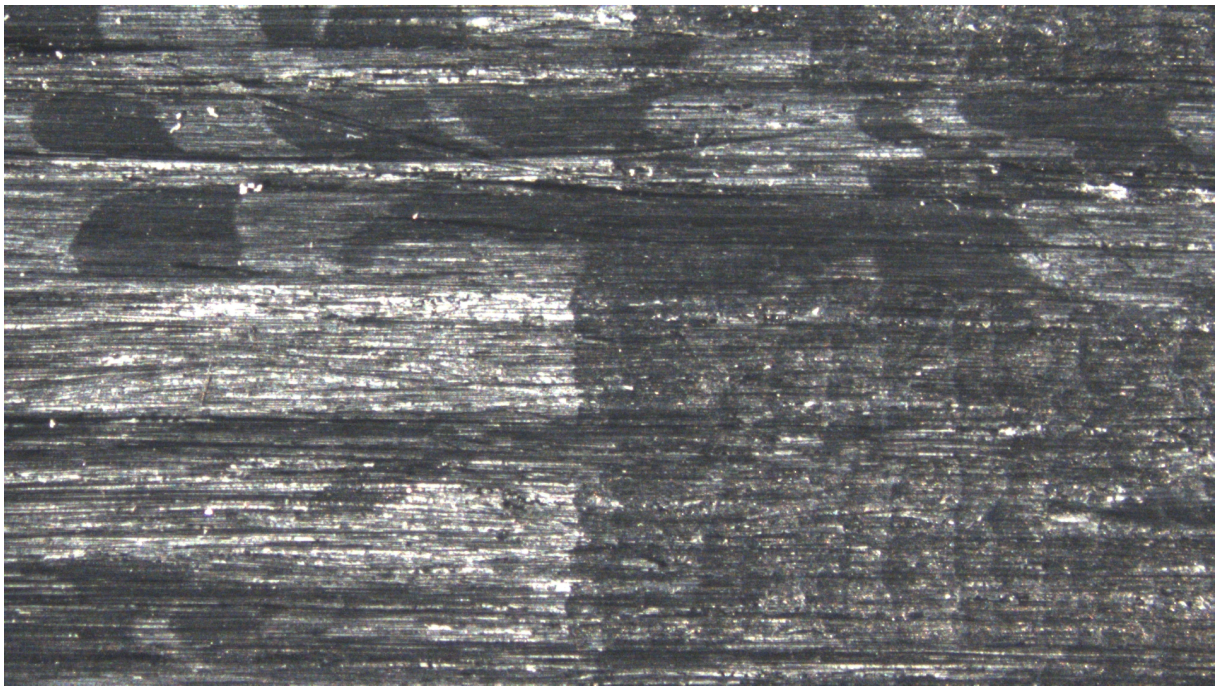

Figure A.6: Optic microscope fractography

Defects that originate this sudden variation are most of the time voids and contamination of the matrix. In order to avoid this problem in future studies if the problem is connected to voids the solution could lie in a different pressure or temperature in the hot-press process for the production of the laminates. The root cause determination is still an open question for the study; however, a numerical study on the modeling part has been performed. In order to achieve the same behavior of the experimental curve 4 entire rows of elements have been subtracted by the cohesive region as represented in Figure A.7.

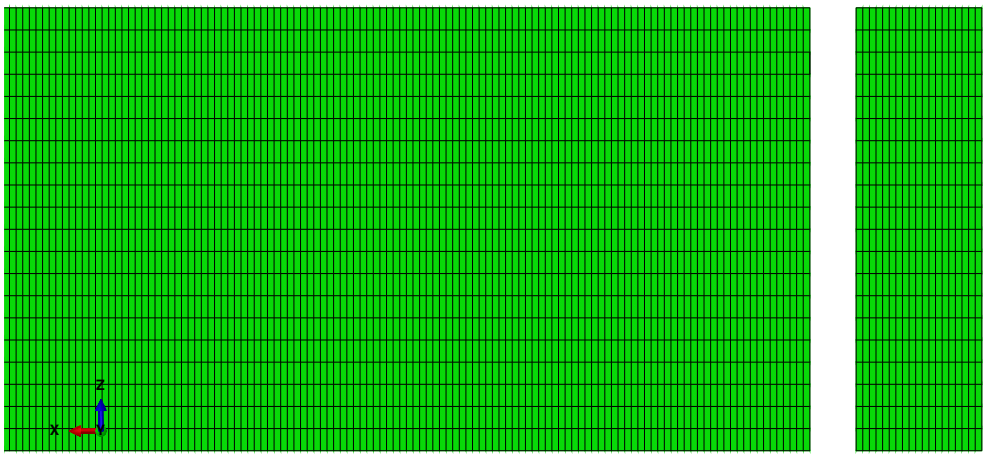

Figure A.7: Defects numerical configuration

The FEM configuration to find the strongest correlation with the experimental curve has been found with a trial and error procedure. It is visible from the figure that many elements are not present in the configuration, creating a large void in the inter-laminar region.

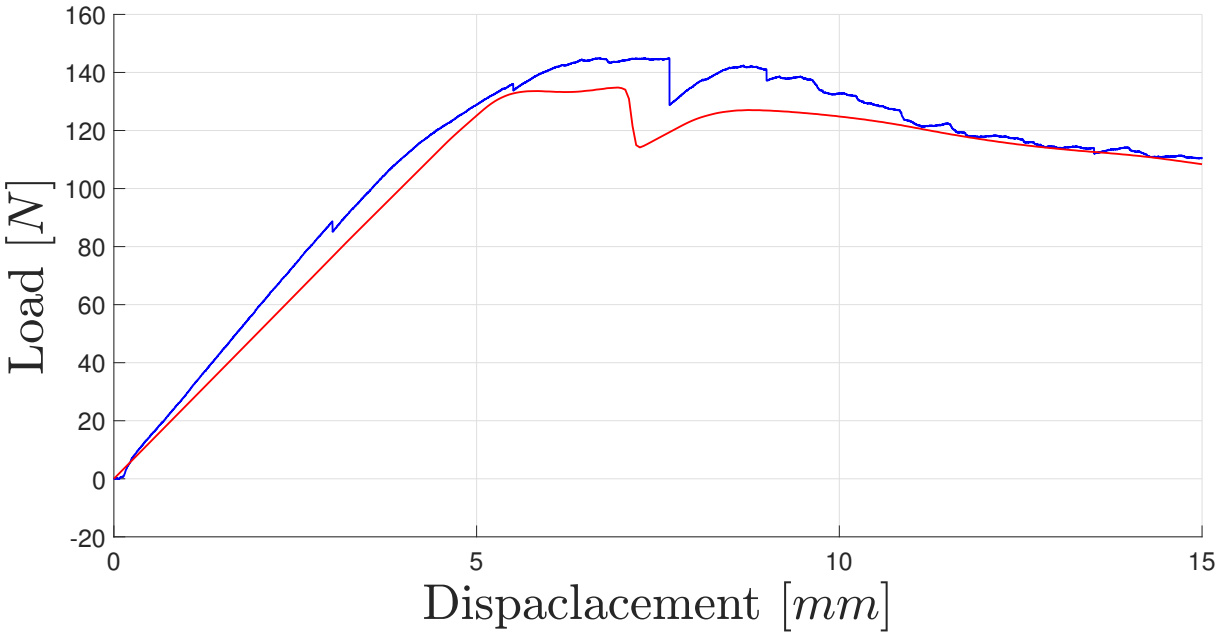

Figure A.8: Defect study comparison

In Figure A.8 the comparison between the numerical curve and the experimental one is present. The main objective, in this case, is not to find a perfect match between numerical and experimental but just to find a representation that can return a similar jump. The entity of the phenomena is obtained, however, the representation has a strong impact on the model itself. The dimension of the void used is very large with respect to the total area of the contact between plies. Such a defect if present determines poor performance during manufacturing.

Acknowledgements

I want to appreciate and express my heartfelt gratitude to my supervisor Prof.Grande, who made this job possible. His direction and assistance saw me through all phases of writing my project. I also want to thank my committee members for making my defense a delightful experience, as well as for your insightful remarks and recommendations.

I would like to thank Dott. Enrico Chemello, who supervised my entire work from the beginning. Thanks to your help, and the conversations held in the laboratory this work has grown over the months and I could manage to start a deeper understanding of the subject.

In addition, a thank you to my colleagues and supervisors of Akka Technologies and Thales Alenia Space, who helped me build the beginning of my professional career and allow me to continue with a full effort regime for my thesis production.

A final remarkable acknowledgment to my family and to my friends. Your support and love have been my main energy source, the comfort that you bring eases my pains and struggles.